# *Graphene Nano-ribbon Patterning and Characterisation Towards Boolean Logic Gates*

by *Teodor Nikolov*

**For the degree of**

**Master of Embedded Systems**

**At Delft University of Technology**


***To be defended publicly on 28.09.2020 at 15:00PM***

**Supervisor**
Prof.dr. Sorin Cotofana

**Daily Supervisors**
Dr.ir. Sten Vollebregt

**Thesis Committee:**
Prof.dr. Sorin Cotofana
Dr.ir. Sten Vollebregt
Prof.dr. Paddy French

# Acknowledgements

The two years at TU Delft have brought me lots of valuable memories. This thesis marks an end to my journey for Master of Embedded Systems degree. There is no doubt that without the help from people I got to know during my thesis project, I would not achieve this outcome.

First of all, I would like to express my appreciation for the thesis committee: Prof. Dr. Sorin Cotofana, Dr.ir. Sten Vollebregt, Prof. Dr. Paddy French. Thanks Sorin, for giving the opportunity of doing this work in your lively group and for giving me the freedom to define my own project.

A very special thanks to Dr.ir. Sten Vollebregt for his support, enthusiasm during the lab work and for always being present to answer any of my questions. You were always ready to help, from the smallest lab problems, interpretation of the results to the instructions for all equipment and performing the part of the experiments to which I do not have access to. It was a big pleasure to work with you. Thank you, Sten!

A special thanks goes to two PhD students: Martin Lee and Maria El Abbassi who performed the fabrication of all samples. Despite their busy schedule, they always find time to give me new insights and their competences shown me that there is much for me to learn. Without you, this project was not possible and I was still going to look at fabricated graphene devices on Internet.

Furthermore, I would like to thank Yande Jiang and Nicoleta Cucu Laurenciu for the provided simulation model, being present to answer all my doubts and for the discussion that we had for improving the model. I would also like to thank, Leandro Sacco who provided me with a guidelines for AFM and for the help with every little problem that I bother him during imaging.

Lastly, I would like to thank my family and friends for their support, trust and patience during my whole educational period.

Teodor Nikolov

Delft, September 21, 2020

# Abstract

As CMOS scaling approaches the atomic feature size limit which results in a high power density and current leakage, low reliability and increased time and production cost, the need for new materials and devices is increasing. One of the promising materials to replace silicon based devices is graphene nano ribbons (GNRs) due to its remarkable electronic properties. Theoretical models suggest that `30nm` GNR structures can mimic the behaviour of basic Boolean logic gates such as inverter, buffer, or and nor gates while reducing `30x` times the propagation delay and using `3000x` less gate active area compared to the equivalent CMOS realisation. The main goal of this thesis is to fabricate GNR devices that can be ultimately used as building blocks for Boolean logic gates, analyse the limitations of achieving sub-50nm patterns and study the edge termination of the formed GNR patterns.

GNR patterns are explored using a simulation model, which can be used for complementary Boolean logic gates. The designed graphene patterns are simulated using tight binding model to calculate the electronic band structure and construct a Hamiltonian matrix. This is followed by calculation of the electronic states and Fermi energies. Non equilibrium Green function (NEGF) models the electrons and holes distribution trough the GNR pattern and the rate at which the charge carriers are transmitted from the source to the drain when they propagate through the device. The result from the NEGF function is used to calculate the charge density using 3D POISSON from which the current through the graphene surface is determined. Finally, with known gate voltages and current, the conductance is found for four different structures in 10 nm and 30 nm technology. By changing the way the structures are connected as pull-up and pull-down network, the behaviour of inverter, buffer, or, and nor gates are obtained.

The patterns from the simulation model with 30 nm feature size are used to create a design for devices to be fabricated. In addition, the design includes devices with minimal dimensions from 50 nm to 200 nm, squares, hexagons and pentagons with different dimensions starting from 1 $\mu$m up to 10 $\mu$m. For this project, graphene grown by chemical vapour deposition (CVD) was transferred to $SiO_2/Si$ samples on which the design of the structures is fabricated. The fabrication process consist of five steps. First, the samples are spin coated with polymethyl-methacrylate (PMMA). Second, electron beam lithography (EBL) is used to pattern the structures, by exposing parts of the resist. Next, the exposed areas are developed in order to remove the resist with introduced damage from the exposure. This is followed by etching the exposed parts of the graphene using oxygen plasma or hydrogen plasma. Finally, the remaining resist is cleaned with acetone.

Characterisation of the patterns is performed using Raman spectroscopy, scanning electron microscopy (SEM) and atomic force microscopy (AFM). From the Raman measurements it was found that the edge termination is most likely random and defects are introduced to the lattice of the graphene patterns with left contaminants from the polymer. The achieved minimal feature size of the devices is 50 nm, which was confirmed using AFM and SEM. In addition to the morphological characterisation of the samples, electrical measurements are performed and from the transport characteristics, the electron and hole mobilities of mono layer graphene are derived. The highest carrier mobility obtained from the measured patterns is 882 $cm^2$ $V^{-1}s^{-1}$.

# Contents

# Chapter 1

# Introduction

In 1975, Gordon Moore forecast that the components used per chip would double it's amount every two years [14]. Robert Dennard described in 1974 a scaling methodology for CMOS transistors that would deliver consistent improvements in transistor area, performance, and power reduction [3]. For the past 20 years, the leading companies has been developing new generation of semiconductors, and each generation was able to scaled the minimum feature size by a factor of 0.7 and area improvement of 0.5 every two years. Thus, the computing performance of the electronic devices increased by several orders of magnitude. However, recent technologies below 14 nm have taken longer than two year to develop, due to the fact that the process complexity and also the number of steps taken in the photo masking stage increased. Today's leading chips are made with a minimum feature size of approximately 30-40 nm that consists of several billion transistors. CMOS scaling approaches atomic feature size limit, which results in increased power dissipation, low yield, reliability and increased production cost [16]. In addition, with this minimalistic feature sizes the quantum effects that arise, are impossible to be ignored. This leads to the fact that it will be no longer possible to continue decreasing the transistor size using the same technological approaches and materials. Therefore, many researchers are focusing on alternative to silicon-based technology that could enable the production of smaller and faster circuits. One of the promising materials to replace the CMOS technology is graphene.

Graphene is the first one atom thick quasi–two-dimensional (2D) material extracted from graphite. This single atomic layer of graphite (mono layer graphene) has attracted enormous attention among scientific and technological communities after its discovery from Novoselov and Geim in 2004 [15] due to its remarkable properties such as high optical transmittance, high electrical and thermal conductivity, high carrier mobility, mechanical flexibility and strength. Novoselov and Geim et al. [15] contribute not only to the material discovery, but also that the mobility of charge carriers in graphene can exceed 10000 $cm^2$ $V^{-1}s^{-1}$ at room temperature with ballistic transport. In comparison, the carrier mobility of CMOS transistors is approximately 450 $cm^2$ $V^{-1}s^{-1}$ for hole mobility and between 700 to 1400 $cm^2$ $V^{-1}s^{-1}$ for electron mobility depending on the manufacturing quality of the Si [18]. Thus, graphene potentially can be used for the creation of much faster electronic devices. However, graphene have no band gap formation due to the touching of the conduction and valence bands in the band structure at the charge neutrality point. This leads to a very low conductivity and sets a limitation for graphene to be used as a material for digital logic applications. In order to overcome the energy-gap problem, researchers have been focused on band gap engineering of graphene using strips called graphene nano-ribbons.

## 1.1 Graphene nano-ribbons

Theoretically it was observed that when graphene is spatially confined in one direction to nano-meter scale, a finite band gap opens, which critically depends on the width and edge orientation. This structures in nano-meter scales are known as graphene nano-ribbons (GNRs) and have two possible edge terminations either zigzag or armchair. Both types of edge termination in GNR are visualised in figure 1.1. The properties of the GNRs are determined by its geometry either to act as a metallic or semiconductor element. The chemical properties of GNRs are also sensitive to the crystallographic orientations of their edges [11].

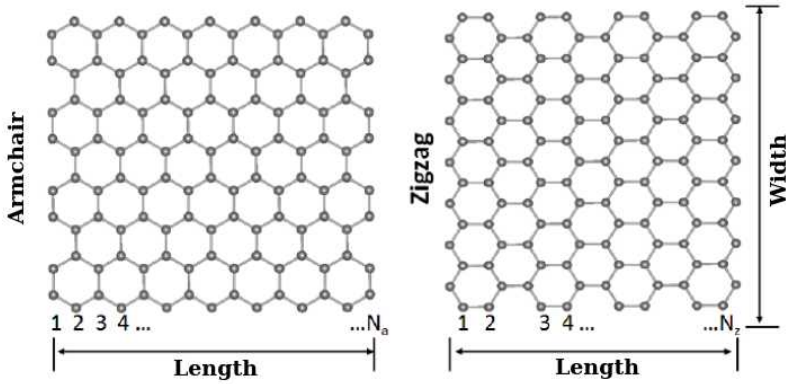


Figure 1.1: GNR structure of graphene with armchair and zigzag edges. (adapted from [9])

GNR with armchair edges can either have a conducting or semiconducting behaviour. Fujita, Son, and coworkers [5] performed a tight binding analysis and found that the armchair edges can be classified into three groups based on the number of atoms in the transverse direction (i.e width of the ribbon). The groups are presented in equation 1.1

$$\begin{aligned} Group_1 &= 3 * n \\ Group_2 &= 3 * n + 1 \\ Group_3 &= 3 * n + 2 \end{aligned} \tag{1.1}$$

where `n` is an arbitrary integer.

Armchair graphene nano-ribbons that have width equal to $3 * n$ and $3 * n + 1$ shows a semiconducting behaviour, while structures that their width is equal to $3 * n + 2$ are gapless or have very small energy band-gap and shows semi-metallic behaviour [20]. The gapless behaviour of armchair edges with width $3 * n + 2$ and the decreasing of the band gap in the other two groups is analytically confirmed using tight binding model (figure 1.2(A)). However, density-functional theory calculations suggest that even for the gapless group found by other methods there is a finite gap of approximately 0.1 eV as shown in figure 1.2(B) [17] .

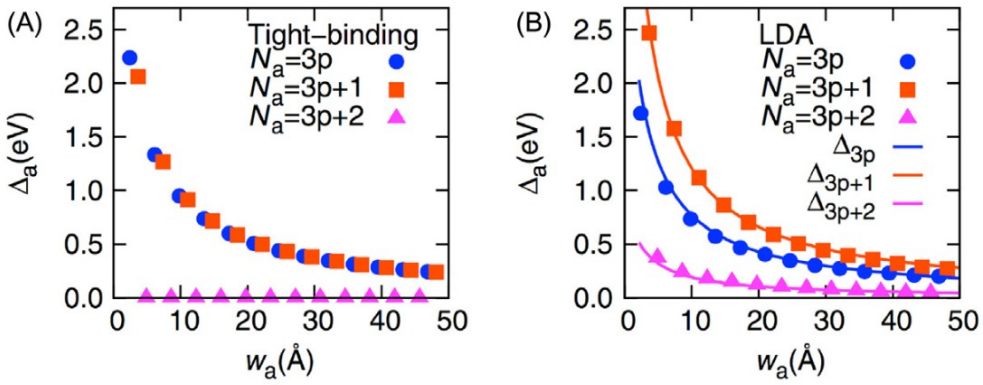


Figure 1.2: Band gaps of armchair edge graphene nanoribbons plotted as a function of its width. (A) tight-binding model (B) first-principles calculations using the local density approximation (adapted from [20])

The energy gap for armchair structures opens due to the anti ferromagnetic coupling between the magnetic moments at opposite edges of carbon atoms. The energy gap for this type of structures has always the same characteristic, in which the energy gap increases when the width of the GNR structure decreases [10].

Considering the groups in respect to the width dependency of the armchair edges to extract the semiconductor properties of the GNR with armchair edges a fabrication process with very high atomic precision is required. On the other hand, zigzag edge orientated GNRs are more stable. Theoretical models predicts that they do not have dependency to the groups as in armchair edges.

Zigzag edges provide the edge localized state with non-bonding molecular orbitals near the Fermi energy [19]. Due to this effect, the zigzag edge structure is expected to have large changes in optical and electronic properties from quantization [1]. Zigzag graphene nanoribbons are theoretically predicted to have a magnetic insulating ground state with ferromagnetic ordering at each zigzag edge and anti parallel spin orientation between the two edges [17]. It is experimentally observed that the band gaps of zigzag GNRs are smaller than those of armchair GNRs [2]. Theoretical models show that by changing the structure of the GNR with zigzag edge termination, it is possible to create a semiconductor behaviour and apply it for various type of logic gates [8].

Experimental results reported in [6] for temperature-dependent conductance measurement shows opening of finite gaps for devices in nm scale with width that varies from 15 nm to 90 nm. The authors observed band gap for the narrowest ribbons of approximately 200 meV and a drop to 1-5 meV for the ribbons with 90 nm width. They have reported also that for the measured devices the orientation of the GNR edges is not atomically precise. Li et. al [12] reported high $\frac{I_{on}}{I_{off}} > 10^5$ ratio for GNRs with widths below 10 nm and band-gap of approximately 150 meV, while for devices with width of 30 nm they observed low $\frac{I_{on}}{I_{off}}$ ratio equal to $10^1$ and band-gap below 50 meV.

## 1.2 The role of the edges in graphene nano-ribbons

The geometry and chemistry of GNRs have significant affects on the electronic properties. For zigzag edge termination, the edge state has a large local density of states and it is spin polarised. This plays a very important role in determine the electronic, magnetic and chemical properties of the GNR with zigzag edges. The impact of the electronic properties can also be caused by how foreign chemical species bond to the edge of the carbon atoms [13]. For example, the attachment of oxygen atoms causes effective boundary conditions. This together with the formed bondings have a strong impact on the electronic properties. Moreover, depending on

the number of hydrogen atoms attached to the linear zigzag edge causes the GNR to switch back and forth, which leads to ON–OFF switching of the electronic activity [4]. Therefore, to be able to obtain the best electronic properties from the GNR, the smoothness of the zigzag edges and cleanliness of the GNRs have an important role [7].

Nevertheless, it is still a challenging task to realise the chemical modification of a graphene edge and to tune the electronic properties in a controlled manner [4].

## 1.3 Research goals

The aim of this thesis is to explore the limitations of the fabrication process for graphene nano-ribbon devices and their potential to be used as a building blocks for Boolean logic devices. Thus, the research goal of this project is to answer the following main questions:

1. `What is the current achievable feature size of graphene nano-ribbon structures?`
2. `What is the edge termination of the patterned graphene structures?`
   (a) `How effectively graphene can be etched?`
   (b) `How can edge termination of the patterns be determined?`
   (c) `How effectively graphene can be cleaned after patterning?`
   (d) `How contaminants influence the electrical properties?`

## 1.4 Thesis outline

This document starts with the theoretical background to the problem in hand by summarising the currently available production, fabrication and characterisation methods of graphene nano-ribbons in Chapter 2. In Chapter 3, presents a detail description of a simulation model that is used as a proof of concept that graphene nano-ribbons can be used as a building blocks for Boolean logic gates. The simulation model is based on tight binding calculation and implementation of non equilibrium Green function (NEGF) in order to derive the conductivity of the GNR and from there to be linked to a specific Boolean operation. The obtained results of the shape and dimensions for GNR are used as a validation for the created and fabricated design, discussed in Chapter 4. Chapter 5 summarises the results from the characterisation process of the substrates. Finally, in Chapter 6 the conclusions of the previous chapters are described and recommendations for further study are given.

## References


[1] Anas and Roy P. Paily. "Simulation of Energy band gap opening of Graphene Nano". In: 2016.

[2] J. Chem. "Electronic and magnetic properties of armchair and zigzag graphene nanoribbons". In: *Phys.* 128.194701 (2008).

[3] R. H. Dennard et al. "Design of ion-implanted MOSFET's with very small physical dimensions". In: *IEEE Journal of Solid-State Circuits* 9.5 (1974), pp. 256–268.

[4] Toshiaki Enoki et al. "Role of edge geometry and chemistry in the electronic properties of graphene nanostructures". In: *Faraday Discuss.* (July 2014). DOI: 10.1039/C4FD00073K.

[5] Mitsutaka Fujita et al. "Peculiar Localized State at Zigzag Graphite Edge". In: *Journal of the Physical Society of Japan* 65.7 (1996), pp. 1920–1923. DOI: 10.1143/JPSJ.65.1920.

[6] Melinda Y. Han et al. "Energy Band-Gap Engineering of Graphene Nanoribbons". In: *Phys. Rev. Lett.* 98 (20 May 2007), p. 206805. DOI: 10.1103/PhysRevLett.98.206805.

[7] Xiaoting Jia et al. "Controlled Formation of Sharp Zigzag and Armchair Edges in Graphitic Nanoribbons". In: *Science* 323.5922 (2009), pp. 1701–1705. ISSN: 0036-8075. DOI: 10.1126/science.1166862.

[8] Yande Jiang, Nicoleta Cucu Laurenciu, and Sorin Cotofana. "Complementary Arranged Graphene Nanoribbon-based Boolean Gates". In: *2018 IEEE/ACM International Symposium on Nanoscale Architectures (NANOARCH)* 18402103 (2018).

[9] Erjun Kan, Zhenyu Li, and Jinlong Yang. "Graphene Nanoribbons: Geometric, Electronic and Magnetic Properties". In: *Physics and Applications of Graphene - Theory* 10.5772/14112 (2011).

[10] Erjun Kan, Zhenyu Li, and Jinlong Yang. "Graphene Nanoribbons: Geometric, Electronic, and Magnetic Properties". In: Mar. 2011. ISBN: 978-953-307-152-7. DOI: 10.5772/14112.

[11] Jungpil Kim et al. "Distinguishing Zigzag and Armchair Edges on Graphene Nanoribbons by X-ray Photoelectron and Raman Spectroscopies". In: *ACS Omega* 3.12 (2018), pp. 17789–17796. DOI: 10.1021/acsomega.8b02744.

[12] Xiaolin Li et al. "Chemically Derived, Ultrasmooth Graphene Nanoribbon Semiconductors". In: *Science* 319.5867 (2008), pp. 1229–1232. DOI: 10.1126/science.1150878.

[13] Yan Li et al. "Electronic and Magnetic Properties of Zigzag Graphene Nanoribbons on the (111) Surface of Cu, Ag, and Au". In: *Physical review letters* 110 (May 2013), p. 216804. DOI: 10.1103/PhysRevLett.110.216804.

[14] G. E. Moore. "Progress in digital integrated electronics [Technical literaiture, Copyright 1975 IEEE. Reprinted, with permission. Technical Digest. International Electron Devices Meeting, IEEE, 1975, pp. 11-13.]" In: *IEEE Solid-State Circuits Society Newsletter* 11.3 (2006), pp. 36–37.

[15] K. S. Novoselov et al. "Electric Field Effect in Atomically Thin Carbon Films". In: *Science* 306 (2004), pp. 666–669.

[16] K. Rupp and S Siegfried. "The economic limit to Moore's law". In: *In IEEE Transactions on Semiconductor Manufacturing* 24 (2011), pp. 1–4.

[17] Young-Woo Son, Marvin L. Cohen, and Steven G. Louie. "Energy Gaps in Graphene Nanoribbons". In: *Phys. Rev. Lett.* 97 (21 2006), p. 216803.

[18] Hippolyte Tsague and Bhekisipho Twala. "Investigation of carrier mobility degradation effects on MOSFET leakage simulations". In: *International Journal of Computing* 15 (Jan. 2016), pp. 237–247.

[19] Katsunori Wakabayashi et al. “Electronic and magnetic properties of nanographite ribbons”. In: *Phys. Rev. B* 59 (12 Mar. 1999), pp. 8271–8282. DOI: 10.1103/PhysRevB.59.8271.

[20] Zhiping Xu. “Fundamental Properties of Graphene”. In: Jan. 2018, pp. 73–102. ISBN: 9780128126516. DOI: 10.1016/B978-0-12-812651-6.00004-5.

# Chapter 2

# Background information

The aim of this chapter is to provide a literature survey that follows the order in which a substrate can be prepared from design to a real device. First, the growth methods of single-layer graphene are discussed. Second, the available transfer techniques and their influence to the graphene lattice are described. Next, the patterning methods and their limitations are summarised. Finally, a theoretical study of the available characterisation techniques is provided.

## 2.1 Growing methods of graphene

The first theoretical model of a single-layer graphite (named graphene later on) was first proposed back in 1947 by P. R. Wallace et al [52]. This research was the starting point of understanding the electrical properties of graphene. One year later, the first observations using electron microscopy of a few layer graphene sheets was made. The first attempts for growing of graphene was performed since 1970 by using epitaxial growth on top of other materials (substrate) [40]. However, it was observed that the graphene was damaged due to significant amount of charge transfers from the substrate.

Currently, many different methods exist for preparing graphene that has various shapes, size and quality. These methods can be divided into two categories, namely bottom-up and top down methods as shown in figure 2.1. Bottom-up methods are used to assembly nanomaterials from atomic scale with high precision. In this group the most common used methods are epitaxial growth and chemical vapor deposition (CVD) which are able to create large-size graphene films with high controllable thickness [16].

Top-down approach is a process for breaking down bulk materials into smaller peaces while retaining the properties of the material [38]. Such methods consist of exfoliation and micro mechanical cleavage of bulk pristine graphite or chemically treated graphite in order to obtain single-layer or few layers of graphene. The direct liquid-phase exfoliation (LPE) enables large-scale production of micro meter-sized graphene films. The working principle of the LPE consist of applying external forces to bulk graphite in order to break the van der Waals interactions between the adjacent graphene layers. This enables to break the graphite directly without using oxidation [56]. However, direct LPE usually leads to a mixture of single-layer to multi-layer graphene, with majority of multi-layer graphene. Typically this results in a poor total yield per volume of solvent [12].

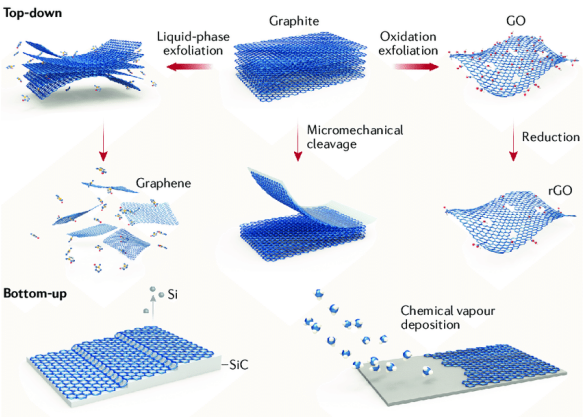


Figure 2.1: Fabrication processes for extracting graphene (adapted from [56])

### 2.1.1 Mechanical exfoliation

The first successful attempt to extract a single-layer atom thick graphene from Highly Ordered Pyrolytic Graphite (HOPG) was made by Geim and Novolesov in 2004 by using a micro-mechanical cleavage process [42]. The idea behind this process is to separate graphene layers from the bulk HOPG as visualised on figure 2.2. The exfoliation process in this method is using a scotch tape applied on the surface of the bulk HOPG. This is followed by numerously repeating the normal force on the scotch tape from which the graphitic layer becomes thinner and thinner and finally it will become single-layer graphene.

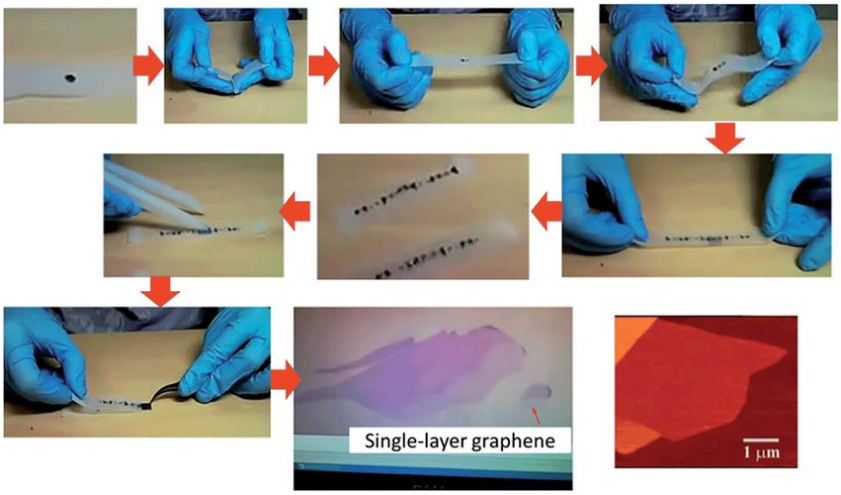


Figure 2.2: Extracting single-layer of graphene using micro-mechanical cleavage process (adapted from [61])

Using micro-mechanical cleavage a large-area of graphene is possible to be extracted. Based on the samples produced using this method, many of the phenomenal properties have been discovered such as very high electrical conductivity, low resistivity, extremely high current densities, inherent strength and ability to absorb a rather large percent of white light. In addition, Novoselov et al. [42] reported that the mobility of charge carriers in graphene can exceed 15000 $cm^2$ $V^{-1}s^{-1}$ at room temperature. However, due to doping of the graphene surface, carrier mobility can vary widely from 100 to 20000 $cm^2$ $V^{-1}s^{-1}$ [9].

A disadvantage of the mechanical exfoliation method is the lack of control over the size, the number of single-layer crystals and the randomness of their location on the substrate. Stating this disadvantage might seem that the method become unreliable for single-layer graphene, but due to the high number of flakes transferred to the

substrate, single-layer graphene is very likely to be found. In addition, this method is only suitable for usage in laboratory research, because it is very time consuming and labour-intensive.

### 2.1.2 Reduction of graphite oxide

Another top-down method for synthesising single-layer graphene is by reduction of graphite oxide. Using sonication, graphite oxide can be exfoliated to single or few layer graphene.

The oxidation of graphite to graphite oxide is typically performed using Hummers' method [62], followed by exfoliation into single-layered graphene oxide (GO), which extends over micrometres in almost quantitative yields. This is an advantage of the reduction of GO methods compared to the LPE method, which does not have high yield for single-layer graphene. GO can be easily treated chemically with hydrazine and/or by thermal annealing. Single-layer graphene produced using this methods shows charge-carrier mobility of more than 1,000 $cm^2$ $V^{-1}s^{-1}$. This methods is mainly used for production of graphene based electrochemical sensors and can find suitable uses for composites, coatings, batteries and super capacitors [56]. During the process graphene is functionalized with oxygen groups, which leads to changing the material properties [47].

### 2.1.3 Chemical vapour deposition

As mentioned earlier chemical vapour deposition (CVD) is one of the most commonly used methods from the bottom-up approaches. CVD successfully removes some of the difficulties and limitations that are introduced by the mechanical exfoliation method. The working principle of the process starts with a carbon-containing gas on a metal catalyst (e.g. Cu or Ni) surface at high temperatures. The gas reacts with the surface and some of the carbon atoms attached to the substrate surface at certain locations. Eventually, other carbon atoms bond to the ones already deposited on the substrate which forms the honeycomb structure of graphene [49].

Compared to the mechanical exfoliation the size of the graphene film can reach `cm` lengths and it is much more promising for scaling up. Some of the advantages of this methods are low defects, good uniformity, and control over the number of graphene layers. However, still it is a challenge to control the deposition of each individual atom in order to form a "perfect" honeycomb structure which leads to degradation of the electronic and optical properties. CVD growth graphene is created on metal catalyst, which requires a transfer to a target substrate (eg $SiO_2$) for further patterning. The process of transferring is still in development and causes lattice damages, impurities and polymer contamination. This leads to CVD growth graphene to show a lower carrier mobility that ranges from 100 to 1000 $cm^2$ $V^{-1}s^{-1}$ [54].

### 2.1.4 Chemical self-assembly

Chemical self-assembly is a bottom-up approach that can be used for creation of graphene grains starting from the individual atoms. The approach uses the molecules of the material and by their own interaction, it allows forming a large scale complex structure, when certain environmental conditions are met during the assembly process. The driving forces working behind the self-assembly process of graphene are inter-layer $\pi - \pi$ bonds, electrostatic forces and dipole-dipole interactions. With the assistance of this driving forces it is possible to create hierarchical composites possessing unique structures and functions.

Graphene sheets have double-sided functionalization in self-assembly processes, which allows for layer by layer coordination assembly. Usually, the self-assembly process for graphene arrays is developed directly on gold surfaces [55]. However, physical and chemical modification are required in order to ensure the targeted assembly architecture for graphene [41].

## 2.2 Transferring methods of growth graphene to another substrate

In general, there are two methods used as a transfer process namely carrier or stamp method. Both methods are visualised in figure 2.3.

The carrier method uses a thick organic film such as polymethyl-methacrylate (PMMA) to cover the graphene layer on the growth substrate. When the film is placed, the growth substrate is etched away with inorganic acid without introducing damages to the resist or to the graphene. Once, the growth substrate is removed, the resulting stack of resist and graphene is placed on top of a desired substrate (eg $SiO_2$). An important part of the process is the selection of the organic film which should be relatively easy to remove without damaging the graphene structure. The mechanical strength should be also precisely applied, in order to ensure that the graphene remains with the same quality on the selected substrate. Applying a large mechanical force will cause extending of the carbon to carbon distance and change the properties of the material [36].

The stamp method uses polydimethylsiloxane (PDMS) as a resist on the growth substrate, before the substrate is etched away. Similar to the carrier method, the remaining part of resist and graphene is placed on top of the desired substrate. The stamp is later on removed using mechanical detachment [8].

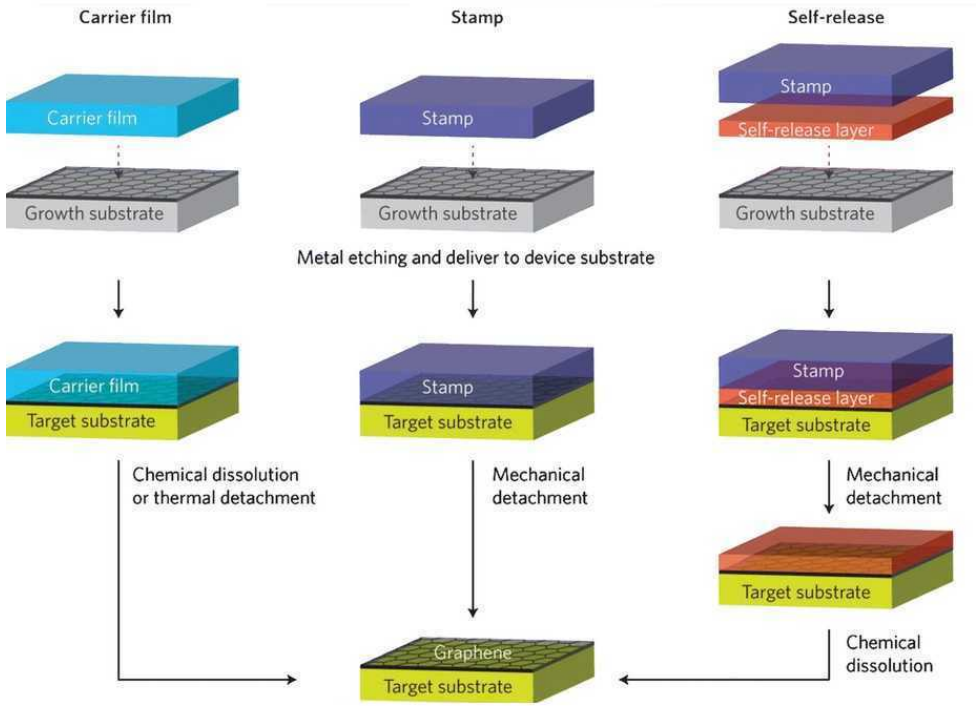


Figure 2.3: Carrier and stamp methods for transferring graphene from growth substrate to the selected substrate for further processing (adapted from [11])

For both methods the transfer film serves as a mechanical support for the graphene, which should guarantee a defect-free placement. Nevertheless, the transfer polymer after removal from the desired substrate can leave residuals. Moreover, because of the treatment with aggressive chemicals for the resist removal, an extensive cleaning is necessary. Considering this, the transfer process to another substrate inevitably will introduce defects in the graphene.

In addition, the current production of synthetic graphene films are typically poly-crystalline [22], that consists of many single-crystalline grains separated by grain boundaries. Such poly-crystalline graphene film is obtained in case graphene is growth using CVD (section 2.1.3). In CVD, the grains nucleate from random and uncontrolled locations. Eventually, the grains will become large enough and two consecutive grains will form a grain boundary.

The grain boundaries between two grains could be complete overlapping or that they are very close to each other. The expectation of the formed grain boundaries is to degrade the mechanical and electrical properties of the resulting poly-crystalline graphene due to formation of non hexagonal rings [3].

## 2.3 Patterning of graphene

Digital electronics applications such as Boolean logic gates require a sufficient band-gap in order to switch off the device for proper operation. Therefore, further modification of the transferred graphene is required.

Features like GNR alignment, width control, aspect ratios, ribbon to ribbon variations are essential to control the electronic characteristics of the fabricated devices and their use as Boolean logic gates. In this section, two methods are discussed including their advantages and limitations. In addition, the currently available etching techniques are presented.

### 2.3.1 Photo-lithography

Optical lithography is a process that uses UV light as a source to transfer a pattern on a substrate via a photo-mask. The first step of the process is coating the substrate with a photo-resist, which is a polymer sensitive to light exposure. The pattern size is dependant from the photo-mask, which makes this technology currently less preferable for patterning GNR devices.

### 2.3.2 Electron beam lithography

Electron-beam lithography (EBL), a technique that originates from scanning electron microscopy (SEM), is a direct writing method to draw a custom patterns on a surface covered with an electron beam sensitive film called resist. There are two types of resists namely positive resist that uses material like polymethyl-methacrylate (PMMA) and negative using hydrogen silsesquioxane (HSQ) as a resist [33]. The focused electron beam on the surface changes the solubility of the resist, which provides a selective removal of either the exposed region in case of positive resist or of the non-exposed region when negative resist is coated on the sample surface. The exposure process of positive and negative resist is presented in figure 2.4. In addition, when the damaged resist is removed with developing, the exposed parts are etched in order to form the desired graphene pattern.

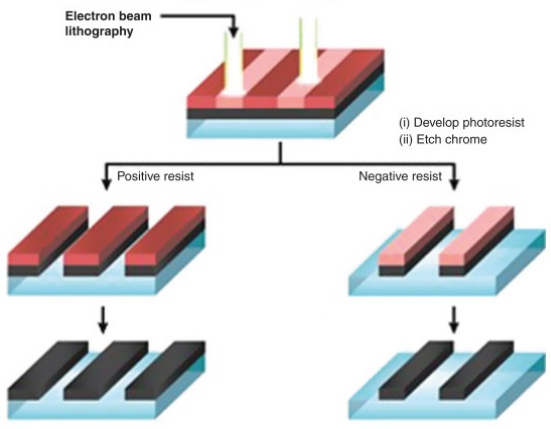


Figure 2.4: E-beam lithography removal of the coated positive or negative resist and further etching the exposed parts

EBL allows simultaneously to pattern different design on one wafer. The simultaneously patterning is also possible in photo-lithography, but the real strength of the EBL is that it allows to program the beam directly. For optical lithography a mask has to be made with the required patterned design, which usually is build using EBL. However, this process of patterning could not be used in industrial scale as it is a slow and expensive process.

One of the most important features of the e-beam lithography is to have a stable high-quality beam source produced by electron gun . The ideal gun should be capable to achieve high brightness, high uniformity, small spot size, stability and reliability. In order to detach electrons from the cathode of the gun, the cathode should be either exposed to high temperature or a large electric field should be applied through it [1]. To turn on and off the beam usually after the electron gun, beam blanks are placed in form of plates. Magnetic lenses are used to adjust the spot sizes by either focus or deflect the moving electrons from the gun.

Today EBL systems are capable to achieve a spot size below 5 nm [2]. However, the spot size can be limited from various factors such as scattering. When electrons enters the resist a series of "low energy collisions" is started that cause electrons to deflect [14]. In addition, some fraction of the electrons do not penetrate deeply into the substrate and can cause exposure microns away from the initial spot. This leads to proximity effect where electrons writing a feature at one location increase the exposure at a nearby feature, causing pattern distortion and overexposure [43]. Therefore, the accuracy of EBL is correlated also with the resist thickness. Another limiting factor of the spot size can be caused from secondary electrons which occurs from ionisation of the incident electron with the resist [14].

In addition, electron-beam irradiation can degrade the electrical transport properties of single-layer graphene. It was experimentally shown that the irradiation causes decreasing of the charge neutrality point, due to doping of the graphene [10]. In every material the charge neutrality point is referred to a position in the Fermi energy, where the material is charge neutral. The principle of charge neutrality states that the sum of positive charges must be equal to the sum of negative charges. In high-quality single-layer graphene the charge neutrality point is usually very close to 0V. A more detailed explanation of the Fermi levels will be provided in Chapter 3.

### 2.3.3 Graphene etching

To remove part of material's surface an etching process is used. Etching can be divided into two types: wet and dry etching. Wet etching is an isotropic process that uses liquid chemicals to remove substrate material. It requires large amounts of etchant chemicals that should be consistently replaced in order to keep constant etching rate. This leads to very high chemical and disposal costs.

Dry etching uses plasma or etch-ant gases that removes the substrate material in form of a gas. The advantages of using the dry etching process are that consume small amount of chemicals for etching and is possible to achieve high resolution and cleanliness. Considering the advantages of the method and the fact that most of the wet etching chemicals does not react with graphene or are very likely to make a reaction with the resist itself, the research related to graphene etching is focused on processes that utilise the dry etching method.

Plasma etching is a process with short reaction time that provides the ability to modify only the top layer of the surface, uniformly. The most promising etching method to remove the exposed parts of the graphene is oxygen plasma .With oxygen plasma, etching of single- to multi-layer graphene shows good results on various substrates such as $SiO_2$ [39] or on $SiC$ [46].

Liu et al. [32] was able to obtain 10nm GNRs using negative resist combined with oxygen plasma etching. Bai et al. [5] used chemically synthesized nanowires to create a mask on graphene film and further etch it with oxygen plasma. Based on the conducted measurements they observed that the electrical characteristics of the device strongly depend on the GNR width. Devices that have sub-10 nm channel widths have much higher $\frac{I_{on}}{I_{off}}$ ratio compared to devices with larger widths. Yang et. al. [60] shows a reduction of multi layer to single-layer

graphene using nitrogen plasma and post-annealing with a mixture of argon and oxygen plasma in 900°C. Lim et al. [59] utilised a neutral beam assisted atomic layer etching technology using oxygen plasma for radical absorption and desorption in combination with argon neutral beam irradiation to achieve a single graphene layer. Atomic layer etching process based on chemical adsorption by low energy oxygen plasma (0 to 20 eV) followed by psychical desorption with low energy argon (11.2 eV) was observed to reduce one graphene layer per iteration [26].

Apart from oxygen plasma etching, other methods are used for etching graphene such as hydrogen plasma supported with argon [58], He plasma [34] and thermally activated Fe particles [15]. All of this solutions were able to create patterns with highly introduced defects.

The only etching process that showed results for pristine graphene is remote hydrogen plasma [35]. The authors present a method that is capable of etching three layer graphene into hexagonal shapes with zigzag edge termination. They observed that at low etching temperatures the energy was not enough to overcome the reaction barrier in order to break the carbon-carbon bonds. On the other hand, using high temperature during the etch process suppresses the formation of $sp^3$-hybridized carbon and methane. Both effects contribute to reduced etching rates. They found out that the etching rate for zigzag edges in hydrogen is slowest compared to other edge configurations due to their density. The kinetics of the etching reaction is affected only by the intrinsic properties of graphene from which they found out that armchair edges are the ones with the highest etching rate [35].

## 2.4 Characterisation of graphene

The section describes the methods used to evaluate the quality, detection of single-layer-graphene and different microscopy processes for characterisation.

### 2.4.1 Determine the quality of graphene

Raman spectroscopy has been used for many years as a method to observe and determine the structural and electronic characteristics of graphene [44, 45]. Raman spectroscopy can be used to determine the number of layers, quality, edge orientation and other properties.

The principle behind the spectroscopy is based on the Raman effect, which occurs when an external light enters in a molecule and interacts with electron or phonon. This leads to vibrational and deformation of frequency shift from which the incident photon changes the electron state to "virtual state" and re-emission of it leads to Raman or Rayleigh scattering. There are two types of scattering observed from the Raman effect namely Stokes and anti-Stokes scattering [4].

Stokes scattering occurs when the molecules are excited from the initial state into the "virtual state" and later on shift back to the higher vibrational excited state. In case the molecules are already in the vibration state the anti-stokes scattering occurs, which is the same as Rayleigh scattering where the scattered light have the exact same frequency as the initial vibrational state. Anti-Stokes are less likely to occur then Stokes, because it requires the molecule to be in excited state in the first place [13].

In figure 2.5 are present all of the known graphene peaks and their position at the Raman shift. The D peak observed at approximately 1350 $cm^{-1}$ is caused due to the presence of some disorder to the $sp^2$ graphene structure and it can be used as a indication for defects introduced to the graphene. For instance, in a perfect graphene structure this peak disappears. The intensity of the D peak is highly dependent from the orientation of the edges. It was observed that for armchair edges the peak is more intense compared to the peak intensity for zigzag edges [6].

The D' band can be observed at 1620 $cm^{-1}$ in case that in the graphene structure exists randomly distributed impurities or surface charges. Experimental results suggests that the ratio of D and D' bands, can provide information of the type of defects such as changes in the carbon hybridisation from $sp^2$ to $sp^3$, grain boundaries, vacancies and implanted atoms [17].

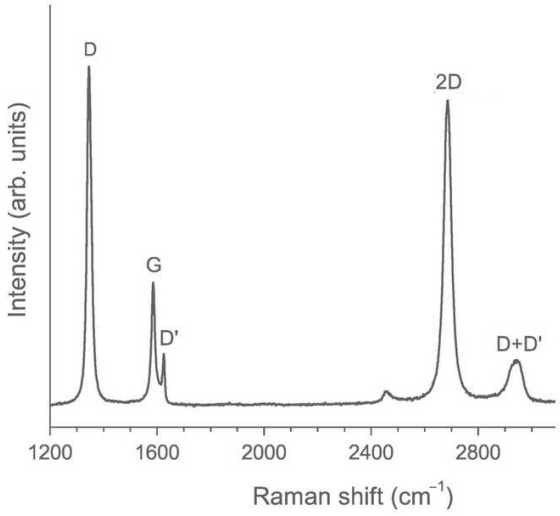


Figure 2.5: Known graphene peaks measured with Raman spectroscopy (adapted from [23])

The G band arises due to the stretching of the carbon-carbon bond and it is highly sensitive to strain effects. The intensity of the G band depends from the graphene thickness and can be used to determine the number of graphene layers [51]. However the G band intensity is affected also by annealing conditions and it is temperature dependent. In order to avoid thermal effects during Raman measurements weak laser beam should be used. [21]. Experimental results shows that the frequency of the G band is affected by doping for which shifting of the peak is observed [18].

The 2D peak originates from the graphitic chemical structure and its shape depends on the number of graphene/graphite layers. It was experimentally observed that the peak for a single-layer graphene is much more intense and sharper compared to multi-layer graphene [51]. Doping can contribute to increase of the 2D spectral width and can be used indirectly to determine the type of doping. It was observed that the full width half maximum (FWHM) for the 2D peak increases to 34 $cm^{-1}$ for n-doped graphene, while p-doping shows expression of 38 $cm^{-1}$ [7].

Finally, the D+D' band occurs, because of the two-phonon processes and it can also be used to determine the quality of the graphene.

Common to all $sp^2$ bonded carbon materials are two of the peaks observed by Raman spectroscopy which are located at approximately 1583 $cm^{-1}$ (the G band) and in the range of 2500 to 2800 $cm^{-1}$ (2D band or as it is referred in some research studies G' band). For a single graphene layer the 2D peak is located approximately at 2680 $cm^{-1}$ by using laser with wavelength of 514 nm [27].

Figure 2.6 shows the typical measured peaks of single-layer graphene. The interpretation of the peaks can give a lot of useful information in regards to the graphene structure and the number of layers.

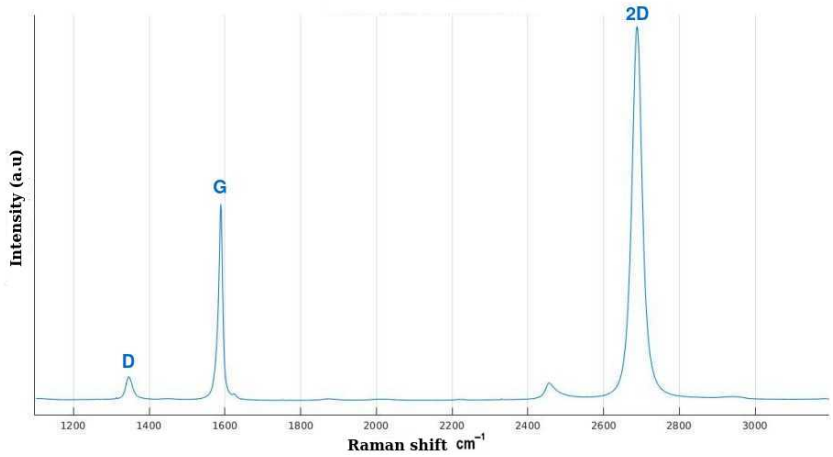


Figure 2.6: Main Raman spectroscopy peaks of single-layer graphene measured with 514 nm green laser.

- The ratio between the intensity of the D and G peaks can be used to characterise the level of disorder in graphene and estimate the amount of defects in carbon materials, such as rips and tears. For single-layer graphene the ratio should be less than 0.1 or ideally 0. ($I_{D/G} < 0.1$) [19].
- An indication for a single-layer of graphene is the ratio between the 2D and G peak which should be larger than 1.5 ($I_{2D/G} > 1.5$) [63]. The relative change in the position of the 2D and G bands result in increase of $I_{2D/G}$ ratio above 2, when graphene is strained [28].
- Analysis of the FWHM of the 2D peak, can be used as a confirmation for the number of layers in graphene. The typical expression of FWHM for single-layer graphene should be 27.5 ± 3.8 $cm^{-1}$. The single-layer graphene can be easily distinguished as the FWHM for bi-layer graphene is observed to be 51.7 ± 1,7 $cm^{-1}$, for tri-layer 56.2 ± 1.6 $cm^{-1}$, for four-layer 63.1 ± 1.6 $cm^{-1}$ and five-layers 66.1 ± 1.4 $cm^{-1}$ [20]. FWHM of the 2D peak is also sensitive to strain and strain fluctuations. It was experimentally observed that the spectral width is broadened at the grain boundaries with width of approximately 36 ± 1.6 $cm^{-1}$ [29].
- The FWHM of the D and G bands is experimentally observed that becomes wider 15-22 $cm^{-1}$ and 16-26 $cm^{-1}$ when single-layer graphene is either stress/strains or doped [48].

### 2.4.2 Scanning tunnelling microscopy

Scanning tunnelling microscopy (STM) is based on the quantum tunnelling effect of the electrons that forms energy barrier between a tip and the surface. With the use of a sharp tip the density of the states can be derived from scanning atomically flat surface [57].

The operational process of the tip is controlled from a feedback system which have a possibility to change the work mode to either using a constant current or constant height. The first mode, readjusts the voltage of the piezoelectric stage which is used to move the tip towards the scanning surface in order to keep the tunnelling current constant. In case, the current decreases, the feedback system will push the tip closer to the surface. On the other hand in constant height mode, the tip is kept at fixed distance on the sample and changes in the tunnelling current are mapped. The STM tools are able to achieve maximum atomic resolution of 0.6 nm for graphene [53]. An example of high resolution image taken with STM is shown in figure 2.7.

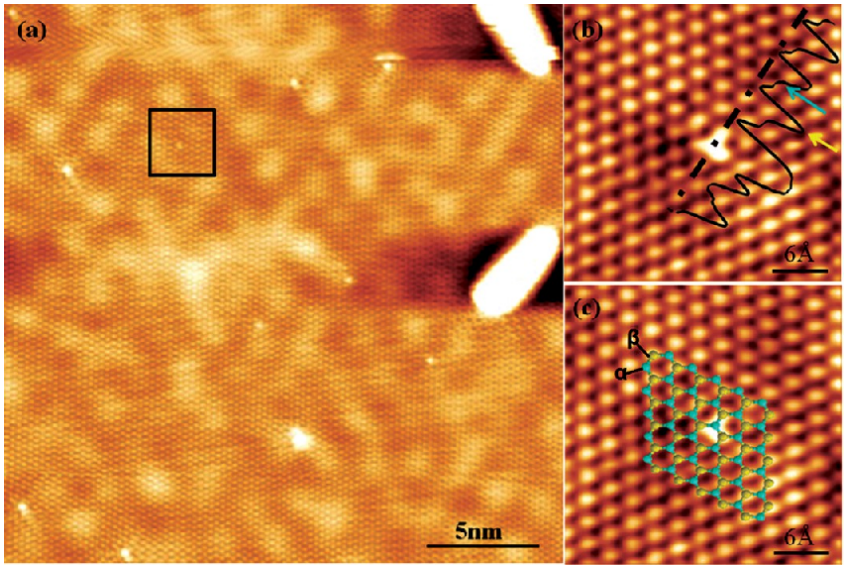


Figure 2.7: Atomically resolved STM images of the structure of single-layer graphene with resolution of 0.6 nm (adapted from [53])

The high atomic resolution allows for further analysis of the image and extract the edge orientation of the graphene grains/patterns. Nevertheless, a conductive path is required to the scanned area in order to obtain an image, which makes this method not suitable for individual graphene nano-ribbon patterns with no contact connection.

### 2.4.3 Atomic force microscopy

Atomic force microscopy (AFM) is a non-interfering and non-contaminating scanning probe microscopy technique for characterizing the topography of a surface using a centilever with attached at the end tip. The formation of the tip is made typically by gluing diamond or gold fragments to the centilever. Due to the occurred attractive or repulsive forces from the tip, the centilever is able to deflect. Compared to the STM, AFM can be applied in broader range of applications, as it can be used for conducting and non-conducting surfaces and it also have the possibility to be used in room environment. The two most common geometries for the tip are rectangular and triangular with 5 to 10 nm lengths. The motion of the tip during scan in each direction is monitored through a reflected laser beam. The reflected beam is tracked by a sensitive photo-detector. For creating a dynamic force mode, the probe is attached to a holder with a shaker piezo which provides the ability to oscillate the probe in a range from 100 Hz to 2 MHz. Depending on the application, AFM can be operated in either contact or non-contact modes.

In a contact mode, similar to the STM either the constant height or the constant current mode can be used. In a non-contact mode (tapping mode), the tip vibrates closely to the surface sample with a distance in order of a few nm. Furthermore, in tapping mode it is possible to measure the frequency modulation or dynamic force microscopy based on the dynamic properties of the cantilever carrying the tip. However, measuring dynamic response using frequency modulation can restrict the operation speed of AFM [50].

A limiting factor for the resolution is in cases when the tip is not sharp enough. This leads to effect known as distortions from which the correct surface topography is not visualised, instead the interaction of the tip with the sample surface is recorded. Distortions are more significant when the tip dimensions are closer to the size of the measured patterns. For this case, a sharper tip is more suitable to be used instead of a dull tip. Furthermore, contamination of the tip can generate profile discontinuities, or tip artefacts that are visualised in the image

topography as generation of new features or repeated patterns. Apart from tip disorders, a shifts of profiles caused by gradual uncontrolled movement over time in horizontal and/or vertical direction, known as drift, can cause a very large amount of distortions. In particular, this is observed when high resolution images of a few hundred nano meter scan range is required. In addition, external noise that originates from different sources such as electrical, acoustical, vibrational or mechanical can also degrade the quality of the image. Finally, disorders can occur in the final image from software manipulations of the data, such as data levelling. The aim of the correction is to remove the tilt that occurs between the microscope in horizontal and vertical scanning plane and the sample surface. Typically the tilt is within 5°, but in some cases it can exceed 15-20°. The removal of the scanned topographies is done by computing the mean plane of the best fitting measured data and subtract the result with each line of individual data. This can cause deformation of the real surface topography [37].

Advantage of the AFM technique is that it permits nano scale movements, and uses a probing tip that can also be used as a micro-tool. This makes it possible AFM to be used in nano scale lithography. AFM-based lithography can ensure spatial resolution of under 10 nm. However, still there are some unresolved problems for application that require high throughput and wider patterning. For instance, the vertical resolution is controllable to sub-nanoscales by the feedback system, but the lateral resolution is mainly dependent on the calibration of the data and does not have a feedback system due to high cost. This introduce a difficulty in controlling the pattern and creating more complex structures than lines [24].

### 2.4.4 Transmission electron microscopy

Transmission electron microscopy (TEM) which includes scanning transmission electron microscopy (STEM) is one of the most promising methods for the characterisation of materials down to the atomic scale. In STEM, a highly focused probe is rastered across the sample using deflection coils. A major requirement for analysis using this method is the correct sample preparation beforehand for which it should be possible for the transmitted electrons to reach the detector through the sample. In case of one layer atomically thick structures such as graphene, any support film would have a stronger contrast in the final image than the graphene itself. With the current widespread availability of chemical vapor deposition (CVD) synthesis of graphene on metal surfaces, [30] the transfer of CVD grown samples to standard TEM grids [31] currently appears to be the most efficient route to obtain free-standing membranes in a TEM-compatible geometry.

The TEM image processing can be divided into two steps:

- Modification of the incoming electrons wave from the sample.
- Further modification of the end wave behind the sample by the optical system of the microscope.

For STEM imaging the steps are reversed, starting from modification of the waves that are hitting the optical system and then process the electrons coming for the sample it self. In case of bright-field imaging both methods provide identical result.

### 2.4.5 Scanning electron microscopy

Scanning electron microscopy (SEM) technique is a method for evaluating the surface morphology. This is achieved through focusing a beam of energetic electrons on the sample. Similar to the electron beam lithography, the electrons are produced from electron gun and passed through a combination of lenses and apertures in order to produce a focused beam of electrons. The beam of electrons interact with the surface of the sample which leads to secondary electrons, back scattered electrons and X-rays. All of this signals are collected from detectors and the final results is formed as an image. Depending on the accelerating voltage the electrons can penetrate the sample to a depth of a few microns, which leads to the effect of secondary electrons and X-rays being produced

[25]. The maximum resolution obtained from SEM depends on multiple factors, like the electron spot size and interaction volume of the electron beam with the sample.

# References


[1] Matteo Altissimo. "E-beam lithography for micro-/nanofabrication". In: *Biomicrofluidics* 4.2 (2010), p. 026503. DOI: 10.1063/1.3437589.

[2] Matteo Altissimo. "E-beam lithography for micro-nanofabrication". In: *Biomicrofluidics* 4.2 (2010), pp. 9785–9791. ISSN: 1932-1058.

[3] Jinho An et al. "Domain (Grain) Boundaries and Evidence of "Twinlike" Structures in Chemically Vapor Deposited Grown Graphene". In: *ACS Nano* 5.4 (2011), pp. 2433–2439. DOI: 10.1021/nn103102a.

[4] Taimur Athar. "Emerging Nanotechnologies for Manufacturing (Second Edition)". In: *Micro and Nano Technologies* (2015), pp. 343–401.

[5] Jingwei Bai, Xiangfeng Duan, and Yu Huang. "Rational Fabrication of Graphene Nanoribbons Using a Nanowire Etch Mask". In: *Nano Letters* 9.5 (2009), pp. 2083–2087.

[6] D. M. Basko. "Boundary problems for Dirac electrons and edge-assisted Raman scattering in graphene". In: *Phys. Rev. B* 79 (20 2009), p. 205428.

[7] Jae Hoon Bong et al. "Facile graphene n-doping by wet chemical treatment for electronic applications". In: *Nanoscale* 6 (June 2014). DOI: 10.1039/c4nr01160k.

[8] B.N. Chandrashekar et al. "A Universal Stamping Method of Graphene Transfer for Conducting Flexible and Transparent Polymers". In: *Scientific Reports* 9 (Mar. 2019). DOI: 10.1038/s41598-019-40408-w.

[9] Bingyan Chen et al. "How good can CVD-grown monolayer graphene be?" In: *Nanoscale* 6 (Oct. 2014). DOI: 10.1039/C4NR05664G.

[10] Isaac Childres et al. "Effect of electron-beam irradiation on graphene field effect devices". In: *Applied Physics Letters* 97.17 (2010), p. 173109. DOI: 10.1063/1.3502610.

[11] J.H. Choi. "Graphene transfer: A stamp for all substrates". In: *Nature nanotechnology* 8 (Apr. 2013). DOI: 10.1038/nnano.2013.74.

[12] Artur Ciesielski and Paolo Samorì. "Graphene via sonication assisted liquid-phase exfoliation." In: *Chemical Society reviews* 43 1 (2014), pp. 381–98.

[13] Philippe Colomban and Gwenael Gouadec. "Raman Scattering : Theory and Elements of Raman Instrumentation". In: Jan. 2008, pp. 11–29. ISBN: 978-0-470-45383-4.

[14] Bryan Cord et al. "Limiting factors in sub-10 nm scanning-electron-beam lithography". In: *Annu. Rev. Phys. Chem. IBM J. Res. Dev. J. Chem. Phys* 41 (Jan. 1990). DOI: 10.1116/1.3253603.

[15] Sujit S. Datta et al. "Crystallographic Etching of Few-Layer Graphene". In: *Nano Letters* 8.7 (2008), pp. 1912–1915.

[16] Daniel R. Dreyer, Rodney S. Ruoff, and Christopher W. Bielawski. "From conception to realization: an historial account of graphene and some perspectives for its future." In: *Angewandte Chemie* 49, (2010), pp. 9336–9344.

[17] Axel Eckmann et al. "Probing the Nature of Defects in Graphene by Raman Spectroscopy". In: *Nano Letters* 12.8 (2012), pp. 3925–3930. DOI: 10.1021/nl300901a.

[18] Andrea C. Ferrari. "Raman spectroscopy of graphene and graphite: Disorder, electron–phonon coupling, doping and nonadiabatic effects". In: *Solid State Communications* 143.1 (2007). Exploring graphene, pp. 47–57. ISSN: 0038-1098.

[19] Andrea C. Ferrari et al. “Raman spectroscopy of amorphous, nanostructured, diamond–like carbon, and nanodiamond”. In: *Philosophical Transactions of the Royal Society of London. Series A: Mathematical, Physical and Engineering Sciences* 362.1824 (2004), pp. 2477–2512. DOI: 10.1098/rsta.2004.1452.

[20] Yufeng Hao et al. “Probing Layer Number and Stacking Order of Few-Layer Graphene by Raman Spectroscopy”. In: *Small* 6.2 (2010), pp. 195–200. DOI: 10.1002/smll.200901173.

[21] Mingyuan Huang et al. “Phonon softening and crystallographic orientation of strained graphene studied by Raman spectroscopy”. In: *Proceedings of the National Academy of Sciences* 106.18 (2009), pp. 7304–7308.

[22] Pinshane Huang et al. “Imaging Grains and Grain Boundaries in Single-Layer Graphene: An Atomic Patchwork Quilt”. In: *Microscopy and Microanalysis* 17 (Sept. 2010). DOI: 10.1017/S143192761100835X.

[23] Ado Jorio, Luiz Gustavo Cançado, and Leandro M. Malard. “Vibrations in Graphene”. In: *2D Materials: Properties and Devices*. 2017, pp. 71–89. DOI: 10.1017/9781316681619.006.

[24] NORITAKA KAWASEGI et al. “ATOMIC FORCE MICROSCOPE LITHOGRAPHY”. In: *Nanofabrication*, pp. 33–64. DOI: 10.1142/9789812790897_0002.

[25] Shahid Khan. *Scanning Electron Microscopy: Principle and Applications in Nanomaterials Characterization*. Sept. 2018, p. 31.

[26] Ki Kim et al. “Atomic layer etching of graphene through controlled ion beam for graphene-based electronics”. In: *Scientific Reports* 7 (May 2017).

[27] Mafra D. L. et al. “Determination of LA and TO phonon dispersion relations of graphene near the Dirac point by double resonance Raman scattering”. In: *Physical Review B* 76 (2007), pp. 233–407.

[28] Martin Benjamin B.S. Larsen et al. “Transfer induced compressive strain in graphene: Evidence from Raman spectroscopic mapping”. In: *Microelectronic Engineering* 121 (2014). Nano Fabrication 2013, pp. 113–117. ISSN: 0167-9317. DOI: https://doi.org/10.1016/j.mee.2014.04.038.

[29] Taegeon Lee et al. “Spatially resolved Raman spectroscopy of defects, strains, and strain fluctuations in domain structures of monolayer graphene”. In: *Scientific Reports* 7 (Dec. 2017). DOI: 10.1038/s41598-017-16969-z.

[30] Xuesong Li et al. “Large-Area Synthesis of High-Quality and Uniform Graphene Films on Copper Foils”. In: *Science* 324.5932 (2009), pp. 1312–1314. DOI: 10.1126/science.1171245.

[31] Yung-Chang Lin et al. “Clean Transfer of Graphene for Isolation and Suspension”. In: *ACS Nano* 5.3 (2011), pp. 2362–2368.

[32] Guanxiong Liu et al. “Epitaxial Graphene Nanoribbon Array Fabrication Using BCP-Assisted Nanolithography”. In: *ACS Nano* 6.8 (2012), pp. 6786–6792.

[33] Kai Liu, J.L Vicent, and Ivan K Schuller. “Ordered magnetic nanostructures: fabrication and properties”. In: *Journal of Magnetism and Magnetic Materials* 256.1 (2003), pp. 449–501. ISSN: 0304-8853. DOI: https://doi.org/10.1016/S0304-8853(02)00898-3.

[34] Wei Luo et al. “High-precision thickness regulation of graphene layers with low energy helium plasma implantation”. In: *Nanotechnology* 23 (Aug. 2012), p. 375303.

[35] Bangjun Ma et al. “Precise control of graphene etching by remote hydrogen plasma”. In: *Nano Research* (Sept. 2018).

[36] Lai-Peng Ma, Wencai Ren, and Hui-Ming Cheng. “Transfer Methods of Graphene from Metal Substrates: A Review”. In: *Small Methods* 3 (Apr. 2019), p. 1900049. DOI: 10.1002/smtd.201900049.

[37] Francesco Marinello et al. “Error Sources in Atomic Force Microscopy for Dimensional Measurements: Taxonomy and Modeling”. In: *Journal of Manufacturing Science and Engineering-transactions of The Asme - J MANUF SCI ENG* 132 (June 2010). DOI: 10.1115/1.4001242.

[38] Buzaglo Matat et al. “Top-Down, Scalable Graphene Sheets Production: It Is All about the Precipitate”. In: *Chemistry of Materials* 29.23 (2017).

[39] Haider Al-Mumen et al. “Singular Sheet Etching of Graphene with Oxygen Plasma”. In: *Nano-Micro Letters* 6 (Mar. 2014), pp. 116–124. DOI: 10.5101/nml.v6i2.p116-124.

[40] Ayato Nagashima and Chuhei Oshima. “Ultra-thin epitaxial films of graphite and hexagonal boron nitride on solid surfaces”. In: *Journal of Physics: Condensed Matter* 9.1 (1997).

[41] M.J. Nine, T.T. Tung, and D. Losic. “9.04 - Self-Assembly of Graphene Derivatives: Methods, Structures, and Applications”. In: *Comprehensive Supramolecular Chemistry II*. Ed. by Jerry L. Atwood. Oxford: Elsevier, 2017, pp. 47–74. ISBN: 978-0-12-803199-5. DOI: https://doi.org/10.1016/B978-0-12-409547-2.12634-4.

[42] K. S. Novoselov et al. “Electric Field Effect in Atomically Thin Carbon Films”. In: *Science* 306 (2004), pp. 666–669.

[43] Liming Ren and Baoqin Chen. “Proximity effect in electron beam lithography”. In: *Journal of Vacuum Science and Technology* 12 (Nov. 2004), 579–582 vol.1.

[44] Dresselhaus M. S. et al. “Raman spectroscopy of carbon nanotubes.” In: *Phys. Rep.* 409 (2005), pp. 47–49.

[45] Reich S. and Thomsen C. “Raman spectroscopy of graphite.” In: *Philos. T. R. Soc. A* 362 (2004), pp. 2271–2288.

[46] Young Jun Shin et al. “Surface-Energy Engineering of Graphene”. In: *Langmuir* 26.6 (2010), pp. 3798–3802. ISSN: 1520-5827.

[47] Andrew T. Smith et al. “Synthesis, properties, and applications of graphene oxide/reduced graphene oxide and their nanocomposites”. In: *Nano Materials Science* 1.1 (2019), pp. 31–47. ISSN: 2589-9651. DOI: https://doi.org/10.1016/j.nanoms.2019.02.004.

[48] Bo Tang, Hu Guoxin, and Hanyang Gao. “Raman Spectroscopic Characterization of Graphene”. In: *Applied Spectroscopy Reviews* 45.5 (2010), pp. 369–407. DOI: 10.1080/05704928.2010.483886.

[49] James Tour. “Top-Down versus Bottom-Up Fabrication of Graphene-Based Electronics”. In: *Chemistry of Materials* 26 (Sept. 2013), pp. 163–171. DOI: 10.1021/cm402179h.

[50] Ampere Tseng, S.D. Sartale, and M.F. Luo. “Atom, molecule, and nanocluster manipulations for nanostructure fabrication using scanning probe microscopy”. In: Jan. 2008, pp. 1–32. DOI: 10.1017/9789812790897_0001.

[51] Mark T. Wall. “The Raman Spectroscopy of Graphene and the Determination of Layer Thickness”. In: *Materials Science* (2011).

[52] P. R. Wallace. “The Band Theory of Graphite”. In: *physical review* 71.9 (1947).

[53] Wen Wan et al. “Incorporating Isolated Molybdenum (Mo) Atoms into Bilayer Epitaxial Graphene on 4H-SiC(0001)”. In: *ACS Nano* 8.1 (2014), pp. 970–976. DOI: 10.1021/nn4057929.

[54] Chen Wang, Kizhanipuram Vinodgopal, and Guiping Dai. “Large-Area Synthesis and Growth Mechanism of Graphene by Chemical Vapor Deposition”. In: Jan. 2019. ISBN: 978-1-78984-960-8. DOI: 10.5772/intechopen.79959.

[55] Hailiang Wang et al. “Chemical Self Assembly of Graphene Sheets”. In: *Nano Research* 2 (Mar. 2009), pp. 336–342. DOI: 10.1007/s12274-009-9031-x.

[56] Xiao-Ye Wang, Akimitsu Narita, and Klaus Müllen. “Precision synthesis versus bulk-scale fabrication of graphene”. In: *Nature reviews* 2.100 (2017).

[57] J. Wintterlin and M.-L Bocquet. “Graphene on metal surfaces”. In: *Surface Science* 603 (June 2009), pp. 1841–1852.

[58] M. Wojtaszek et al. “A road to hydrogenating graphene by a reactive ion etching plasma”. In: *Journal of Applied Physics* 110.6 (2011), p. 063715. ISSN: 1089-7550. DOI: 10.1063/1.3638696.

[59] Sun Lim Woong et al. “Atomic layer etching of graphene for full graphene device fabrication”. In: *Carbon* 50.2 (2012), pp. 429–435. ISSN: 0008-6223.

[60] Xichao Yang et al. “Layer-by-layer thinning of graphene by plasma irradiation and post-annealing”. In: *Nanotechnology* 23.2 (2011), p. 025704.

[61] Min Yi and Zhigang Shen. “A review on mechanical exfoliation for scalable production of graphene”. In: *Journal of Materials Chemistry A* (2015).

[62] N.I. Zaaba et al. “Synthesis of Graphene Oxide using Modified Hummers Method: Solvent Influence”. In: *Procedia Engineering* 184 (2017). Advances in Material & Processing Technologies Conference, pp. 469–477. ISSN: 1877-7058. DOI: https://doi.org/10.1016/j.proeng.2017.04.118.

[63] Wei Zhou et al. “Ultraviolet Raman spectra of double-resonant modes of graphene”. In: *Carbon* 101 (2016), pp. 235–238. ISSN: 0008-6223. DOI: https://doi.org/10.1016/j.carbon.2016.01.102.

# Chapter 3

# Simulation model

The aim of this chapter is to give detailed explanation to the reader, of how the simulation model for graphene nano-ribbons Boolean logic devices is realised. Furthermore, the model is used to derive a suitable GNR butterfly shapes that can be used for the realisation of complementary Boolean logic gates. This is achieved by simulating each structure that is part of the formation of the device as pull-up and pull-down network and look at how the conductance of each structure changes when external voltage is applied.

## 3.1 Implementation

The model uses iterative approach to derive the current through the graphene when external voltage is applied and from there the overall conductance can be found. The GNR device is considered as ballistic semi-conducting device. In the list below are described the steps taken in consideration during calculation of the model for deriving the overall conductance.

- Electronic band structure
- Electronic states and Fermi level
- Density of states (DOS)
- Charge density through the surface of the graphene

The model of the device is considered as a GNR structure connected between two contacts with different Fermi levels ($\mu_1$ and $\mu_2$). Due to this connection it makes the device out of equilibrium state. The connection of the structure with the contacts is visualised in figure 3.1. The approach used for solving the problem is present in figure 3.2. First, by using a non equilibrium Green function the density matrix is determined. The required parameters to derive the density matrix are the Hamiltonian matrix, voltage potential across the surface,contacts self energy and their Fermi levels. Secondly, the potential is recalculated using Poisson equation and the result is compared with the previous potential [6]. If the difference of the absolute values of both voltages is larger then $30e^{-3}$, the process is repeated starting from recalculating the density matrix with the new potential. Otherwise, it is considered that the computation is converged and the current is calculated in the next step. Each one of this steps and how the matrices are constructed and found, will be discussed in details in the next sections of the chapter.

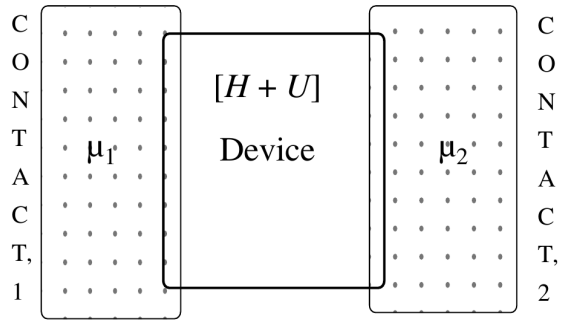


Figure 3.1: GNR device driven out of equilibrium from two contacts with different Fermi levels (adapted from [5])

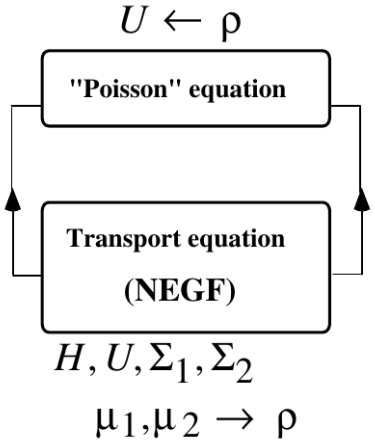


Figure 3.2: Self consistent procedure for determining the density matrix from which the electron density and current can be derived for the overall device (adapted from [5])

### 3.1.1 Electronic band structure

The honeycomb structure of the graphene is formed from a single layer of carbon atoms, that create pattern of repeating hexagons. The number of electrons in one carbon atom are determined by its number in the periodic table (i.e six). The electrons can be separated into core and valence electrons. Two of the electrons are core electrons located in the inner orbital, strongly bounded to the nucleus and does not interact with the neighbouring carbon atoms. The four valence electrons are located in the outer orbitals and therefore interact with the surrounding carbon atoms. All of the electronic and chemical properties of graphene are determined by the valence electrons. These valence electrons are formed from 2s, $2p_x$ and $2p_y$ orbitals [7]. The unit cell consist of two carbon atoms labelled as A and B in figure 3.3. Carbon-carbon distance is known to be `0.42 nm`. The vectors **a1** and **a2** in the Bravias lattice can be calculated with the equations 3.1 and 3.2 where **a** is the inter-atomic carbon distance. The equality of the vectors **a1** and **a2** gives a reciprocal lattice rotated on 90° from the Bravias lattice forming a new vectors **b1** and **b2**. Both new vectors form a first Brillouin zone which characterise the states in a system such as graphene, e.g. phonon or electron states. The reciprocal vectors can be calculated from equations 3.3 and 3.4 [18].

$$a_1 = \frac{a}{2}(3, \sqrt{3}) \tag{3.1}$$

$$a_2 = \frac{a}{2}(3, -\sqrt{3}) \tag{3.2}$$

$$b_1 = \frac{2\pi}{3a}(1, \sqrt{(3)}) \tag{3.3}$$

$$b_2 = \frac{2\pi}{3a}(1, -\sqrt{(3)}) \tag{3.4}$$

The high symmetry points of the reciprocal lattice are given in the figure 3.4 with coordinates shown in 3.5 and 3.6

$$\Gamma = (0,0), M = (\frac{2\pi}{3a}, 0) \tag{3.5}$$

$$K = (\frac{2\pi}{3a}, \frac{2\pi}{3\sqrt{3}a}), K' = (\frac{2\pi}{3a}, -\frac{2\pi}{3\sqrt{3}a}) \tag{3.6}$$

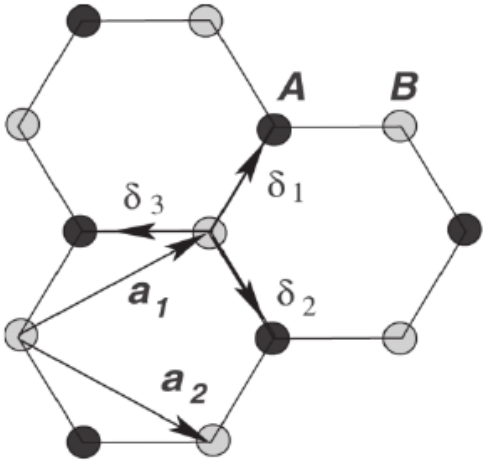


Figure 3.3: GNR honeycomb lattice structure with two carbon atoms A and B per unit cell with lattice vectors **a1** and **a2**. The nearest carbon neighbour vectors from B to A are shown as $\delta_{1,2,3}$ (adapted from [4])

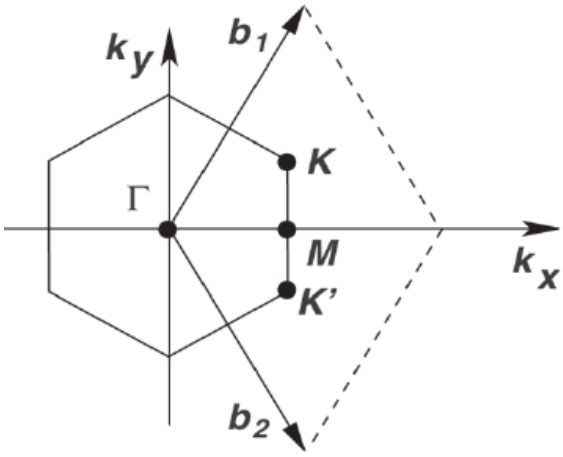


Figure 3.4: GNR reciprocal lattice, with first Brillouin zone spanned by vectors **b1** and **b2** (adapted from [4])

Dirac points are formed for a specific points in the electronic band structure, where two linear bands meet. For graphene, this points are located at the end of the first Brillouin zone at **K** and **K'** points [13]. As graphene crystal structure is 2D, the electrons can have momentum in x and y directions at the points that are at the intersection of two Dirac cones. The touching points between the Dirac cones gives an advantage of graphene in terms of its electronic properties. First, it allows for electrons to easily move between two bands. This means that with applying a small voltage through graphene, more electrons can occupy the upper band and allow for current to flow through the material. Second, when the graphene is in micron meter size and even few hundred nano meters, the two bands causes electrons to behave as massless particles [16]. This is due to the fact that the band near Dirac point is straight, which causes the electrons that are located in these electronic bands to behave as they have zero mass. In other words, this leads to pseudo-spin of the electrons in addition to the normal spin. Due to the introduced pseudo-spin, the electrons behave as chiral electrons. Finally, the aligned bands of the graphene, makes it very efficient in absorbing light.

Apart from the edge of the structure, each carbon atom inside the structure has three bonds with neighbouring atoms. In case of `x-y` plane position of the GNR, the sigma bonds ($\sigma$) correspond to $sp^2$ hybridised orbitals formed from the 2s, $2p_x$ and $2p_y$ orbitals. For graphene, the levels involving these orbitals are decoupled from those that involves $2p_z$ orbitals, which means that there are no corresponding matrix elements in the Hamiltonian coupling for $2p_x$ and $2p_y$ orbitals. In addition, the energy levels of this orbitals are either too far below or above Fermi level, which contribute to the fact that the conductance and valance bands are mainly formed from the

$2p_z$ plane. In $p_z$ orbitals of neighbouring atoms overlap which results in creation of $\pi$ and $\pi*$-bands [6]. This simplified the calculation of the model and conduction and valance bands can be described quite well by using only one plane. Moreover, the number of electrons that can be released per each carbon atom from $2p_z$ plane is known to be only `one`.

The energy band structure of undoped graphene is visualised in figure 3.5, from which it can be seen that the six meeting points are located at the K and K' points from the first Brillouin zone. In figure 3.6 the linear dispersion of the Dirac cones is visualised. Each Dirac cone meets the other one at K points, which forms a canonical-shaped valley [1].

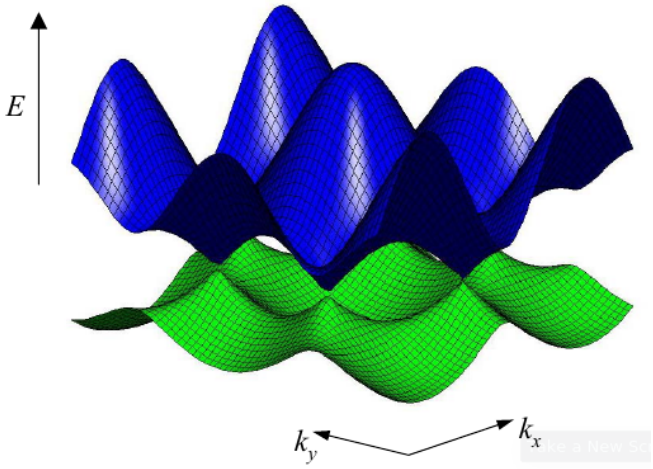


Figure 3.5: 3D relation for graphene $\pi$ energy bands (adapted from [16])

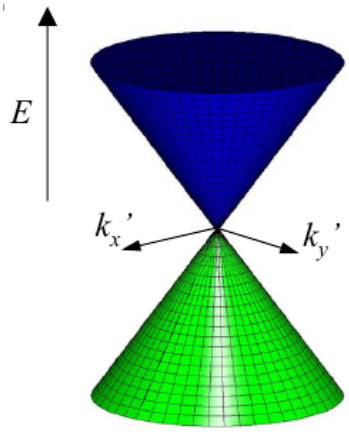


Figure 3.6: Dirac cone projection for low energy near K points (adapted from [16])

The electronic states $\psi$ and the corresponding energy values $E_k$ can be derived by solving the Schrödinger equation 3.7. In further discussion of the simulation model the calculation of the electronic states and energy levels will be described as non equilibrium Green function (NEGF), which is a matrix representation of the Schrödinger equation. The NEGF method is used to model open boundary conditions devices with a description of coherent quantum effects such as confinement, interference and tunnelling. In addition the NEGF method includes scattering of phonons and device imperfections such as roughness, defects and impurities [11]. Moreover, the NEGF formalisation provides a very well defined connection that can be used to calculate the density matrix from which the electron density and current can be obtained [14].

$$H[\psi] = E_k[\psi] \tag{3.7}$$

First let us consider the generation of the Hamiltonian matrix. Semi-empirical tight binding model is used to calculate the electronic band structure of the graphene. The model is using approximation of wave functions, which are derived from the superposition of the isolated atoms located at each atomic site. The atomic wave functions are described as eigenvalues of the Hamiltonian matrix `H` in equation 3.8 [10]. The Hamiltonian matrix `H` describes the electron hopping between nearest-neighbour carbon atoms. For the formation of the matrix are also taken into account the internal and external potentials, applied through top and back gates.

$$H = \sum_{i,j} t_{i,j} \tag{3.8}$$

where $t_{i,j}$ equals zero if atoms are not adjacent, otherwise the atom is set to -2,7 eV.

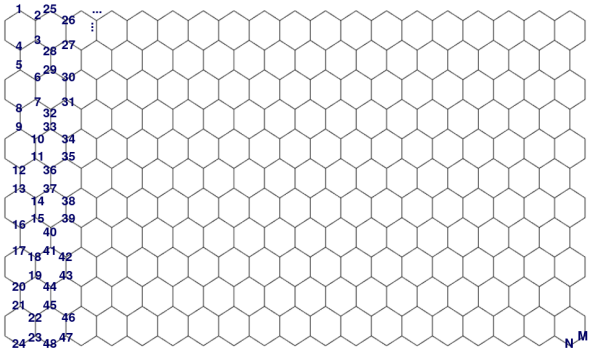


Figure 3.7: GNR sheet

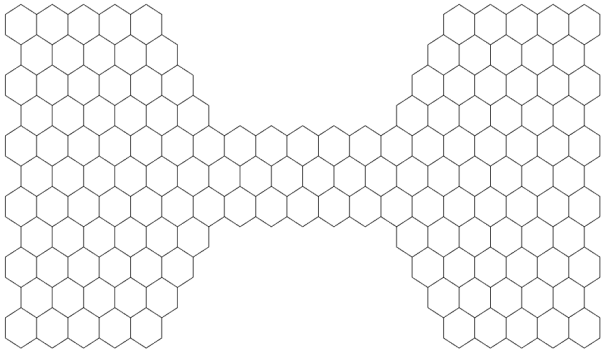

Figure 3.8: GNR butterfly

Initially, all atoms of the GNR are described with the numbering followed as shown in figure 3.7. The numbering of atoms is chosen with respect to the direction of the current flow through the GNR when external voltage is applied. The current direction is going from left to right, perpendicular to the edge orientation. Once the GNR matrix is described in the Hamiltonian, a remove operation is performed, in order to remove the connections of the atoms that are not part of the design of the simulated structure. The removal process is repeated until the desired shape is achieved. In this report, the focus is only limited to butterfly shapes which can be used as building blocks for the realisation of different Boolean logic gates. An example butterfly shape is visualised in figure 3.8. For all of the simulated butterfly shapes the slope between the source/drain contacts and the channel is set to 60°.

The Hamiltonian of the butterfly structure is divided into four sectors as visualised in figure 3.9. The carbon atoms connection for the drain and the source part of the structure are the same with the only difference between them is the indexing of the atoms. Therefore, the matrix representation can be considered as one region and it is generated only once. For the two slopes towards the channel the connection for each column of the GNR is different and this is the reason why, each slope is described as individual sector in the graph. Due to the very large number of atoms for structures above `10 nm`, only a small block of the Hamiltonian for sector `1` is saved. The same applies for the semi-infinite contacts for which the same number of columns as in sector 1 is stored. Otherwise, if the full Hamiltonian for sector `1` is stored it will result in enormous amount of memory usage and simulations are very likely to fail. The reduced Hamiltonian description of sector `1` is believed that it should not affect the final result, as this small block can be re used in the computation of the sector because the atoms have the same bonding (i.e the bonds stored in the Hamiltonian have the same values). For the remaining sectors the atoms in the Hamiltonian are fully described.

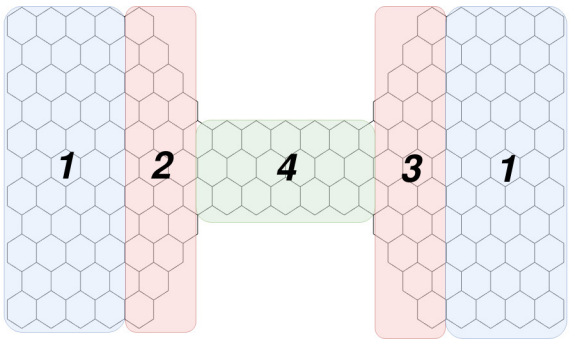


Figure 3.9: Butterfly Hamiltonian construction of the gates and channel

### 3.1.2 Electronic states and Fermi level

The ability of electrons to behave as a charge carriers (i.e the ability of quasi-particle to move freely, carrying an electric charge) depends on the availability of the not occupied electronic states [2]. This phenomena allows for electrons to increase their energy when external electric field is applied through the device and makes them able to flow. The electronic states for a semiconducting structure are shown in figure 3.10. With grey are marked the areas in the filled bands where holes ( empty states ) can be formed. It is known that the holes can also contribute for changes in the conductivity. Holes, are vacancies which are created after an electron leaves its place. The Fermi level $\mathbf{E} = \mathbf{0}$ between the valence and conduction band is marked as $E_f$. Semi-conducting devices that have a small band-gap allows the flow of electrons from valence to conduction band when external energy such as thermal is applied.

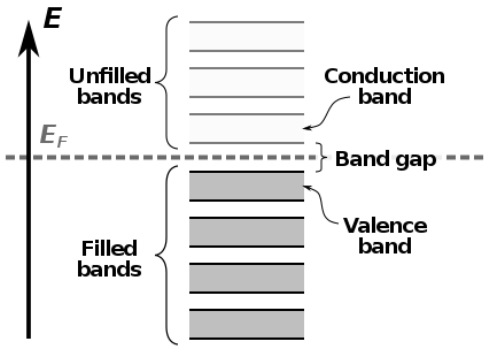


Figure 3.10: Allowed electronic states that can be occupied in a semiconducting device

Fermi level $\mathbf{E} = \mathbf{0}$ is equal to the electrochemical potential $\mu$, which gives information of up to what energy level the allowed states are occupied in respect to its position. The location of the electrochemical potential can be determined by using photo emission measurements which shows how far below the vacuum level this point is located [3].

In case that the source and the drain regions of a device are coupled to the channel, the electrons will flow in and out of the device bringing them all in equilibrium with a common electrochemical potential. In this equilibrium state, the average number of electrons over time in any energy level is typically not an integer, but is described by a Fermi function (equation 3.9) [17]

$$\phi_1(E) = \frac{1}{e^{\frac{E-V_{dd}}{k_B T}} + 1} \tag{3.9}$$

where **E** represent the current energy level point, **V** is equal to the Vdd and $k_B$T is the Boltzmann constant with selected temperature. All the simulations are performed at room temperature.

The energy level points (**E**) are generated as a vector values in range of -5 to 6 with a step of 0.1. The result of the Fermi function is compared with a static value of $1e^{-16}$ and in case the result is less than the compared integer and the range is still in the negative site, the minimum energy level is adjusted to be equal to the current tested energy point. In the opposite case, if the value is larger than the selected integer and the range of the energy level points is in the positive site, the maximum energy level is set to be equal to the current test point. The ranges of the energy level points are selected based on observation of how the minimum and maximum energy values are changing based on the supplied voltage at room temperature.

Once the minimum and maximum energy levels are known, a linear space vector with 50 points between the minimum and maximum energy level points is generated. The linear space vector, defines all levels which are used for further simulation in the model. The number of points is selected based on running experiments with different values and observation that above 50 for a small butterfly structures, the outcome result of the model remains almost the same (the order of magnitude for the conductance does not change).

### 3.1.3 Density of states (DOS)

In the NEGF, open boundary conditions of the device are described in terms of contact self-energies. The interaction of the drain and source contacts with the graphene surface are represent as two matrices with different electrochemical potentials. The channel between the contacts maintains them in local equilibrium. The two matrices in the model are described as $\Sigma_1$ and $\Sigma_2$. The distinction of source and drain contacts from the gate allows to limit the explicit NEGF calculation only to the gate. This allows to reduce the computational load of the model. The method used to calculate the contact self energy of each contact in the model is Sancho-Rubio method, which is based on the assumption of semi-infinite, periodic leads. $\Sigma_1$ and $\Sigma_2$ are calculated using equation 3.10. There are two contacts considered in the calculations namely left (drain) and right (source) which for both of them the interaction with the graphene is described by the Hamiltonian block **1**. The calculation is repeated for all energy levels obtained in the previous step and the result is stored as a matrix representation for each of the contacts. The $g_{n-1}$ is the result of the NEGF, which at the first iteration is set as a fixed very small numerical value. Typically, the Sancho-Rubio method for one contact and energy level should take no more than 40 iterations.

$$\Sigma_N = H_{n,n-1} g_{n-1}, H_{n-1,n} \tag{3.10}$$

By using the result of the contact self energy for both contacts, the NEGF can be solved by considering each sector of the device and each energy level. The result is based on equation 3.11

$$G_R(E) = (EI - H - \Sigma_1 - \Sigma_2)^{-1} \tag{3.11}$$

The energy **E** is a matrix which size is determined by the number of energy level points and the length of the GNR. This matrix represent the slab for each energy point and it is calculated using the equation 3.12.

$$E_{i,k} = E_{l(i)} - U_i + E_{c1} \tag{3.12}$$

where index **i** is used to keep track of the current energy level point and **k** is the current simulated column of the GNR. The calculation repeats until all energy levels and the full length of the GNR is covered. The voltage point **U** is a vector with length equal to the length of the GNR and initially all values of the vector are set to $1e^{-6}$. The energy $E_{c1}$ is a single value point derived from the eigenvalues of the Hamiltonian matrix.

Once the NEGF matrix is known the transmission function **T(E)** can be found using equation 3.13. The transmission function shows the rate at which electrons are transmitted from the source to the drain contacts by propagating trough the device.

$$T(E) = Trace(\Gamma_1 G_R \Gamma_2 G_R^{-1}) \tag{3.13}$$

where $\Gamma_{1,2} = i(\Sigma_{1,2} - \Sigma_{1,2}^{-1})$

Another usage of the NEGF is finding the electrons and holes distribution trough the graphene surface. For this purpose the diagonal values of the NEGF matrix are used and adapted in equation 3.15 and 3.14

$$rho_p = \frac{G_R diag}{2\pi} + (1 - f_1(E)) * step \tag{3.14}$$

$$rho_n = \frac{G_R diag}{2\pi} + f_1(E) * step \tag{3.15}$$

where the step is the difference between each of two levels ( $E_2$ - $E_1$). The total number of electrons and holes are then recalculated and used later on in the calculation of the charge potential in Poisson equation. The Poisson equation is discussed in the next section.

$$P_{total}(E) = P_{total}(E) + rho_p \tag{3.16}$$

$$N_{total}(E) = N_{total}(E) + rho_n \tag{3.17}$$

Initially, the electrons $P_{total}$ and holes $N_{total}$ are set to 0 and after each iteration of the model their values are updated. The updating of the certain element of the vectors depends on the difference between current energy point **E** and the voltage of each column from the surface $U_j$. If the result of this subtraction is larger than 0, the value of $N_{total}$ is updated (equation 3.17). Otherwise, the element of $N_{total}$ remains unchanged and $P_{total}$ is updated using equation 3.16.

### 3.1.4 Charge density through the graphene surface

The charge density represent the potential **U** through the graphene surface by considering the whole device as a stack including the back-gate voltage, substrate ($SiO_2/Si$) and top gates [8]. An example device is shown in figure 3.11

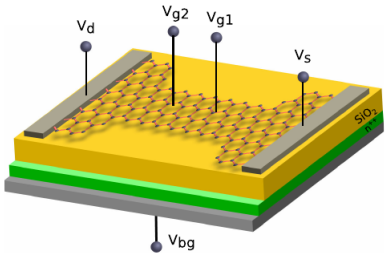


Figure 3.11: Full stack device representation of all layers (adapted from [8])

For this purpose, 3D POISSON calculation is performed, which accounts for the electron to electron interactions through an applied potential. The dimension description of the materials used in the calculation are a standard 300 nm $SiO_2/Si$ insulator, one layer GNR with thickness of one atom and the top gate contacts realised as Cr/Au electrodes. The potential is calculated for each column of the GNR and the outcome result is used in equation 3.12. The calculation of the model repeats from equation 3.10 until the difference of the absolute value of the new voltage point and the old potential is larger than $30e^{-3}$. Otherwise, it is assumed that the model has converged and the channel current can be derived based on the Landauer formula from equation 3.18.[12]

$$I(V) = \frac{q}{h} \int_{-\infty}^{\infty} T(E) * (\phi_1(E - \mu_1) - \phi_1(E - \mu_2)) \tag{3.18}$$

where $\mu_{1,2}$ are the source and drain Fermi energy and $\phi_1(E)$ denotes the Fermi-Dirac distribution function calculated from equation 3.9.

Finally, when current is known the overall conductance of the GNR can be derived using equation 3.19.

$$G = \frac{I}{V_{dd} - V_s} \tag{3.19}$$

## 3.2 Results

This section presents the outcome results of the simulation model and investigate the potential of using GNRs as building blocks for graphene-based Boolean logic gates.

A design space exploration (DSE) is performed in order to match the dimensions of the shape and desired Boolean logic transfer function obtained from the truth table, with the conductance changes when external voltages are applied through the graphene surface (e.g gate voltages). An essential part for a device to be considered as workable is to have $\frac{ON}{OFF}$ ratio higher than 100 between each two states (e.g 0 or 1) [15]. For each simulation the overall conductance of the graphene is mapped to the **ON** and **OFF** state, in which a high conductance represents the switched on state and low conductance represents the off state of the device.

Each Boolean gate is designed using two complementary GNRs, namely pull-up which main purpose is to perform the desired Boolean function and a pull-down that performs that inverse of the pull-up. The pull-down (GNRdn) and pull-up (GNR-up) of a two gate device is visualised in figure 3.12 [9].

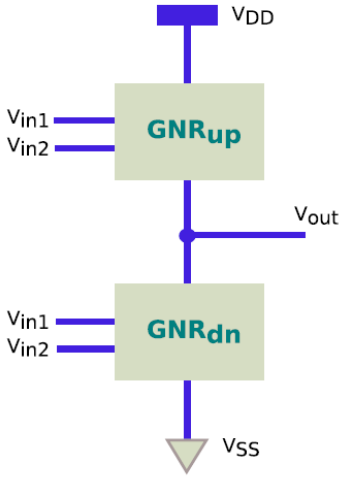


Figure 3.12: GNR complementary two gate Boolean logic device (adapted from [9])

The output voltage of the devices is determined using equation 3.20.

$$V_{out} = V_{dd} * \frac{G_{up}}{G_{dn} + G_{up}} \tag{3.20}$$

The source and the drain contacts are situated between a conduction channel with a zigzag edge orientation. Depending on the desired logic one or two contacts are placed on the channel. From the DSE, five topologies are identified and simulated for various sizes from 10 nm to 30 nm technology and mimic the behaviour of OR,AND,NOR,INVERTER and BUFFER. The technology size shows the smallest part in the structure.

In figure 3.13 are present the butterfly dimension abbreviation used to described the sizes of the channel, source and the drain parts from the GNR structure. This abbreviation will be used later on in the tables to describe the simulated structures. All models are simulated with an angle of **60°** from the source/drain to the gate. This angle is chosen because it shows the best results, as the flow of electrons is focused trough the channel.

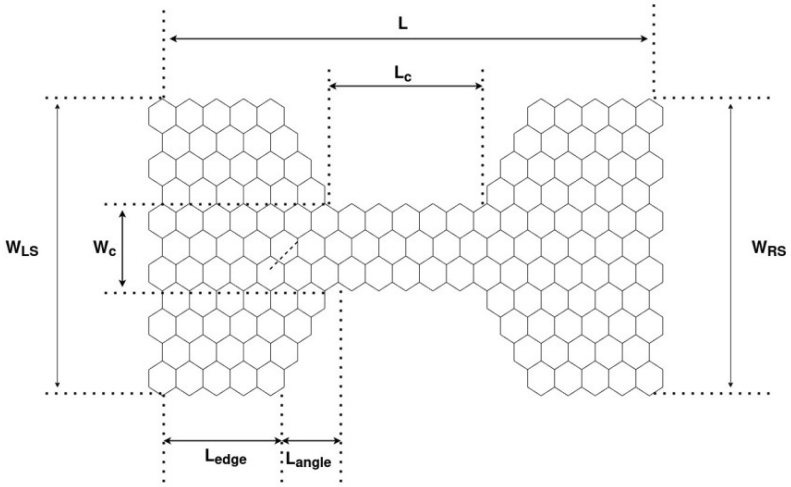


Figure 3.13: GNR dimension description in nm

As in the simulation model the dimension of the source and drain are equally set their width will be noted as `W` as shown in equation 3.21. Later on, both widths will be evaluated in the characterisation process of the fabricated structures.

$$W = W_{LS} = W_{RS} \tag{3.21}$$

### 3.2.1 GNR simulation for 10 nm technology

The dimensions of the structure are presented in **nm** in table 3.1 which includes the width, length of the GNR butterfly, the width and the length of the channel and the overlap of the top gate contacts (channel contacts, drain and source).

Table 3.1: GNR complementary Boolean gates simulation parameters for 10 nm technology

| Structure № | W (nm) | L (nm) | Lc (nm) | Wc (nm) | $L_{edge}$ (nm) | $L_{angle}$ (nm) | Channel Contact (nm) | Drain/Source Contact (nm) |
|---|---|---|---|---|---|---|---|---|
| #1 | 25 | 41 | 10 | 10 | 11.17 | 4.33 | 5 | 5 |
| #2 | 31 | 48 | 14 | 10 | 12.938 | 6.062 | 5 | 5 |
| #3 | 41 | 75 | 30 | 10 | 13.551 | 8.949 | 5 | 5 |
| #4 | 31 | 65 | 23 | 10 | 21.438 | 6.062 | 5 | 5 |

Figure 3.14 shows the conductance changes when external voltage is supplied to the gate. For obtaining the results of both structure the $V_{dd}$ was set to 3V and gate channel voltage is changed from 0 to 3V. It can be seen from the graph that the structure #1 shows a conductance change that can be mapped to behaviour of inverter. Simulation model shows that when the gate voltage is close to 0V the GNR have high conductivity and the opposite occur when the gate voltage is set to $V_{dd}$. Structure #2 have the inverse logic compared to structure #1 in which the conductivity of the graphene surface is low when the channel have voltage equal to $V_{dd}$. Combining both structures they can be used as a pull up network (structure #1) and pull down network (structure #2) and form an inverter Boolean logic.

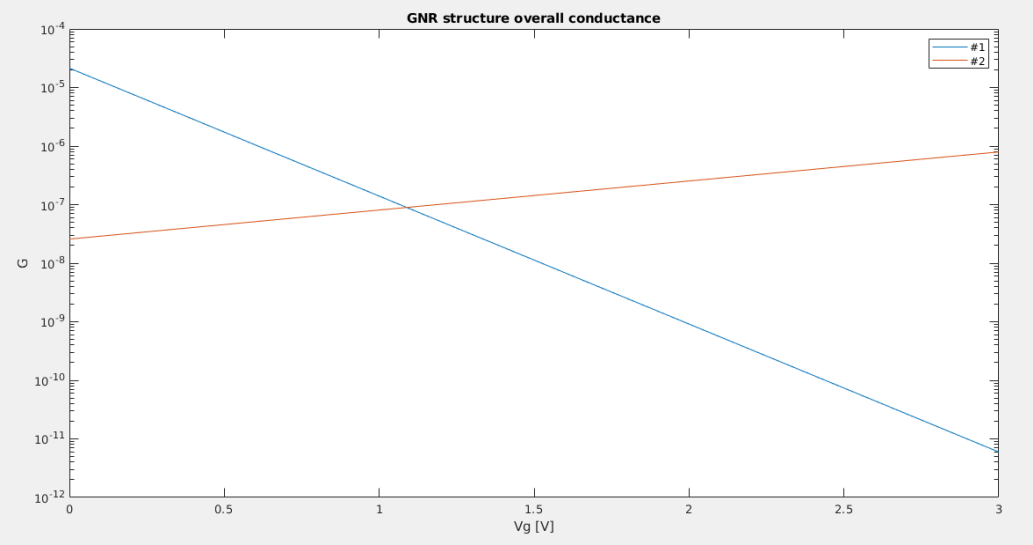


Figure 3.14: Conductance change for different channel voltage levels for structure #1 and #2

The conductance of each carbon atom from the graphene zigzag nano-ribbon structure is mapped to the number of simulated energy levels. The graph of structure #1 and #2 for every gate voltage simulated is visualised in figure 3.15. It can be noted, that for structure #2 the conductance ratio is below 100, which is due to the fact that the conductance distribution is close to 0 in the positive energy level points. The ratio is also affected of the region after -0.8 eV where structure #2 shows regions of the graphene nano-ribbon with high conductance. In structure #1 the ratio for ON and OFF state is above 100, which can be observed from the figure that when $V_{dd}$ is supplied to the gate all regions of the graphene surface conduct.

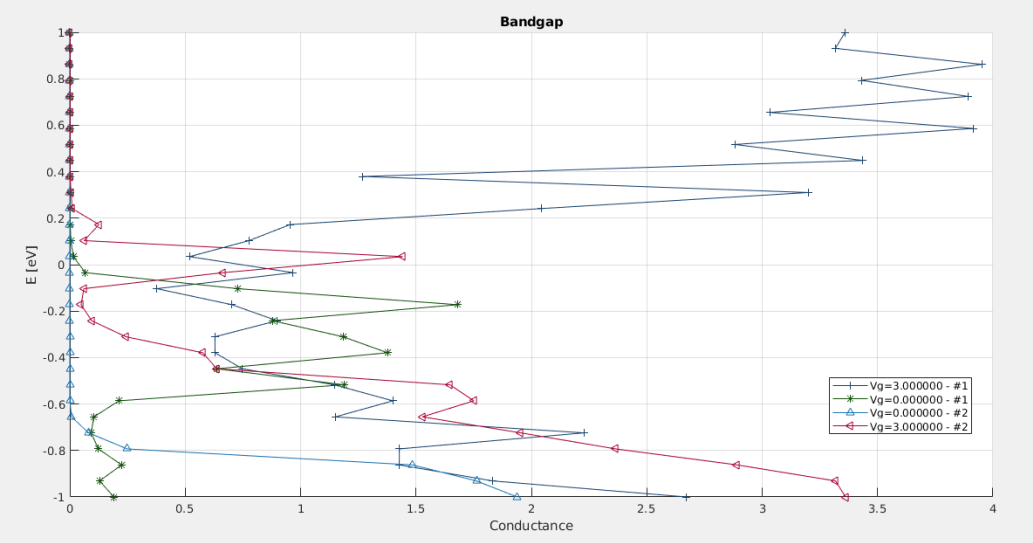


Figure 3.15: Energy level conductance distribution of GNR for structure #1 and #2

Figure 3.16 present the result of the conductance change for structure #3 from the table. For this structure the channel consist of two contacts, where each contact is with length of 5 nm. In addition, the contacts are separated with 10 nm distance from each other and 5 nm distance is left between the slope of the source/drain to the contact.

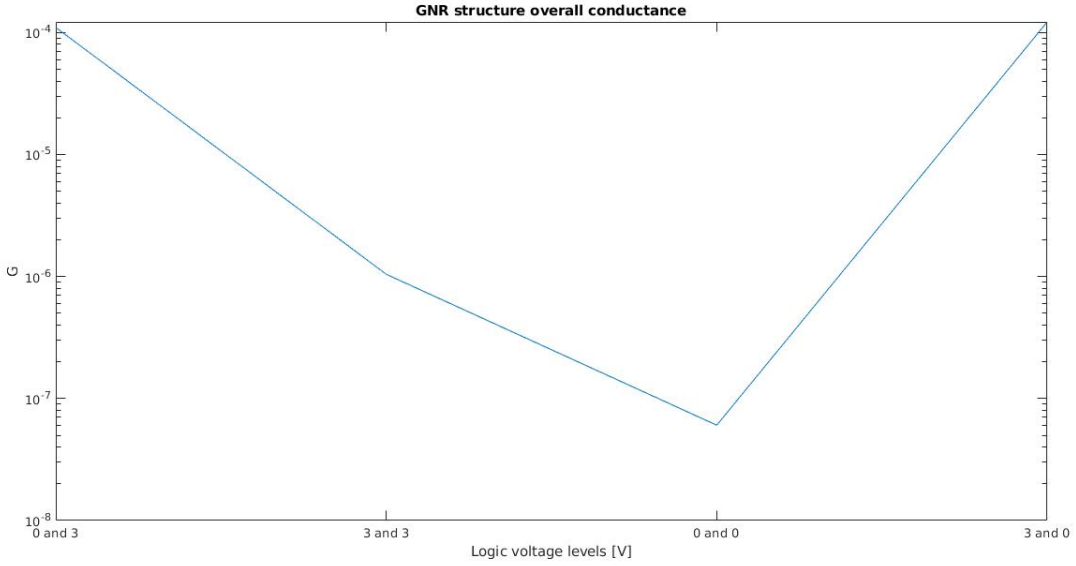


Figure 3.16: Conductance change for different channel voltage levels for structure #3

It can be seen from the energy level conductance distribution in figure 3.17, that when no voltage is applied to the channel contacts, the GNR have an area with conductance close to 0 and for other voltage combinations conductivity in graphene is always observed. This can be mapped to the conductance change from (3.16) where the zero voltages on the channel represent the OFF state of the device and all the rest can be considered as ON state. The behaviour of this structure can be considered as the up network of OR gate.

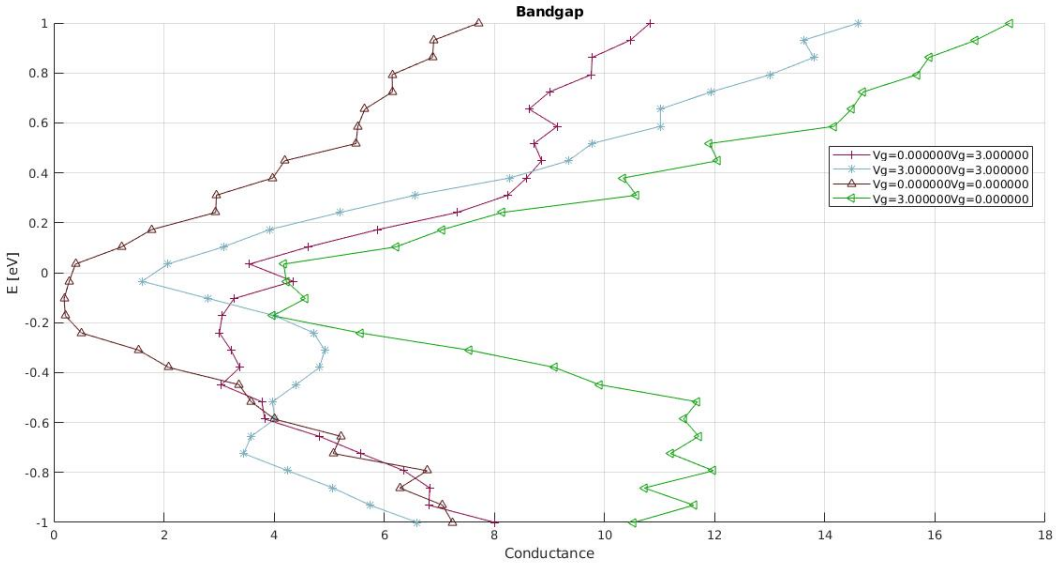


Figure 3.17: Energy level conductance distribution of GNR for structure #3

The opposite conductance change is observed for structure #4. By making the length of the channel and the total length of the structure smaller, the opposite conductance map is obtained. The conductance change is shown in figure 3.18. For this structure the contacts on the channel are kept on 5 nm, however the distance between each contact is reduced to 3nm.

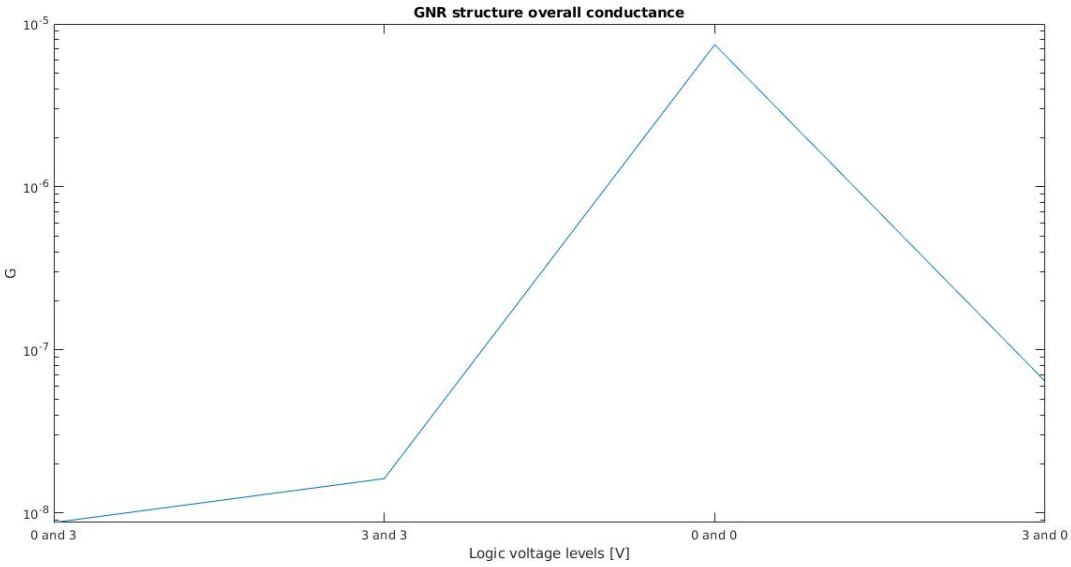


Figure 3.18: Conductance change for different channel voltage levels for structure #4

From the energy level conductance distribution in figure 3.19 we can see that the band-gap does not exist when the gate voltages are set to 0.

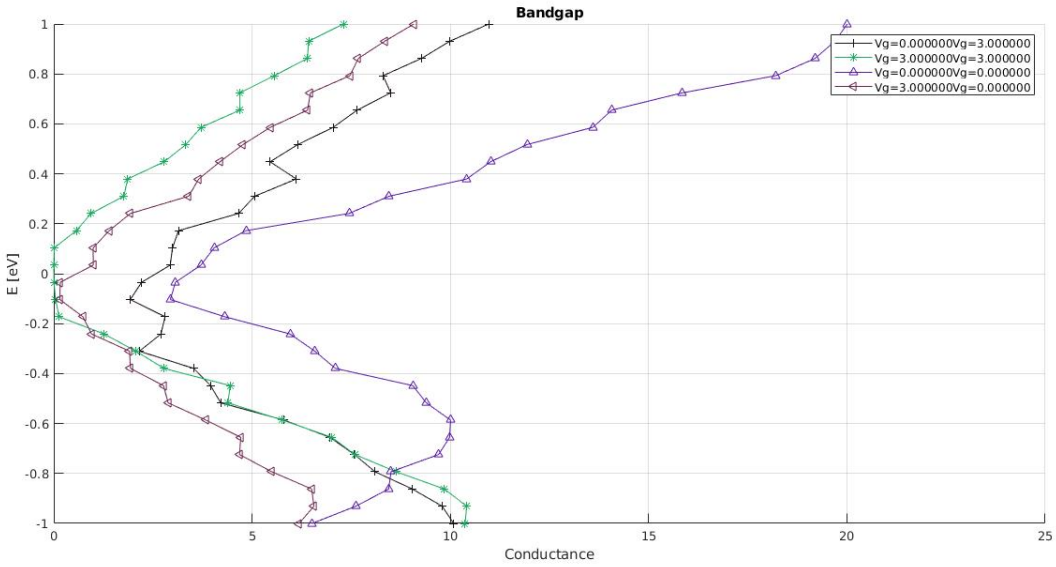


Figure 3.19: Energy level conductance distribution of GNR for structure #4

As mentioned earlier, for complementary logic design the pull up network mimic the behaviour of the desired logic, while the pull down network have the inverse function. Keeping that in mind, the four simulated structures can be used to create different devices. Structure #1 and #2 can be used as an inverter, but switching the way they are connected, the same structures can be used for creating inverter. The same applies for structure #3 and #4, where if #3 is connected as pull up network and #4 as pull down it forms an `OR` gate, while the opposite connection can be used to create `NOR` gate.

### 3.2.2 GNR simulation for 30nm technology

Another simulation of structures is performed for devices that can be realised in 30 nm technology. The simulated butterfly shapes are summarised in table 3.2

Table 3.2: GNR complementary Boolean gates simulation parameters for 30 nm technology

| Structure № | W (nm) | L (nm) | Lc (nm) | Wc (nm) | $L_{edge}$ (nm) | $L_{angle}$ (nm) | Channel Contact (nm) | Drain/Source Contact (nm) |
|---|---|---|---|---|---|---|---|---|
| #1 | 65 | 110 | 30 | 30 | 30 | 10 | 25 | 5 |
| #2 | 82 | 124 | 34 | 30 | 30 | 15 | 30 | 5 |
| #3 | 70 | 240 | 90 | 30 | 65 | 10 | 30 | 5 |
| #4 | 66 | 232 | 90 | 30 | 61 | 10 | 30 | 5 |

The conductance difference for the first two structures of the table is visualised in figure 3.20. For the simulation, the `Vdd` is set to 5V and the gate voltage is changed from zero to $V_{dd}$. Compared to the simulations from the 10 nm that shows the same behaviour, it can be seen that the down network shows higher conductance ratio. Combining structure #1 and #2 as pull up and pull down network they can be used to create inverter logic. Moreover, reversing the connection for both structure they can be used as a buffer.

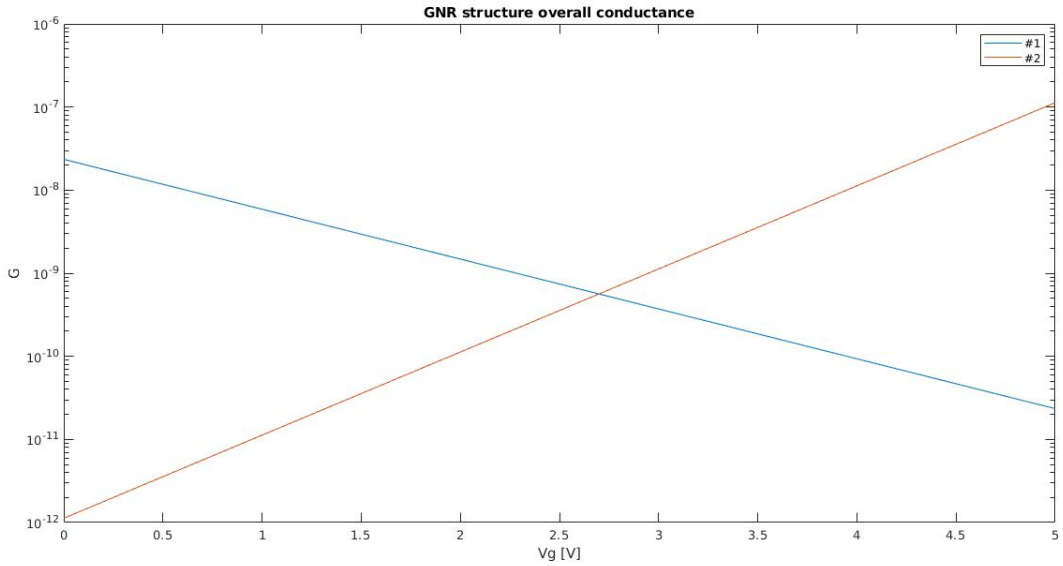


Figure 3.20: Conductance change for different channel voltage levels for structure #1 and #2

The result for structures #3 and #4 from the table that have 30 nm channel width are shown in figure 3.21 and in figure 3.22. The $V_{dd}$ is set to 5V and the gate voltages are changed from zero to 5V. Each logic output from the truth table of the device is simulated individually. For this set of simulations is also observed that the ratio between the ON and OFF state is larger, compared to the simulations performed in 10 nm. By changing the connection of both structures it can be derived either OR or NOR Boolean logic device.

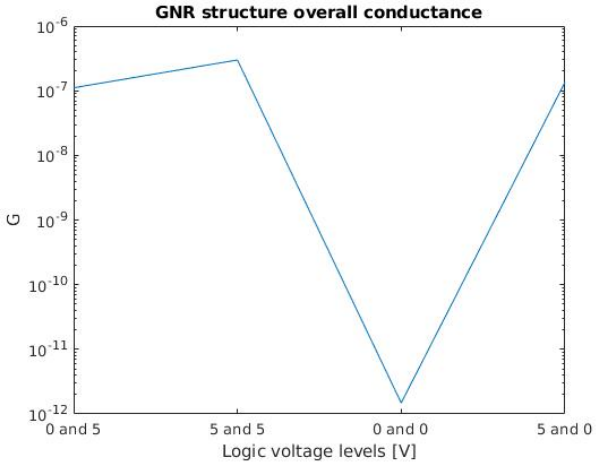


Figure 3.21: Conductance change for different channel voltage levels for structure #3

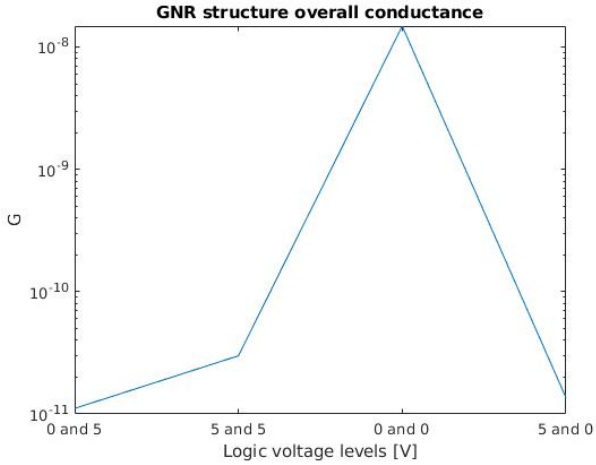


Figure 3.22: Conductance change for different channel voltage levels for structure #4

For all simulations performed in 30 nm technology can be noted that the obtained results are generated by applying higher voltages compared to the 10 nm. This is due to the fact that with 3V and the same dimensions of the structures, the behaviour of the devices was not observed. It should also be considered that the energy levels was reduced to 10 which can lead to an error in the final result. They are reduced, because of the very large number of atoms that slows down the computation of the model. Attempts were made to simulate a structure with the same number of energy levels as in the previous simulation, but for one week of run time it had finished only half of the computation for the first voltage point.

The back-gate voltage ($V_{bg}$) in all simulations was set to 0V, because a larger voltage will decrease the band gap of the graphene. By decreasing the band-gap there will be higher area with a conductance close to zero in the energy band structure from which the ratio between ON and OFF state will degrade.

# References


[1] LCAO BANDSTRUCTURE. "Bandstructure of Graphene and Carbon Nanotubes : An Exercise in Condensed Matter Physics". In: 2000.

[2] C.W.J. Beenakker and H. [van Houten]. "Quantum Transport in Semiconductor Nanostructures". In: *Semiconductor Heterostructures and Nanostructures*. Ed. by Henry Ehrenreich and David Turnbull. Vol. 44. Solid State Physics. Academic Press, 1991, pp. 1–228.

[3] L. Brey and H. A. Fertig. "Electronic states of graphene nanoribbons studied with the Dirac equation". In: *Phys. Rev. B* 73 (23 2006), p. 235411.

[4] A. H. Castro Neto et al. "The electronic properties of graphene". In: *Rev. Mod. Phys.* 81 (1 2009), pp. 109–162.

[5] Supriyo Datta. "Nanoscale device modeling: the Green's function method". In: *Superlattices and Microstructures* 28.4 (2000), pp. 253–278. ISSN: 0749-6036.

[6] Supriyo Datta. *Quantum Transport: Atom to Transistor*. Cambridge University Press, 2005. DOI: 10.1017/CBO9781139164313.

[7] Simon Dubois et al. "Electronic properties and quantum transport in Graphene-based nanostructures". In: *The European Physical Journal B* 72 (Nov. 2009), pp. 1–24. DOI: 10.1140/epjb/e2009-00327-8.

[8] Y. Jiang, N. C. Laurenciu, and S. D. Cotofana. "On Carving Basic Boolean Functions on Graphene Nanoribbons Conduction Maps". In: *2018 IEEE International Symposium on Circuits and Systems (ISCAS)*. 2018, pp. 1–5.

[9] Y. Jiang et al. "Graphene Nanoribbon Based Complementary Logic Gates and Circuits". In: *IEEE Transactions on Nanotechnology* 18 (2019), pp. 287–298.

[10] Yande Jiang, Nicoleta Cucu Laurenciu, and Sorin Cotofana. "Complementary Arranged Graphene Nanoribbon-based Boolean Gates". In: *2018 IEEE/ACM International Symposium on Nanoscale Architectures (NANOARCH)* 18402103 (2018).

[11] T. Kubis et al. "General Retarded Contact Self-energies in and beyond the Non-equilibrium Green's Functions Method". In: *Journal of Physics Conference Series* 696 (Apr. 2016). DOI: 10.1088/1742-6596/696/1/012019.

[12] Edward McCann and Vladimir I. Fal'ko. "Landau-Level Degeneracy and Quantum Hall Effect in a Graphite Bilayer". In: *Phys. Rev. Lett.* 96 (8 2006), p. 086805.

[13] Paul L. McEuen et al. "Disorder, Pseudospins, and Backscattering in Carbon Nanotubes". In: *Physical Review Letters* 83.24 (1999), pp. 5098–5101. ISSN: 1079-7114. DOI: 10.1103/physrevlett.83.5098.

[14] Ioannis Nikiforidis, Ioannis Karafyllidis, and Panagiotis Dimitrakis. "Simulation and parametric analysis of graphene p-n junctions with two rectangular top gates and a single back gate". In: *Journal of Physics D: Applied Physics* 51 (Jan. 2018).

[15] C.N.R. Rao, A. Müller, and A.K. Cheetham. *Nanomaterials Chemistry: Recent Developments and New Directions*. May 2007, pp. 1–403. DOI: 10.1002/9783527611362.

[16] R Saito, G Dresselhaus, and M S Dresselhaus. *Physical Properties of Carbon Nanotubes*. 1998. DOI: 10.1142/p080.

[17] Young-Woo Son, Marvin L. Cohen, and Steven G. Louie. "Energy Gaps in Graphene Nanoribbons". In: *Phys. Rev. Lett.* 97 (21 2006), p. 216803.

[18] P. R. Wallace. "The Band Theory of Graphite". In: *Phys. Rev.* 71 (9 1947), pp. 622–634.

# Chapter 4

# Design and fabrication

The aim of this chapter is to present a detailed explanation of the created designs for the first and second batch of samples. The design has been created using AutoCAD 2018. In addition, the fabrication steps of the samples are described. Electron beam lithography is chosen as a patterning method due to it's advantages over optical lithography as described in the background information. Oxygen plasma was used to etch the exposed areas and remove the unnecessary graphene from the first batch of samples. From the second batch of samples, one of the substrates was etched using oxygen plasma, while the rest of the samples was used to test the etch rates of hydrogen plasma. In Chapter 5 the analysis of the patterned samples will be described.

## 4.1 Design of the butterfly structures used for the first batch of samples

The initial design of the samples is visualised in figure 4.1a. The design of the substrate has contact pads (Au) with dimensions starting from 20x20 $\mu m^2$ up to 200x200 $\mu m^2$. The purpose of these contact pads is to expose the contacts of the created internal structures. The distance between two of the contact pads with dimensions of 200x200 $\mu m^2$ is 100 $\mu$m. Three additional Au pads are placed at two of the sides with dimension of 140x200 $\mu m^2$. The orientation of the chip showed in figure 4.1a is used as a reference to the external company that transferred the graphene grains to the $SiO_2$ samples. The zigzag edges are requested in vertical direction, while the armchair edges are supposed to be located in horizontal direction.

Markers are placed in the inner part of the substrate between the contact pads in form of a matrix. The distance between each of the two markers is 140 $\mu$m. Each marker is created with a different shape that represent a specific spot on the chip. An example of a marker design is shown in figure 4.1b. In total, the matrix formed by the markers contains 14 rows and 14 columns. One element of the matrix will be considered as a `cell`. The Au contact pads and the markers was already placed on the samples beforehand.

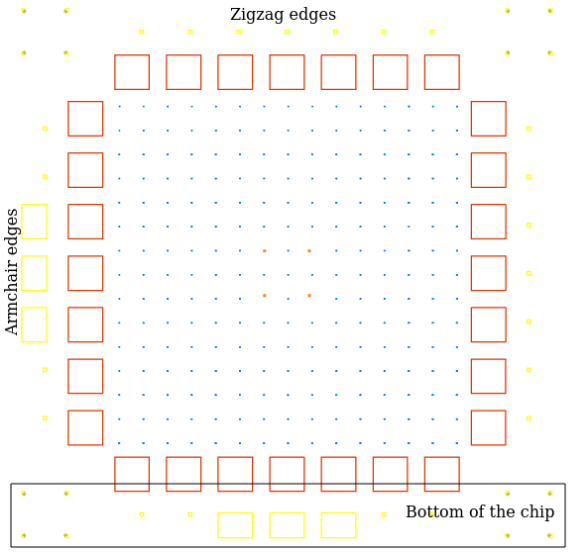


(a) Full overview of the initial design including the location of the Au contacts (red and yellow squares), markers ( the light blue dots) and selection of the chip orientation

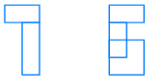

(b) Example of one of the markers. The markers are spread across the internal part of the chip with a distance between each marker of 100 $\mu$m.

Figure 4.1: Initial Autocad design of the substrate

The first 4 rows between the markers of the top part of the chip are used to create the intended design. The full overview of design is visualised in figure 4.2.

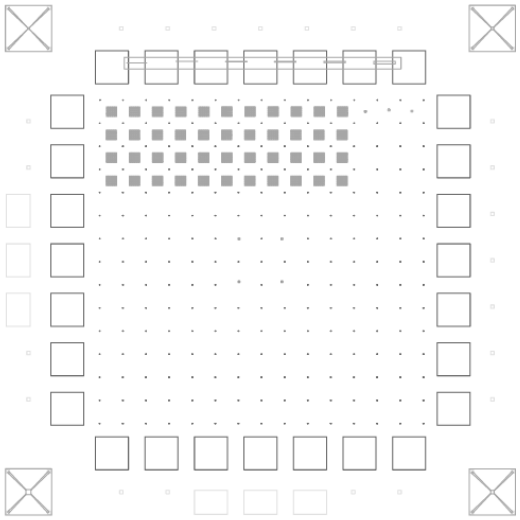

Figure 4.2: Full chip design view of the $Si/SiO_2$ substrate with included connection between the contacts, four probe connection at each edge of the chip and squares at the first 4 rows of the chip.

The design of the butterfly structures are created in a square with dimensions of 10x10 $\mu m^2$. Each cell consists of 25 squares which are visualised in figure 4.3a. The distance between two squares is 3 $\mu$m. This number of squares is chosen for each cell in order to repeat the patterns. For complementary logic gates two structures are used in order to create the pull up and the pull down network. Therefore, each device is created as a pair of two structures with a distance between them of 3 $\mu$m. The small distance between the two patterns in each square is created for easier characterisation of the samples. The position of the butterflies and the

dimensions from the sides of the square are shown in figure 4.3b

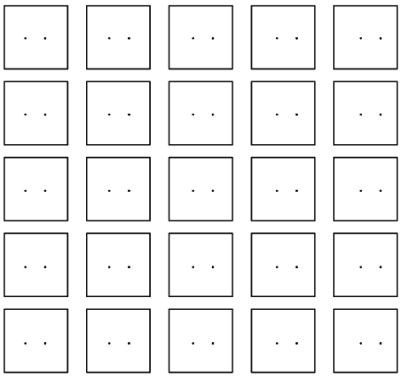

(a) 5x5 matrix of squares that represent one cell from the created grid of the device structures

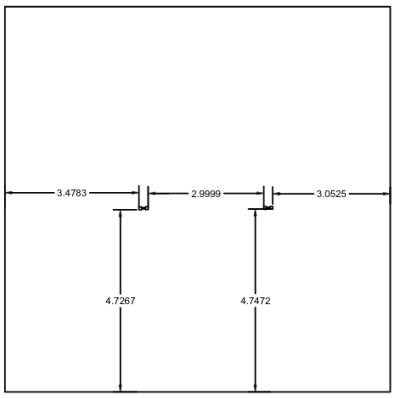


(b) Design of complementary logic gate using two butterfly patterns. The dimensions are present in $\mu$m

Figure 4.3: Square design and position of the butterfly structures

As previously mentioned in section 3.2, by modifying the dimensions of the butterfly patterns, different logic can be obtained. The chosen dimensions of the structures are taken from the simulation results of the butterflies with 30 nm channel width. The designed patterns are shown in figure 4.4a and 4.4b for by changing their connection as pull-up or pull-down network inverter or buffer logic can be obtained as we have observed from the simulation model results in section 3.2.2. Similarly, the created patterns visualised in figure 4.4c and 4.4d can be used to in order to create OR or NOR complementary logic gates. The dimensions of the designed patterns are summarised in table 3.2.

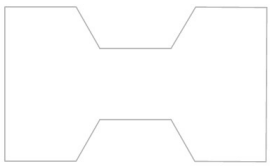

(a) Structure design of a pull up device for inverter gate and pull down device for buffer gate

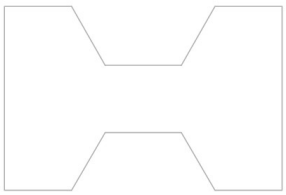

(b) Structure design of a pull down device for inverter gate and pull up device for buffer gate

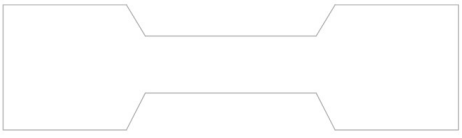

(c) Structure design of a pull up device for OR gate and pull down device for NOR gate

(d) Structure design of a pull down device for OR gate and pull up device for NOR gate

Figure 4.4: Designed butterfly structures that can be used for complementary logic device

In addition to the 30 nm structures, butterflies with larger channel dimensions are included to the design. The butterflies are visualised in figure 4.5 and the dimensions are summarised in table 4.1.

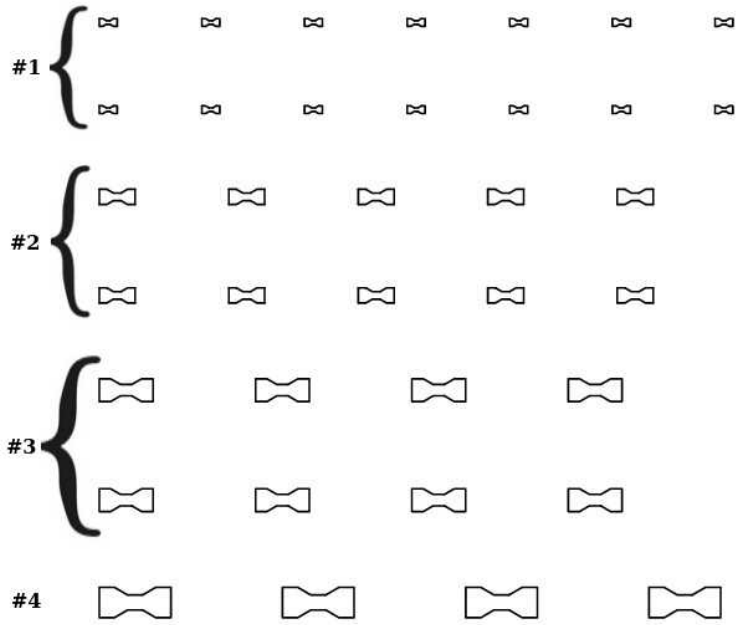


Figure 4.5: Design of additional patterns included to the first batch of substrates with different channel dimensions from 50 nm to 200 nm

Table 4.1: Dimensions of the additional patterns included to the first batch of substrates.

| Structure № | W (nm) | L (nm) | Lc (nm) | Wc (nm) | $L_{angle}$ (°) |
|---|---|---|---|---|---|
| #1 | 100 | 250 | 50 | 50 | 30 |
| #2 | 200 | 500 | 100 | 100 | 30 |
| #3 | 300 | 750 | 150 | 150 | 30 |
| #4 | 400 | 1000 | 200 | 200 | 30 |

The layout and the position of the structures on the chip is presented in figure 4.6. The design of the butterfly patterns are created horizontally in the same direction as the requested edge orientation in order to match the zigzag edges with the direction of the current flowing through the butterfly. This is necessary to obtain the desired electronic properties. In addition, since the graphene is poly-crystalline, the structures are rotated with $\pm$ 1° up to 5° compared to the initial butterfly design. In case that the channel edges differs from zigzag, the electronic properties of the device will be degraded and it is even possible that it does not show the expected behaviour. Thus, the patterns are rotated in order to obtain a butterfly structures that are very closely to the preferred zigzag edge orientation.

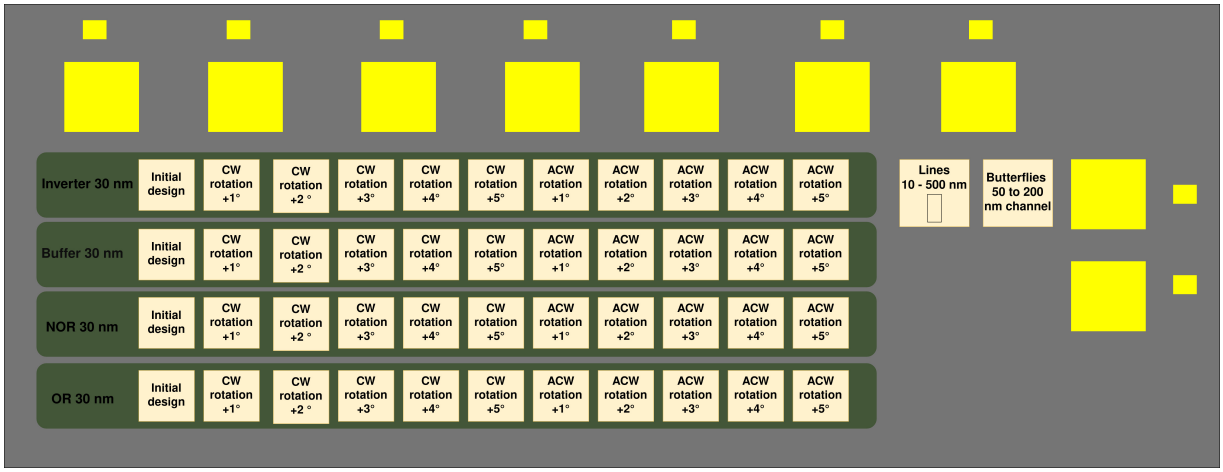


Figure 4.6: Overview of different pattern included to the design and their position on the substrate in respect with the surrounding contact pads at the top right part of the substrate. Acronyms are used in the figure for clockwise (CW) and anti-clockwise (ACW).

Finally, as a requirement for placing contacts on the created structures from this design is that the distance between two patterns should be at least 100 $\mu$m. This condition can be satisfied in case that, the pattern for the pull up network is used from the first row (INVERTER) or third row (NOR gate) and the pattern for the pull down network is connected from the second row (INVERTER) or fourth row (NOR gate) respectively.

## 4.2 Design of additional structures used for the second batch of samples

Another design was made which was used for second batch of fabrication. The design focuses on structures with micron meter sizes. The created patterns in this design are used to study and compare the edge termination of oxygen and hydrogen plasma etching. As in the previous design, the intended patterns was included at the top part of the substrate as visualised in figure 4.7.

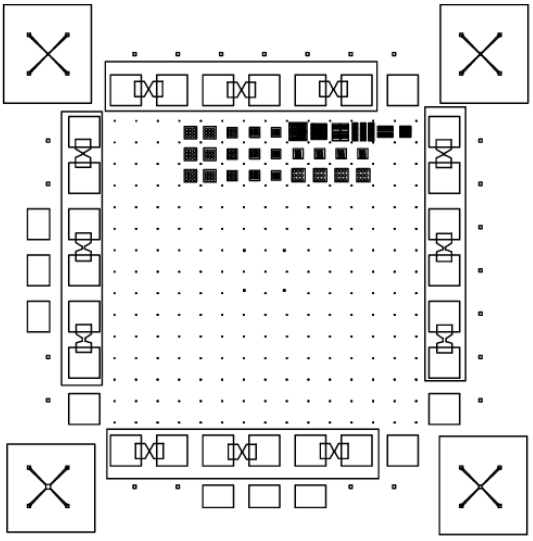

Figure 4.7: Full overview of the substrate and the square position for the second created design

Between the 200x200 $\mu$m Au pads butterflies with channel dimensions of 1, 3, 7, 15 and 20 $\mu$m are included in order to perform two contact probe electrical measurements.

The design of the patterns for the second batch is shown in figure 4.7. The created squares, pentagons and hexagons are rotated with $\pm$ 1° step up to $\pm$ 4° in respect to the initial structure design. The reason behind is that if the all structures are patterned within the same grain, the rotation would help to identify the angle at which the edge orientation is equal to the preferred one. Butterfly structures with channel width and length of 200 nm are included in order to compare the result with the scans performed from the first batch. In addition, butterflies with slope of 60° are included for the butterflies with minimal feature size of 200 nm.

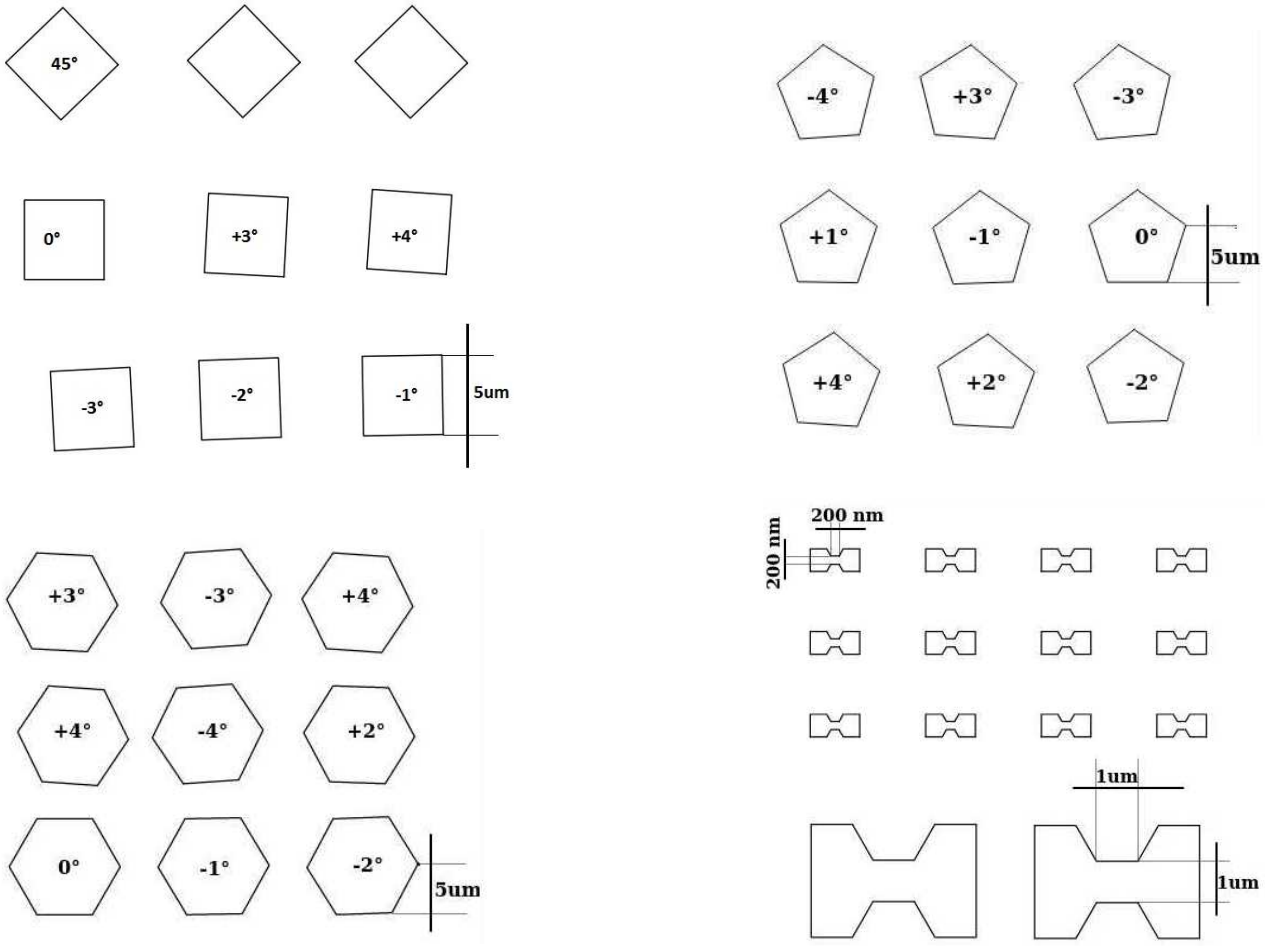


Figure 4.8: Design patterns included for the second fabrication batch. For each design of the squares, pentagons and hexagons are rotated with ±1 °between each pattern up to ±4 °. Each side of the presented structures is 5 $\mu$m, except the butterflies for which the channel dimensions are 200 nm or 1 $\mu$m.

Figure 4.9 presents the layout of the top part of the substrate and the position of the included patterns. The squares, pentagons and hexagons patterns are duplicated across the top part of the substrate with a change in their dimensions from 1 $\mu$m up to 10 $\mu$m.

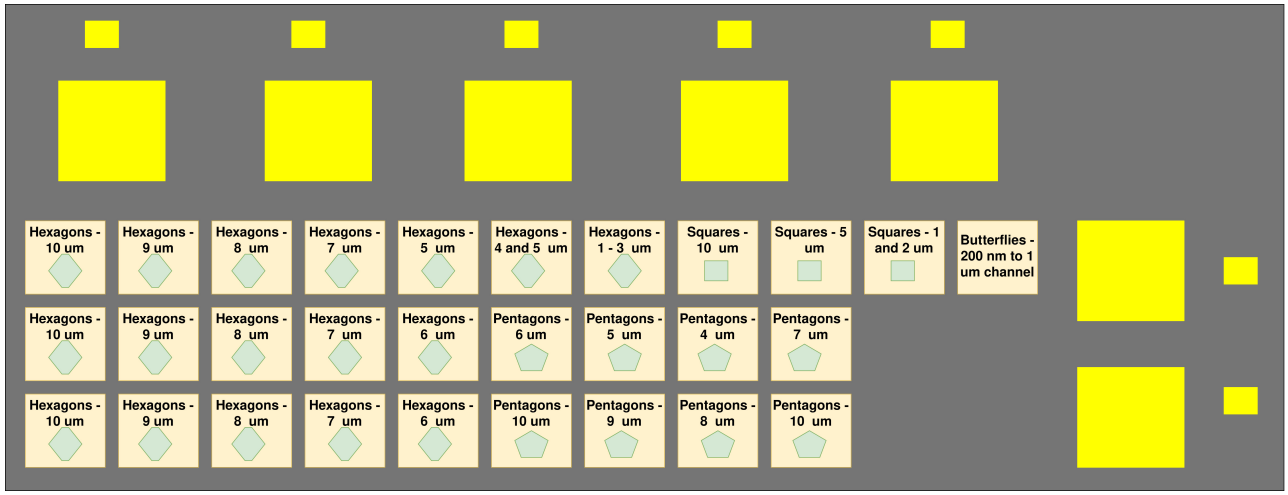


Figure 4.9: Overview of different pattern included to the design and their position on the substrate in respect with the surrounding contact pads at the top right part of the substrate

### 4.2.1 Patterns included in both designs

In both designs, a four contact connection between the 20x20 $\mu$m yellow contacts that are located at the edges of the substrate is included. The square created in the middle between each edge is 10 $\mu$m. The connection is visualised in figure 4.10. The blue square on one of the edges of the square shows the area used to perform Raman mapping (figure 5.13).

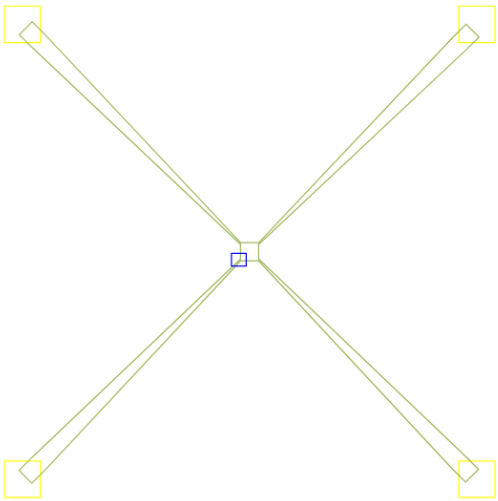

Figure 4.10: 20x20 *um* Au contact pads (yellow) connected to square. The light blue square at the bottom left edge is used to visualise the area on which Raman measurements are taken.

## 4.3 Transferring mono layer graphene to the desired substrate

For this project CVD growth graphene is used, which was provided from a commercial supplier. After growing mono layer graphene, it is necessary to be transferred from the growth substrate to the desired substrate for further patterning without damaging the honeycomb graphene structure or the substrate itself. The chosen substrate for transferring is a $SiO_2/Si$ with active area of 3x3 mm. The thickness of the $SiO_2$ is 285 nm. The transfer process of the mono layer graphene was performed by ANL at TU Delft. Unfortunately, the process is

a company secret and details regarding the method used for transferring or the quality of the grains was not provided.

## 4.4 Fabrication steps of the design

The fabrication of the design on the substrate consists of five steps which were all carried in the clean room of Kavli Institute of Nanoscience. The fabrication of the chips was conducted entirely by a PhD student from Applied Physics department.

First, the substrate was spin coated with a positive resist (PMMA). Another option for spin coating is negative resist which is usually HSQ. However, previous experiments shows that using negative resist the created patterns have worse results compared to the ones with positive resist. The type of the positive resist used in this project is PMMA 950k A3, spin coated on the substrate at 4000 rpm. The thickness of the resist is approximately 120 nm. Secondly, the 10x10 micron squares were patterned. This was used as initial patterning for rough removal of the rest of the area which does not include any nano ribbon structures.

Third, the nanoribbons were patterned using Electron Beam Pattern Generator operating at 100kV which provides approximately the same energy per electron (100 keV). The wavelength of the electrons for this energy is 0.37 nm. The electron beam size was set to 5 nm, but the beam size which interacts with the substrate is estimated to vary from 3.3 up to 16.8 nm. The dose setting is an important parameter which determines the number of electrons that are delivered to the sample. The higher the dose is set, more electrons are delivered, while low doses cause low amount of electrons to be delivered. The dose setting varies from the type of the resist used on the sample and usually the optimal point is determined experimentally. For positive resist, the dose was set to 2000 $\frac{uC}{cm^2}$ with enabled proximity error correction. Next, the exposed areas are developed using 1:3 ratio of Methyl isobutyl ketone (MIBK) and Isopropyl alcohol (IPA) for 30 seconds.

Finally, the exposed parts were etched with pure oxygen plasma ($O_2$) for 30 seconds using Sentech Etchlab 300 'F2'. The settings used during the etch process were 100V constant bias voltage and constant pressure of 20 µbars. The measured power during etching was 21W. This step was performed only on the first batch of samples and on one of the samples from the samples of the second batch.

To verify the correctness of the settings from each step, the design was exposed to a blank $SiO_2/Si$ sample and SEM characterisation was performed after the fabrication. The result of the analysis is discussed in the next section.

### 4.4.1 Dose test on silicon dioxide/Silicon substrate

The dose test on a blank substrate is used to verify the correctness of the settings used for each of the fabrication steps. Due to the mono atomic thinness, low amount of charge carriers and high conductivity of mono layer graphene, the patterning of graphene versus no-graphene substrate can be assumed that has very little difference. After exposing the design, developing and etching with oxygen plasma a characterisation of the resist patterns was performed using scanning electron microscopy (SEM). The characterisation with the SEM was used in order to evaluate the impact of the pattern sizes. In figure 4.11 are visualised the patterned initial 10x10 micron squares and butterfly patterns with smallest dimensions for the channel from 30 nm (figure 4.11b) to 200 nm (figure 4.11c). The butterfly slope for the larger patterns above 50 nm was set to 30 degrees in order to test different angles than the one used in the 30 nm structures for which 60 degree slopes are set. The requested 30 nm butterflies are visualised in figure 4.11b.

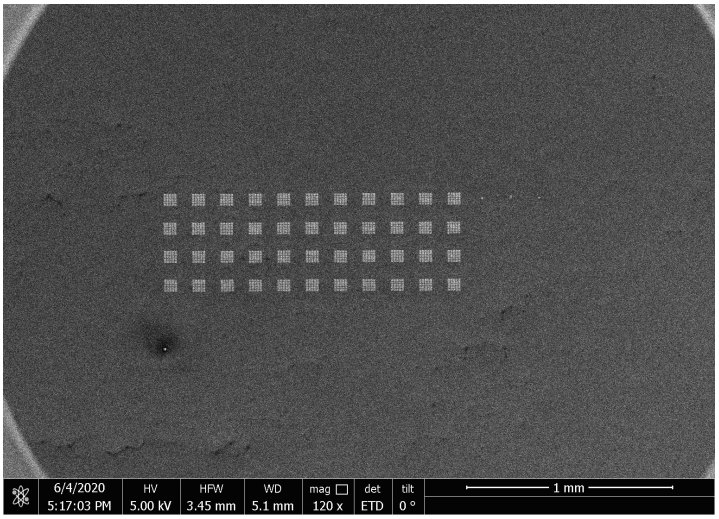


(a) Patterned 10x10 micron squares on the substrate

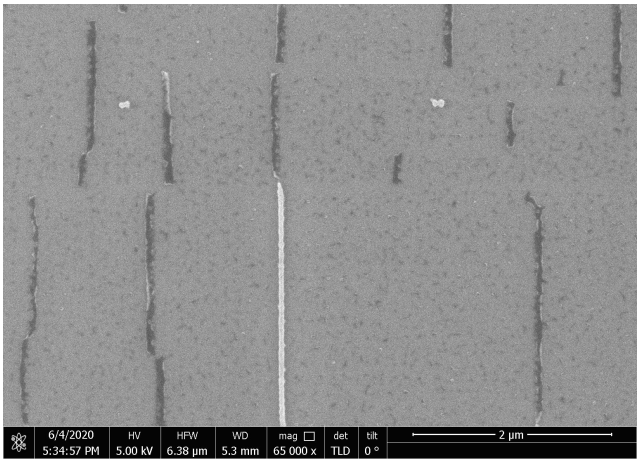


(b) Patterned graphene nano ribbon butterflies with channel length of 30 nm

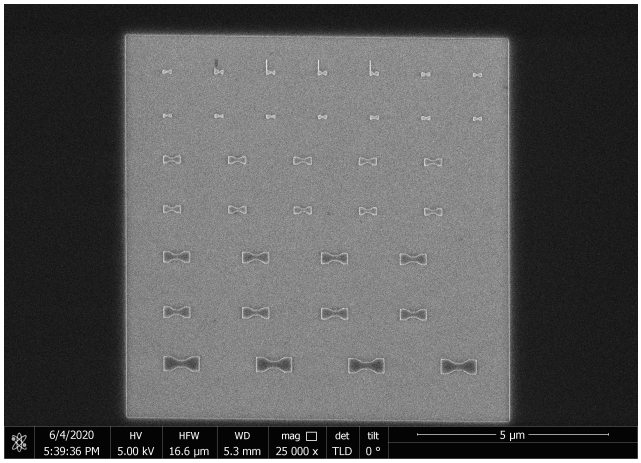


(c) Patterned butterflies with channel length of 50 to 200 nm

Figure 4.11: SEM images taken from the blank $SiO_2/Si$ of pattern design model

High resolution images were taken on individual structures. The characterisation of different butterfly patterns are visualised in figure 4.12 and the dimensions are summarised in table 4.2.

Table 4.2: Dimension difference between the intended and fabricated patterns on a blank substrate

| Design № | Design Width nm | Design Length nm | Real Width nm | Real Length nm |
|---|---|---|---|---|
| #1 | 110 | 30.00 | 106.21 | 22.84 |
| #2 | 110 | 30.00 | 104.60 | 36.10 |
| #3 | 150 | 50.00 | 199.84 | 40.97 |
| #4 | 300 | 100.00 | 315.52 | 78.24 |

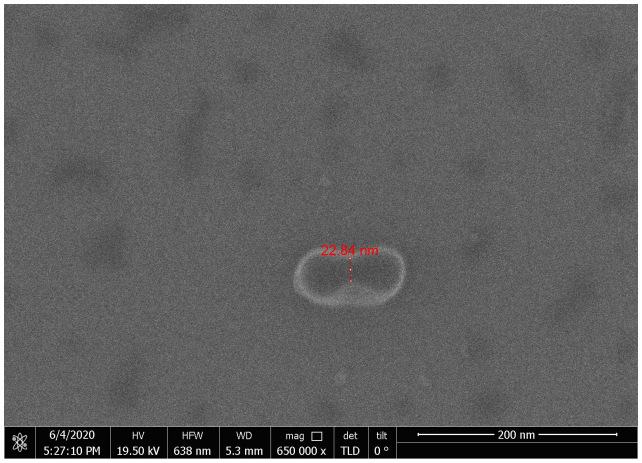


(a) Butterfly pattern #1

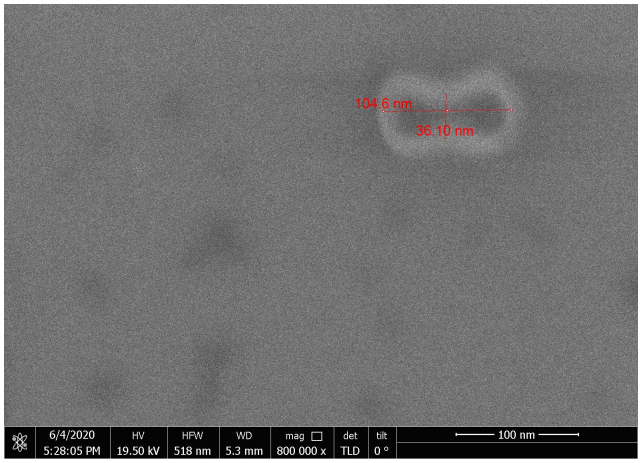


(b) Butterfly pattern #2

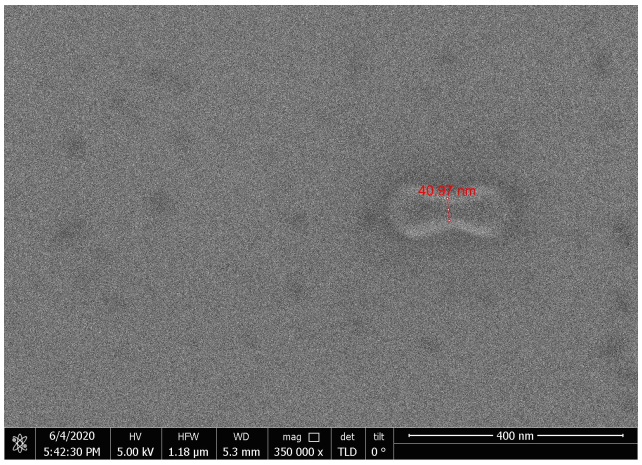


(c) Butterfly pattern #3

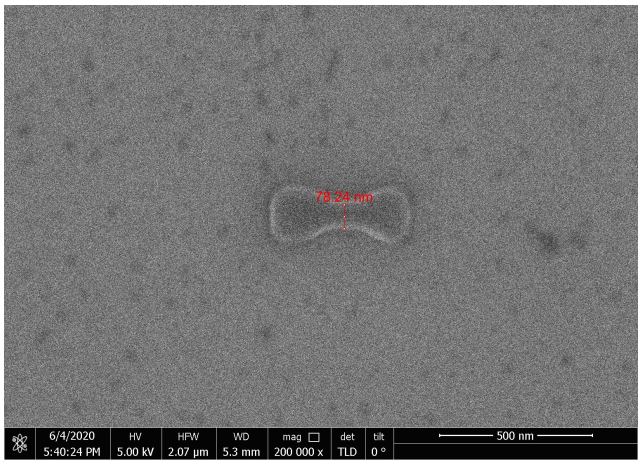


(d) Butterfly pattern #4

Figure 4.12: High resolution SEM images taken from the blank $SiO_2/Si$ of pattern design model

Overall, using the settings for each fabrication step described in section 4.4 and the performed characterisation using SEM, shows promising results for patterning structures below 50 nm. Therefore, the same settings were used for patterning the mono layer graphene substrate with the design of the first batch of samples. The only difference in the settings for the graphene sample was that the developing time was increased to 60 seconds, due to observed errors from the analysis of the blank substrate. For the second batch the dose test was not performed as the patterns are created in micron meter size and the beam exposure for this type of patterns is quite robust. In addition, one sample from the second batch was etched using oxygen plasma, while the rest of the samples was only patterned and developed in order to test the etching rate and quality of hydrogen plasma. The performed experiments of hydrogen plasma etching are described in section 5.5.

# Chapter 5

# Characterisation of the samples

The aim of this chapter is to present a detailed explanation of the obtained results from the performed experiments. First, analysis of the samples after the transfer process using Raman spectroscopy is described. Second, the patterned samples form the first batch that are etched with oxygen plasma are analysed using AFM and Raman spectroscopy. Third, a cleaning procedure is described and applied on the samples. This is followed by further inspection using AFM and Raman. Next, characterisation using AFM and Raman spectroscopy is performed on the second batch of samples. Furthermore, test of etching with hydrogen plasma on exfoliated is described and applied to the rest of the not etched samples from the second batch. The characterisation of the hydrogen plasma etched sample is performed in the similar way to the other samples using AFM and Raman. Finally, electrical measurements are taken from one of the oxygen plasma etched sample from which the transport characteristics and carrier mobility are obtained.

## 5.1 Analysis of the graphene after transferring on the substrates

The first step, before the fabrication process was to evaluate the graphene after the transfer process and to get an idea of the potential damages introduced to it. For this purpose, Raman spectroscopy was performed on different places on two of the transferred substrates. As it was mentioned in section 2.4.1, Raman spectroscopy is a powerful method for analysing graphene, which can be used not only to get information about whether mono- or multi-layer graphene is transferred, but also by looking at the three main graphene peaks (D, G, 2D) the physical quantities of the graphene can be determined. This quantities include, stress/strains, damages in the $sp^2$ bonded carbon structure and defects introduced from contamination of the sample.

Two different areas were selected at which later on the nano-ribbon structures will be patterned. The dimensions of the selected area for the performed experiments are 11x11 $\mu m^2$ for the first substrate and 15x15 $\mu m^2$ for the second one. In addition, experiment for determining the edge termination of the graphene grains was performed on the second substrate. The result of this experiment is described in Appendix B.

For every Raman measurement described in the report the scan is performed using raster method. The raster method starts from the first row of the selected area and performs measurements until the end of it. Once the row is complete, it moves to the next row and the scan is performed again until the last cell of the row. This process is repeat until all rows are scanned. The Raman measurements are taken on Renishaw Invia Reflex Raman Spectroscopy using green laser with 514 nm wavelength. In addition, the gathered data from all Raman experiments is fitted using Lorenzian function. The D and 2D peak are fitted with respect to the G peak.

### 5.1.1 Raman spectroscopy measurements of 11 x 11 micron area with 1 micron step size

The Raman maps described in this section are created using fourth polynomial fitting curve, as it was observed that first polynomial fitting is not able to accurately detect the peak position, when tilt in the signal is present. The analysis from the first polynomial fitting is described in Appendix A.

The generated graphs using the fourth polynomial fitting curve are showed in figure 5.1. It can be seen from figure 5.1a that the $I_{D/G}$ ratio for most of the scanned area is in the range of 0.1 to 0.15. A small area of the substrate is observed to have higher ratio up to 0.25, which suggests that this area of the chip is highly defective. From the spectral width of the 2D band a raise to 53 $cm^{-1}$ is observed in the same area that shows high defects, which could suggest a locally formed bi-layer graphene. Nevertheless, $I_{2D/G}$ ratio as visualised in figure 5.1b for the defective area does not suggest values that can be related to bi-layer graphene. Bi-layer graphene is expected to have value $I_{2D/G}$ ratio lower than the one measured for mono layer graphene, in the range of 0.6 to 1. Instead, a raise of the ratio to approximately 4 is observed that could mean that graphene is highly strained. In addition from the spectral width of the G band showed in figure 5.1d, can be seen that the distribution is almost homogeneous around 13,5 $cm^{-1}$, whit exception of small area of 6x2 $\mu$m that shows a raise up to 19 $cm^{-1}$. This could suggest that in-homogeneous doping occurs. At approximately the same area, the width of the D band also shows a raise between 15 and 18 $cm^{-1}$, which could be related to the wider G peak and support that graphene is either doped or stressed as mentioned in the theoretical survey for the graphene peaks in section 2.4.1. The most likely reason from both is that the graphene is stressed.

From the analysis of 11x11 $\mu m^2$ of the substrate, it is observed that, disorders to the graphene are packed into blocks closed to each other. This could suggest that defects are not randomly distributed across the chip, but rather locally to a specific areas of the chip.

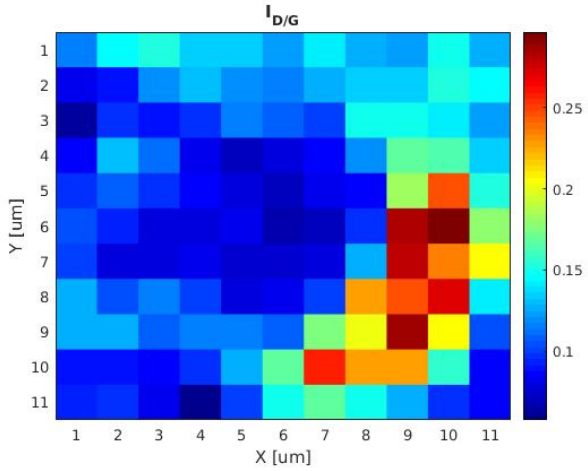


(a) Ratio intensity map for the "D" and "G" peak ratio

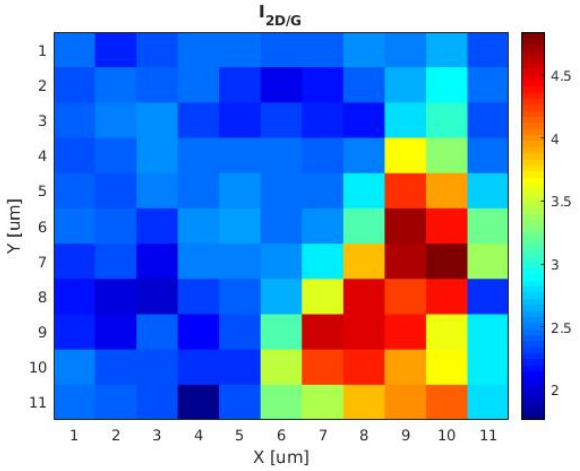


(b) Ratio intensity map for the "2D" and "G" peak ratio

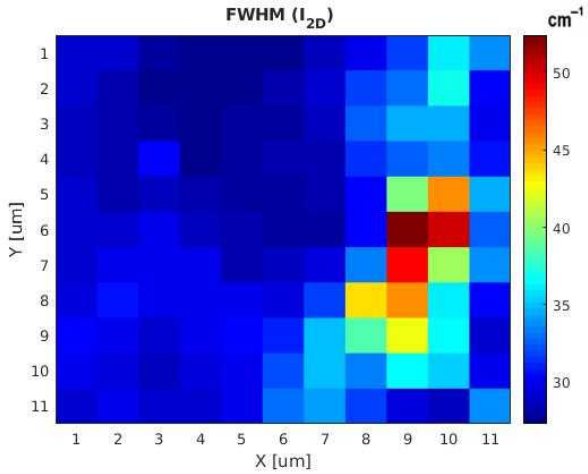


(c) Raman map for FWHM of the "2D" peak

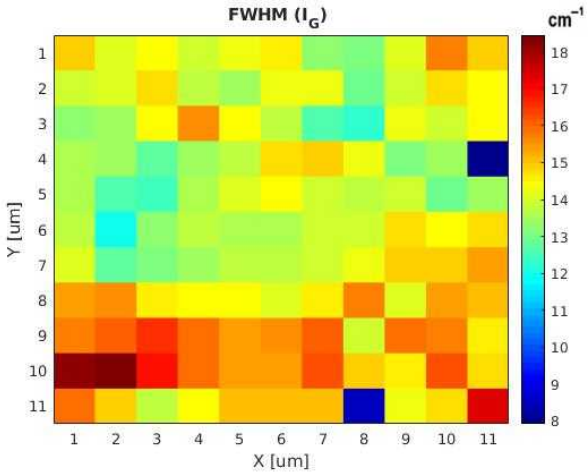


(d) Raman map for FWHM of the "G" peak

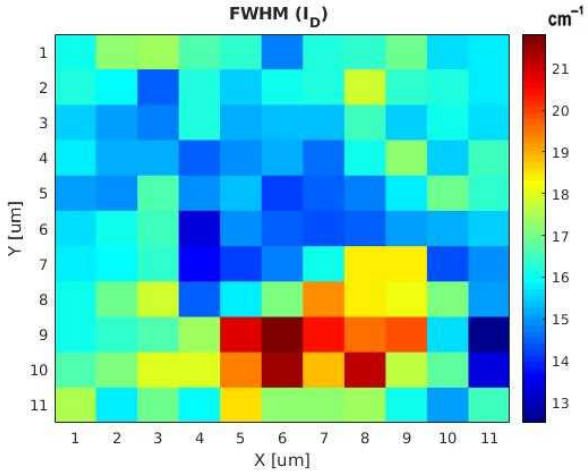


(e) Raman map for FWHM of the "D" peak

Figure 5.1: Raman intensity maps using of mono layer graphene and their ratios respectively using fourth polynomial curve fitting. The wavelength of the Raman green laser is 514 nm, with spatial resolution of 1 $\mu$m. The scanned area is 11x11 $\mu m^2$ with a step size between each measurement of 1 $\mu$m.

### 5.1.2 Raman spectroscopy measurements of 15 x 15 micron area with 1 micron step size

Another experiment is performed on a different area on the same substrate. The selected region for the measurements was set to 15x15 micron with a step size between each measurement of 1 $\mu$m. The $I_{D/G}$ ratio is visualised in figure 5.2a. Compared to the previous experiment, the analysis of the selected substrate area shows more points for which the $I_{D/G}$ is higher than the set threshold for mono layer graphene. The introduced defects can be related to a group of blocks which are close to each other and they are not randomly distributed as observed from the previous experiment. The $I_{2D/G}$ ratio is visualised in figure 5.2b. For the measurement of the selected area, almost all blocks shows ratios in the range of 1,6 to 1,9. A lower ratio is observed only in a few randomly distributed blocks, which could suggest that at this spots graphene is weakly interacting with the substrate. The FWHM of the 2D peak is visualised in figure 5.2c. The analysis shows that all of the measurements are within the range of 27.5 $\pm$ 3.8 $cm^{-1}$ except one which is most likely caused due strains in the graphene.

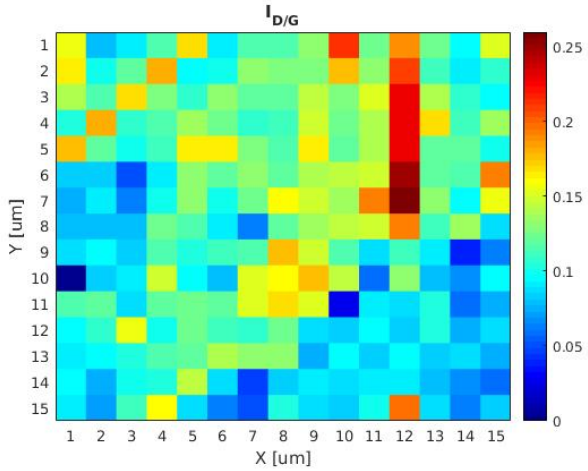


(a) Ratio intensity map for the "D" and "G" peak ratio

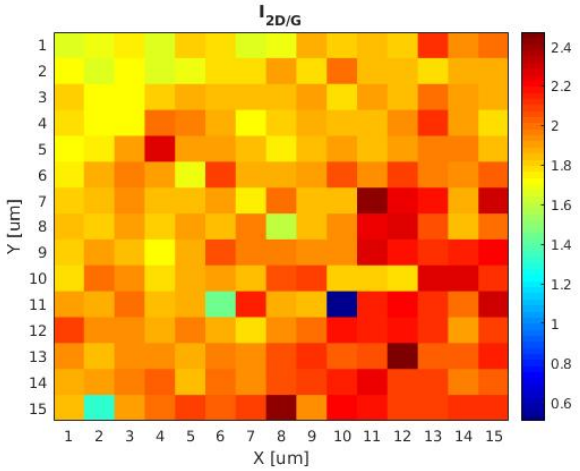


(b) Ratio intensity map for the "2D" and "G" peak ratio

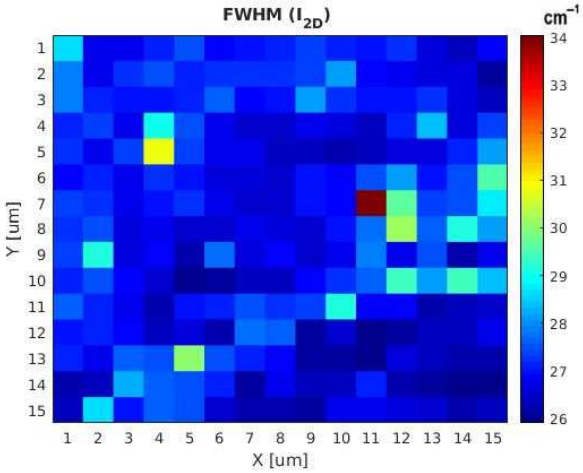


(c) Raman map for FWHM of the "2D" peak

Figure 5.2: Raman intensity maps of mono layer graphene bands and their ratios respectively. The wavelength of the Raman green laser is 514 nm, with spatial resolution of 1 $\mu$m. The scanned area is 15x15 $\mu$m$^2$ with a step size between each measurement of 1 $\mu$m.

From the performed Raman mappings on two different substrates with areas of 11x11 $\mu$m$^2$ and 15x15 $\mu$m$^2$ it can be derived that defects are indeed introduced on the graphene either from distortions of the lattice or left

contamination from the transfer resist.

## 5.2 Analysis of the oxygen plasma etched from the first batch of samples before removing the remaining resits

This section shows the result from the characterisation of the substrate after the fabrication process was complete and before removing the remaining resist of the substrate. This step is performed in order to understand how the patterns are formed and to get an idea for the dimensions of the structures.

The images are taken using a scanning frequency range of 0.20 to 0.80 Hz, where the lower frequency allows for higher resolution images. The resolution also depends from the number of steps per line, which for the set of experiments varies from 128 to 512 pixels. The force at which the tip interacts with the sample is determined by the set point and the feedback gain. Usually the set point is 75 % of the resonance peak, while the feedback gain can varies between 0.1 to 0.5. By lowering the set point the tip interacts with the substrate with more applied force, which might generate noise in the retrieved data. On the other hand, higher feedback gain results in a faster recovery of the force after a step has been encountered, which can also contribute to unwanted features in the image. Therefore, an optimal parameter between the set point and the feedback gain needs to be found in order to obtain a good quality image.

The typical signal when the tip is interacting with the substrate should look as shown in figure 5.3. When the feedback is switching on, the tip should drop down to the substrate and generate a single peak of attractive force. This peak is considered as a mode where the tip is in contact with the surface. After the occurring of the peak the signal should normalise to the level of the resonance set point and remain without noise. The level of the peak value is determined by the feedback force set point. [1]

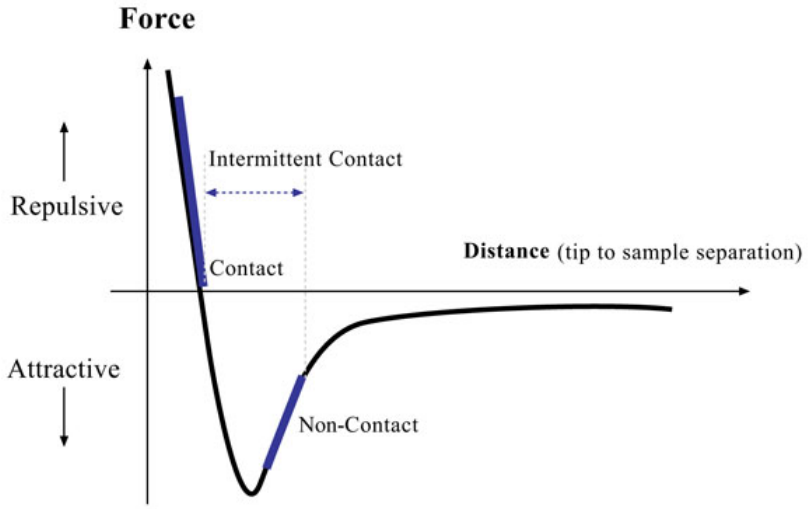


Figure 5.3: Typical AFM tip interaction with the substrate surface (adapted from [1])

As the thickness of the resist is expected to be approximately 120 nm, the free resonance peak value is set to be between 16 to 17 nA, the feedback gain is changed during run-time from 0.1 to 0.3 and the set point of the resonance was changed from 10 to 13.5 nA, based on the scanned surface, the chosen frequency and the number of steps of each scanned line in the image.

In figure 5.4 are visualised the patterns of the butterflies with the smallest intended dimension of 30 nm. Unfortunately from the analysis it can be seen that the intended ribbons for the Buffer (5.4b) and Inverter (5.4a)

with a channel width and length equal to 30 nm does not show a formation of a butterfly and the formed pattern looks like a blob. On the other hand, the structures of the NOR (5.4c) and OR (5.4d) gates, shows a formation of two blobs with a spacing between them, which from the taken AFM images appear to have no resist left and it is likely that the graphene is etched away. For the 50 nm structures visualised in figure 5.4e and 5.4f is visible that the slope to the channel is formed only at one of the sides of the butterfly.

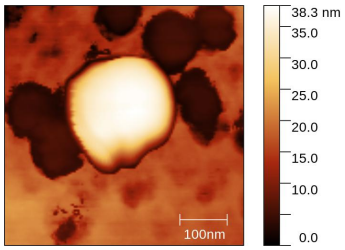


(a) Resist formation of one of the Inverter structures

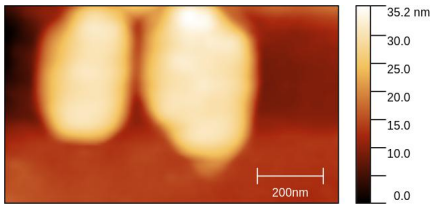


(b) Resist formation of one of the Buffer structures

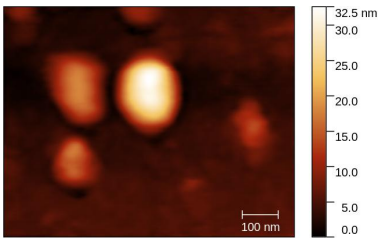


(c) Resist formation of one of the NOR structures

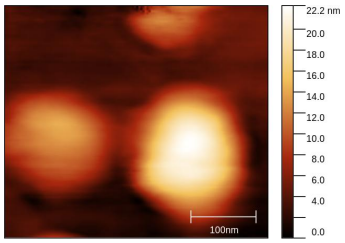


(d) Resist formation of one of the OR structures

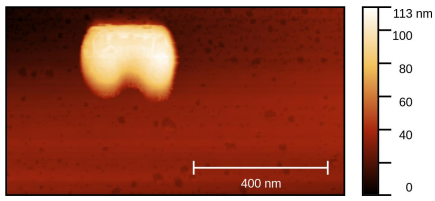


(e) Resist formation of one of the 50 nm patterns

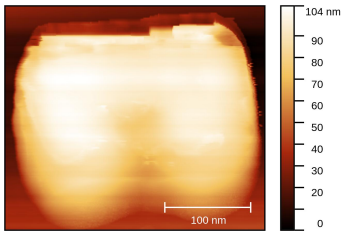


(f) Resist formation of one of the 50 nm patterns

Figure 5.4: AFM images of butterfly ribbons with smallest intended dimension of 30 nm. The tip used for this set of scan is 10 nm golden tip (NSG10)

The butterflies that were created in the design with smallest dimension of 100 nm have visible formation on the substrate after the fabrication process. The AFM images of each butterfly are visualised in figure 5.5. The dimensions of the butterflies were taken by performing profile measurements using Gwyddion software and the results are summarised in table 5.1.

It can be seen that all of the fabricated butterflies are much bigger than the ones intended on the first place with a dimension error varying from 5 % for the 200 nm patterns to up to 40 % for the intended 150 nm patterns and below. The angle variation also differs for each of the butterfly slopes from 30 to 48°. From the analysis of the data it is visible that the angle error decreases when the size of the butterfly increase. The AFM images of the structures, suggest that the exposure is not uniform for the patterns with same dimensions for butterflies below 150 nm channel.

Table 5.1: Dimension difference between the intended and fabricated butterflies

| Design № | Design Width ($W_{LS}$) nm | Design Width ($W_c$) nm | Design Width ($W_{RS}$) nm | Design angle (°) | Real Width ($W_{LS}$) nm | Real Width ($W_c$) nm | Real Width ($W_{RS}$) nm | Real angle (° ) |
|---|---|---|---|---|---|---|---|---|
| #1 | 250 | 100 | 250 | 30 | 365 | 250 | 351 | 30-48 |
| #2 | 300 | 150 | 300 | 30 | 324 | 281 | 315 | 31-39 |
| #3 | 300 | 150 | 300 | 30 | 451 | 400 | 444 | 32-43 |
| #4 | 400 | 200 | 400 | 30 | 435 | 268 | 437 | 30-36 |

Note: $W_{LS}$ represent the left side of the butterfly, $W_{RS}$ - the right side of the butterfly and $W_c$ is the channel. All dimension notations can be seen in figure 3.13.

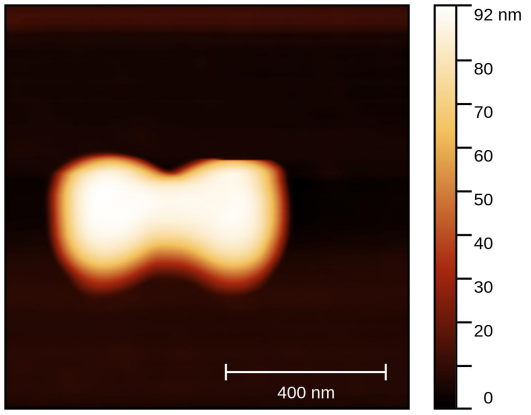


(a) Resist formation of one of the 100 nm butterfly patterns (design #1)

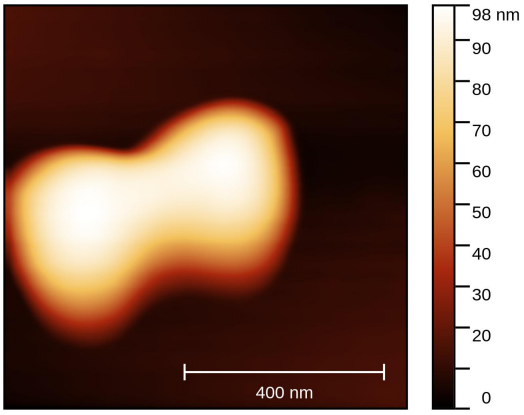


(b) Resist formation of one of the 150 nm butterfly patterns (design #2)

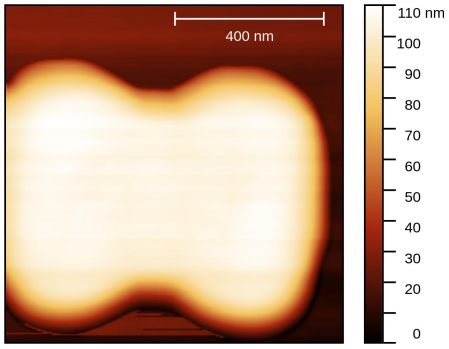


(c) Resist formation of one of the 150 nm butterfly patterns (design #3)

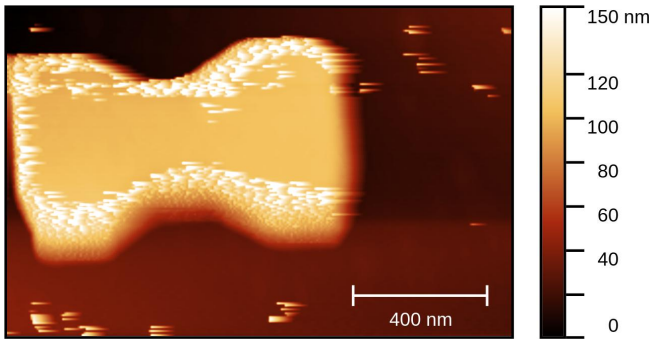


(d) Resist formation of one of the 200 nm butterfly patterns (design #4)

Figure 5.5: AFM images of the butterfly ribbons with intended channel dimension from 100 to 200 nm. The tip used for this set of scan is 10 nm golden tip (NSG10).

The measured dimensions of the butterfly structures is larger than the one intended in the design by up to 50 % difference. Dimension differences can be caused either from the tip which gets contaminated when interacting with the PMMA resist or from the tip shape and its interaction with the much higher thickness patterns. It was experimentally observed that a "shadow" effect occurs around the pattern due to interactions between the edges of the pyramidal, quadrilateral or tetrahedral tip with the side walls of the pattern. [3]. Nevertheless, the shape of the tip does not affect the height profile of the patterns. Their result suggest that only sharp tips with high aspect ratio, large titled angles and excellent circular symmetry tips such as CNT tips or whisker tips shows artifact-free topography. Diamond whisker tips were available with a very sharp tip of 1 to 3 nm, but due to the high thickness variation between the patterns and the sample, they were not tested.

Analysis on one of the butterflies with intended channel of 100 nm is performed, by changing the plot visualisation to zones. The obtained images are visualised in figure 5.6. It can be seen that that most likely the "shadow" effect is in place around the butterfly where the thickness is gradually decreasing. The highest thickness area between 90 and 98 nm is probably the real dimension of the patterned butterfly, which shows a channel length of 106 nm and width of 98 nm.

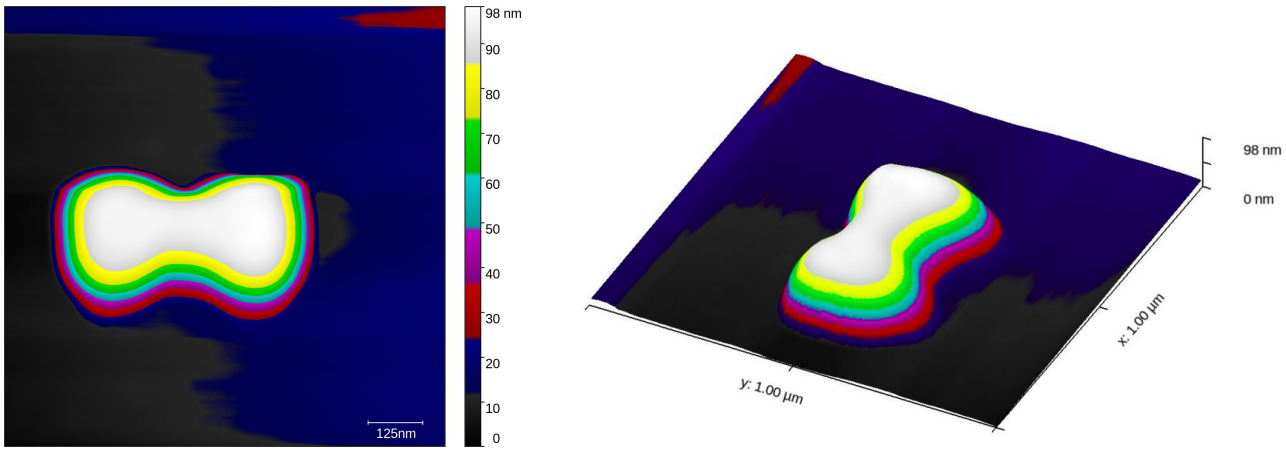


Figure 5.6: Analysis of the tip convolution for butterfly (#1) pattern with 100 nm intended channel by design.

In order to obtain more accurate dimensions of the patterned butterflies, a further analysis after cleaning the sample from the remaining resist is required with a not contaminated tip and smaller tip size. Raman maps are taken on the butterflies with channel dimensions of 50 nm to 200 nm and the results are described in appendix C.

## 5.3 Analysis of the oxygen plasma etched from the first batch of samples after cleaning the substrate

To remove the remaining resist the sample was left to soak in acetone, followed by rinse with IPA for 1 minute. The IPA is used to remove the left residues from the acetone. The first attempt to clean the sample was made for 10 minutes in acetone. After that, AFM images (figure 5.7a and 5.7b) were taken on some of the patterns to evaluate the cleanliness of the sample. From the images it is observed that the sample was still quite dirty and residues from the acetone and PMMA are still in place around and on the structures. Therefore, the sample was left in acetone for 1 hour and AFM scans was performed again (figure 5.7c and 5.7d). In this set of images can be seen that the sample looks cleaner in comparison to the first scan, but still there are left PMMA residues on top of the graphene patterns and possible dust particles or visualised residues due to contamination of the tip. Thus, the sample was soaked in acetone for 15 hours and the tip was replaced for the next AFM images. Raman maps are taken on the same area as before cleaning the sample and the results are summarised in appendix D.

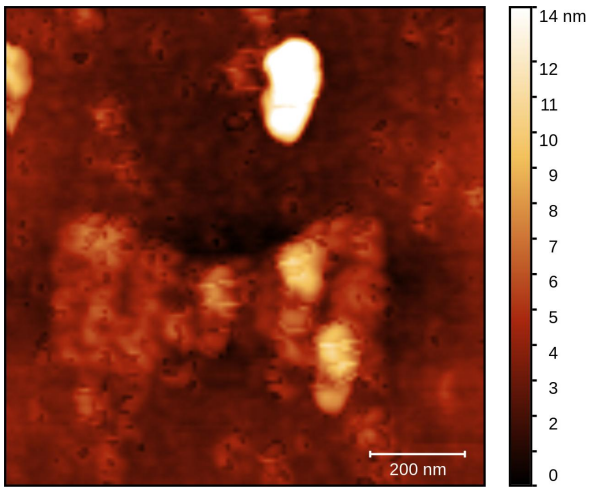


(a) Butterfly pattern after 10 minutes removal in acetone

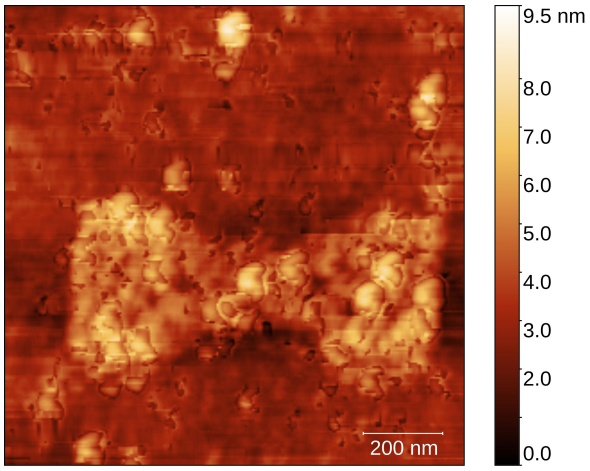


(b) Butterfly pattern after 10 minutes removal in acetone

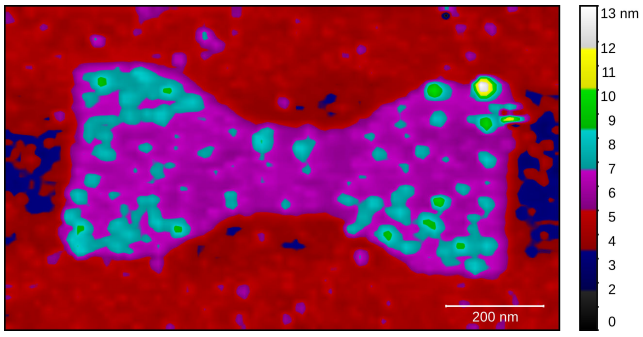


(c) Butterfly pattern after 1h removal in acetone

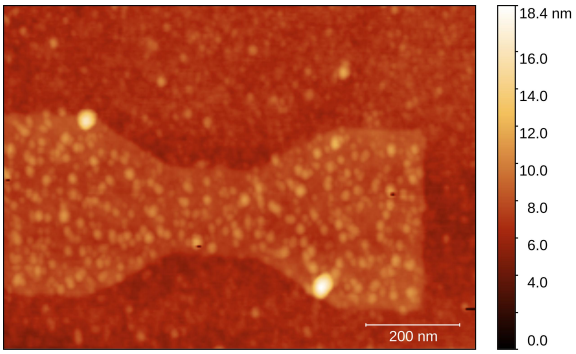


(d) Butterfly pattern after 1h removal in acetone

Figure 5.7: AFM images of butterfly patterns after removing the remaining resist with acetone for 10 minutes and 1h respectively. After both cleanings the sample was soaked for 1 minute in IPA and blow dried with air. The tip used for this set of scan is 10-15 nm golden tip.

The scanned butterflies after cleaning the sample with acetone for 15 hour are shown in figure 5.8. It can be seen, that the sample looks much more cleaner than the previous experiments, but still there are residues left of the PMMA resist on top of the graphene patterns and also features of the tip interaction with the surface. However from the collected images it is possible to retrieve the real dimensions of the structures. This is summarised in table 5.2. From the measurements it can be derived, that after removing the resist the dimensions of the butterflies are much more accurate in comparison with the taken dimensions of the resist. This suggest that the dimension error of the previous scans is likely due to tip convolution with the edges of the resist pattern. From the table it can be seen that the error rate of the width and length and the slope angle for structures with smallest feature size larger than 150 nm is less than 5 %. On the other hand, structures that have channel length smaller than 150 nm, the width and length shows similar error rates, but the slope angle variation increase to up to 10°. This can be also seen in figure 5.8c and 5.8d where the slopes from each side of the butterfly are not uniform.

Table 5.2: Dimensions derived from AFM images of the graphene butterfly structures after removing the resist with acetone for 15 hours

| Butterfly № | D_width ($W_{LS}$) nm | D_width ($W_c$) nm | D_width ($W_{RS}$) nm | D_angle (°) | Real Width ($W_{LS}$) nm | Real Width ($W_c$) nm | Real Length ($L_c$) nm | Real Width ($W_{RS}$) nm | Real angle (°) |
|---|---|---|---|---|---|---|---|---|---|
| #1 | 400 | 200 | 400 | 30 | 390 | 195 | 197 | 392 | 30-32 |
| #2 | 300 | 150 | 300 | 30 | 291 | 130 | 138 | 291 | 29-31 |
| #3 | 200 | 100 | 200 | 30 | 186 | 85 | 99 | 191 | 30-39 |
| #4 | 100 | 50 | 100 | 30 | 92 | 46 | 54 | 87 | 34-38 |

Note: The slope angle described in the table represents the minimum and maximum measured value of all slopes for the butterfly using Gwyddion. All dimension notations can be seen in figure 3.13.

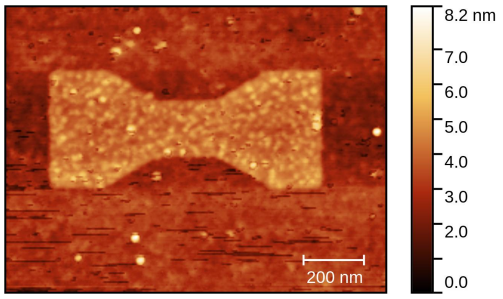


(a) Butterfly pattern (#1) with 200 nm intended channel

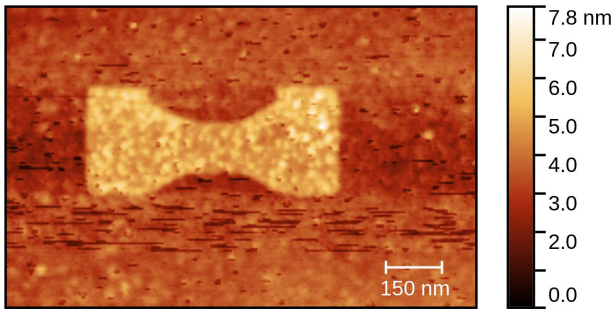


(b) Butterfly pattern (#2) with 150 nm intended channel

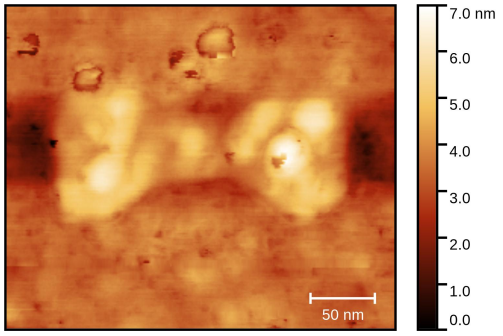


(c) Butterfly pattern (#4) with 50 nm intended channel

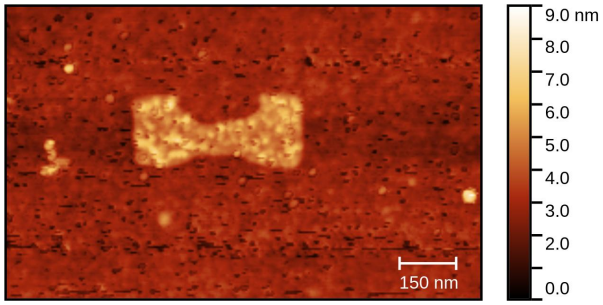


(d) Butterfly pattern (#3) with 100 nm intended channel

Figure 5.8: AFM images of butterfly patterns after removing the remaining resist with acetone for 15 hours followed by 1 minute in IPA and blow dry with air. The tip used for this set of scan is 8-10 nm golden tip.

In addition, SEM images are taken on the butterflies with intended channel dimensions of 50 nm to 200 nm. The SEM images of the patterns are visualised in figure 5.9 and their dimensions are summarised in table 5.3. The images that are obtained with SEM are not on the same butterflies as the ones taken during the AFM scan. The measured widths and lengths of the source, channel and drain are smaller than the ones taken from the AFM for the structures in sub 150nm. For device #1 the channel dimensions are measured to be closer to the ones intended by design. In addition, the angle variation of measured slopes for each butterfly have smaller variations in the range of 3 to 5°. The channel width of the smallest structure (#4) is measured to be 27 nm, which is almost twice as smaller to the width taken from the AFM (46 nm). Nevertheless, it can be seen that the shape of the butterflies for 50 nm, 100 nm and 150 nm differs from the ones imaged with AFM. This suggest that for this feature sizes the exposure with E-beam was not uniform and have larger variations.

Table 5.3: Dimensions derived from SEM images of the graphene butterfly structures after removing the resist with acetone for 15 hours

| Butterfly № | D_width ($W_{LS}$) nm | D_width ($W_c$) nm | D_width ($W_{RS}$) nm | D_angle (°) | Real Width ($W_{LS}$) nm | Real Width ($W_c$) nm | Real Length ($L_c$) nm | Real Width ($W_{RS}$) nm | Real angle (°) |
|---|---|---|---|---|---|---|---|---|---|
| #1 | 400 | 200 | 400 | 30 | 386 | 197 | 193 | 384 | 31-34 |
| #2 | 300 | 150 | 300 | 30 | 288 | 126 | 128 | 294 | 30-33 |
| #3 | 200 | 100 | 200 | 30 | 183 | 79 | 102 | 188 | 29-34 |
| #4 | 100 | 50 | 100 | 30 | 76 | 27 | 49 | 76 | 28-33 |

Note: The slope angle described in the table represents the minimum and maximum measured value of all slopes for the butterfly using Gwyddion. All dimension notations can be seen in figure 3.13.

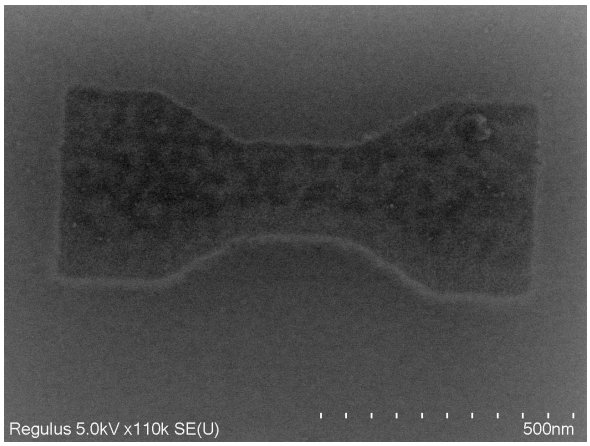


(a) Butterfly pattern (#1) with 200 nm intended channel

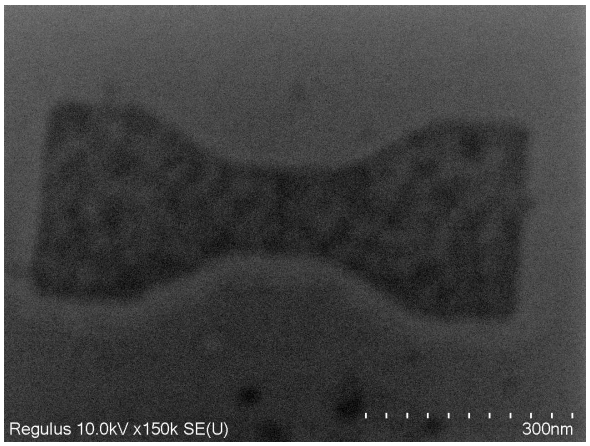


(b) Butterfly pattern (#2) with 150 nm intended channel

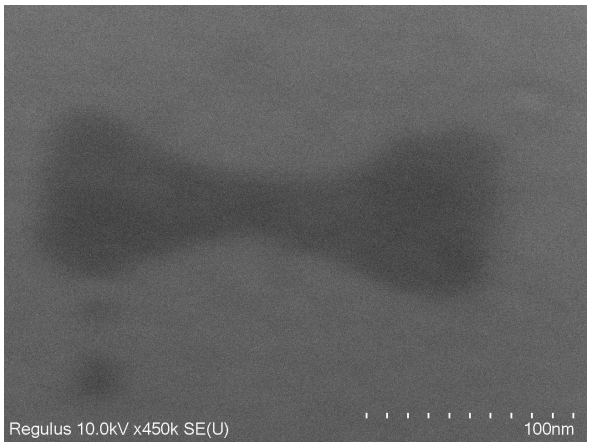


(c) Butterfly pattern (#4) with 50 nm intended channel

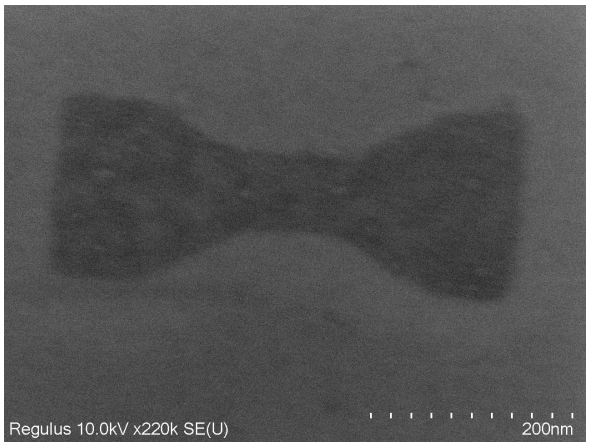


(d) Butterfly pattern (#3) with 100 nm intended channel

Figure 5.9: SEM images of butterfly patterns after removing the remaining resist with acetone for 15 hours followed by 1 minute in IPA and blow dry with air.

So far for the AFM images a semi-contact mode was used. The equipment used for AFM scanning supports also contact mode, which was used as an attempt to reduce the noise produced from the tip as in this mode the tip is in constant contact with the surface. However, using this mode completely destroyed the graphene pattern with channel length of 200 nm (figure 5.10a) and create a hole on the left side of the butterfly for the structure with channel length of 150 nm (figure 5.10b). Hence, the use of this method in the future measurements was

avoided.

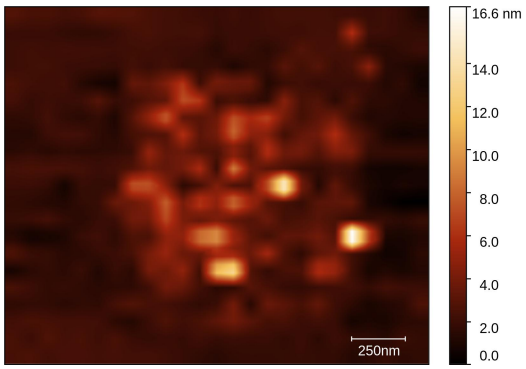


(a) Destroyed butterfly pattern with channel length of 200 nm

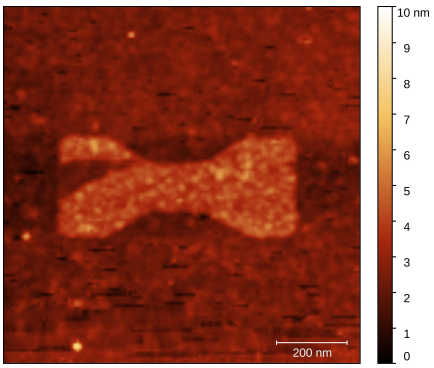


(b) Introduced damage on the left side of the butterfly using contact mode

Figure 5.10: AFM images of butterfly patterns using contact mode. The tip used for this set of scan is 8-10 nm golden tip.

Finally, AFM images are taken using very sharp diamond whiskers tip with diameter of the tip between 1 nm to 3 nm. The scanned structures with channel width of 50, 100 and 150 nm are present in figure 5.11. Using whiskers type tip, it was possible to obtain much more clear view of the topography of the substrate and see the contamination that is left on the GNR patterns.

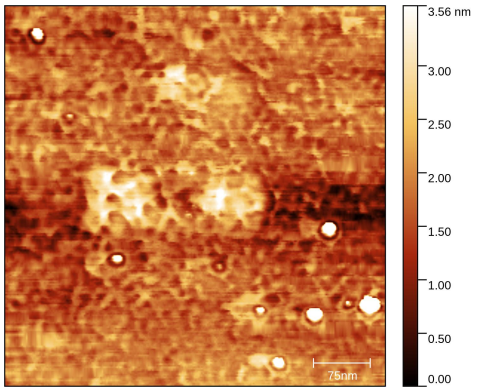


(a) Butterfly pattern (#1) with 200 nm intended channel

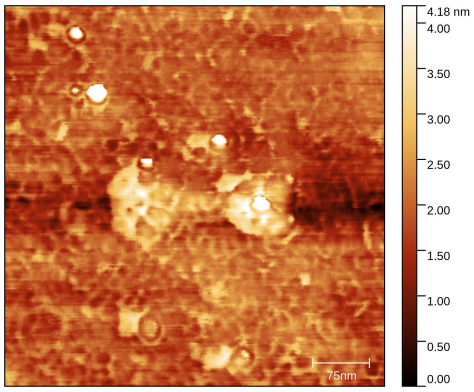


(b) Butterfly pattern (#2) with 150 nm intended channel

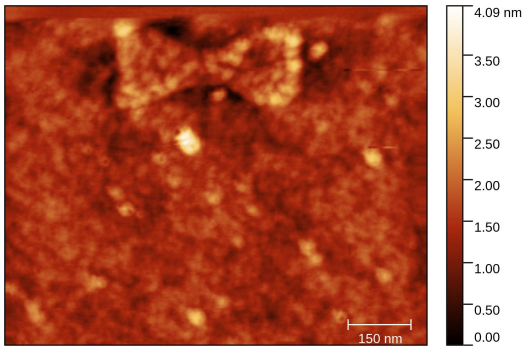


(c) Butterfly pattern (#4) with 50 nm intended channel

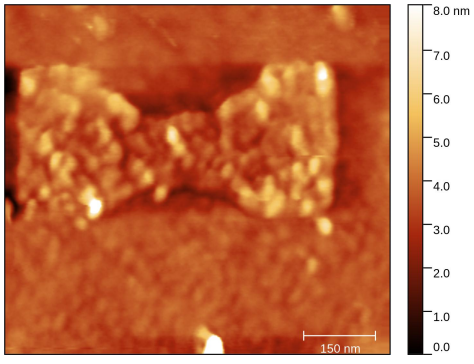


(d) Butterfly pattern (#3) with 100 nm intended channel

Figure 5.11: AFM images of butterfly patterns after removing the remaining resist. The tip used for this set of scan is 1-3 nm diamond tip.

Figure 5.12 presents an overview of the butterflies created with channel width of 50 to 150 nm. The image is taken using diamond whiskers with very sharp tip of 1 to 3 nm from which it can be seen the left contamination on the substrate. In addition, there are 4 visible dark spots left from the previously taken SEM images. Most likely this is because of the beam irradiation that causes formation of silicon-rich nanoparticles in the irradiated area. When the substrate leaves vacuum environment the surface of the formed silicon particles is re-oxidised and ideally the silicon network is destroyed. However, some of the silicon network might not be destroyed leaving the area of the chip still charged [2]. From the performed AFM characterisation of the substrate it is observed that the "cut offs" and rounded shapes at the edges are formed at the top part of the butterfly, while the bottom part of the patterns shows better slopes and edges formation.

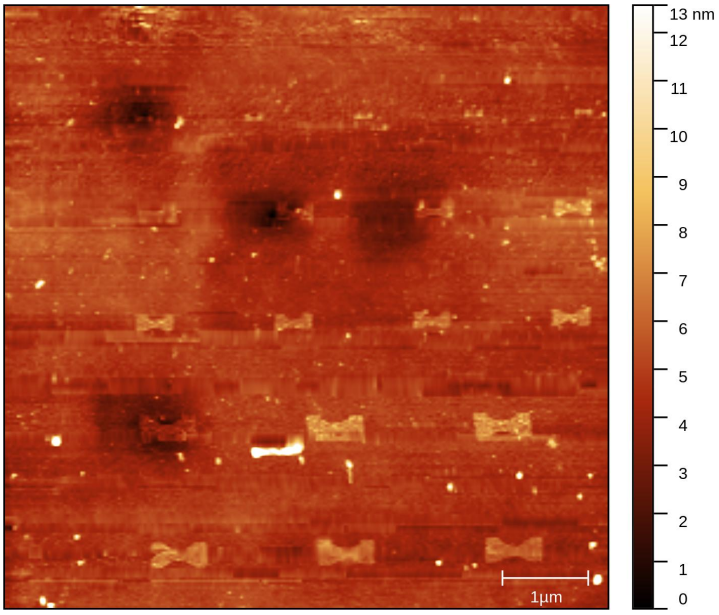


Figure 5.12: AFM images of butterfly patterns with 50 nm to 150 nm channel. The tip used for this set of scan is 1-3 nm diamond tip.

Unfortunately, the patterns with channel dimensions of 30 nm by design, was not able to be located on the sample. The performed characterisation of the area at which the structures were created revealed only the remaining contamination of the sample, with blob formations at the spots on which the butterflies were included by design.

### 5.3.1 Raman measurement of the four contact probe connection area

The performed Raman mapping was done on 7x7 um area covering part of the square and one of the connections to the golden pad. The design of the created patterns is explained in section 4.2.1. Increasing of the defects or a combination of armchair and zigzag edges is observed on the edges of the patterns as shown in figure 5.13a while in the inner parts of the square the defects decreases and towards the top left end the graphene shows ratios of pristine zigzag edge orientation. The $I_{2D/G}$ and FWHM shows the same characteristics for mono-layer graphene as it was observed in the previous scans of the sample. In addition, the FWHM shows a diagonal line, for which the width of the 2D band is between 31 to 33 $cm^{-1}$. The same area have also higher spectral width of the D band of approximately 16 $cm^{-1}$, which could suggest that this is a small fold or a grain boundary with stressed/strained carbon atoms.

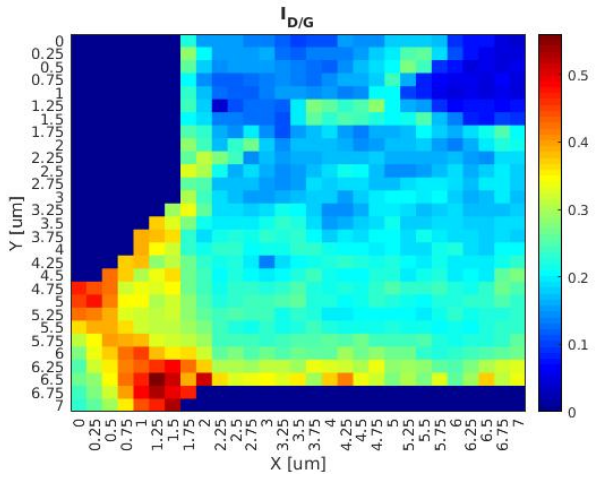


(a) Ratio intensity map for the "D" and "G" peak ratio

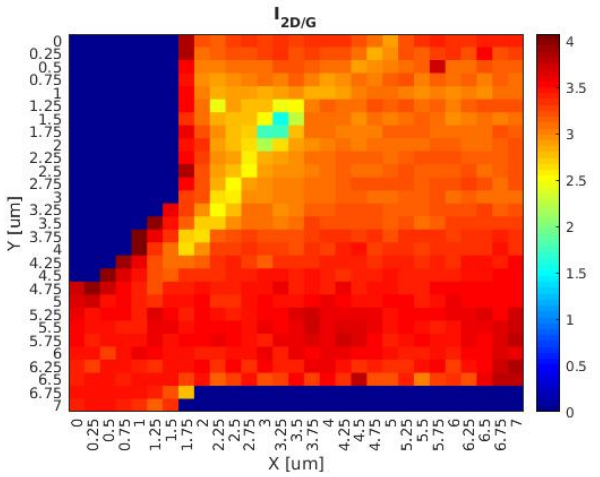


(b) Ratio intensity map for the "2D" and "G" peak ratio

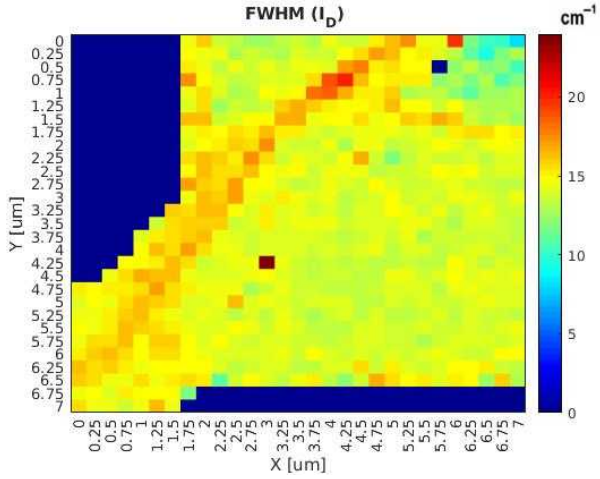


(c) Raman map for FWHM of the "D" peak

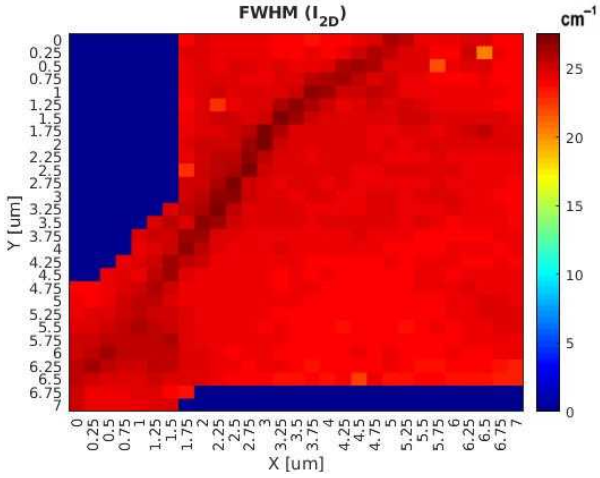


(d) Raman map for FWHM of the "2D" peak

Figure 5.13: Raman intensity maps of mono layer graphene bands and their ratios respectively. The wavelength of the Raman green laser is 514 nm, with spatial resolution of 1 $\mu$m. The scanned area is 7x7 $\mu$m$^2$ with a step size between each measurement of 250 nm.

## 5.4 Analysis of the oxygen plasma etched from the second batch of samples

For the oxygen plasma etched sample in this batch the analysis before removing the resist was skipped and the sample was cleaned directly with acetone followed by IPA rinse and blow dry with air.

### 5.4.1 AFM images of the butterfly patterns

As mentioned earlier, the dose test of the second batch of samples was skipped, because the focus of this batch of samples is on micron meter patterns which allows for creating a Raman maps and study the edge termination. Nevertheless, AFM images are taken on the included butterfly patterns with 200 nm channel. The images are visualised in figure 5.14 and their dimensions are summarised in table 5.4. As it was expected, the variation of the dimensions is larger compared to the samples from the first batch. From the results it can be seen, that the slope become less accurate with deviation of 15 to 22° for the structures created with intended angle of 60° by design. From the AFM images is also visible that the substrate looks more contaminated compared to the

images taken from the first etched sample with oxygen plasma in section 5.3. Tip artefacts, can contribute to some of the features showed in the figures, such as the holes with thickness close to 0 nm and the repeated small circles patterns that are visible on top of the structure. However, there are left residues from the PMMA, which are observed on the patterns itself and around them. This can be confirmed also from the image visualised in figure 5.14c.

Table 5.4: Dimensions of the graphene butterfly structures of second batch oxygen plasma etched sample

| Butterfly № | D_width ($W_{LS}$) nm | D_width ($W_c$) nm | D_width ($W_{RS}$) nm | D_angle (°) | Real Width ($W_{LS}$) nm | Real Width ($W_c$) nm | Real Length ($L_c$) nm | Real Width ($W_{RS}$) nm | Real angle (°) |
|---|---|---|---|---|---|---|---|---|---|
| #1 | 400 | 200 | 400 | 30 | 320 | 97 | 101 | 315 | 32-34 |
| #2 | 400 | 200 | 400 | 60 | 375 | 378 | 140 | 151 | 38-45 |

Note: The slope angle described in the table represents the minimum and maximum measured value of all slopes for the butterfly using Gwyddion. All dimension notations can be seen in figure 3.13.

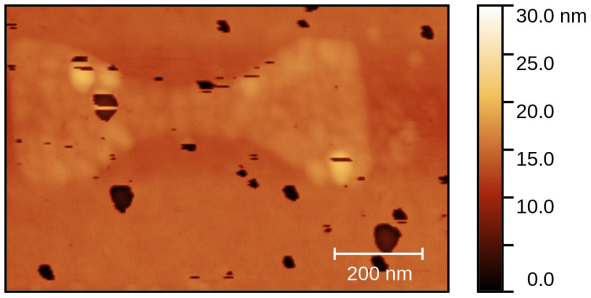


(a) Butterfly pattern #1 with 200 nm channel and slope of 30°

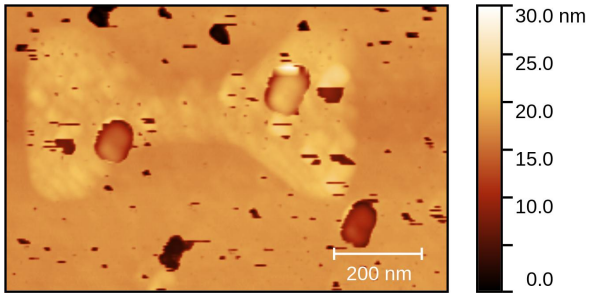


(b) Butterfly pattern #2 with 200 nm channel and slope of 60°

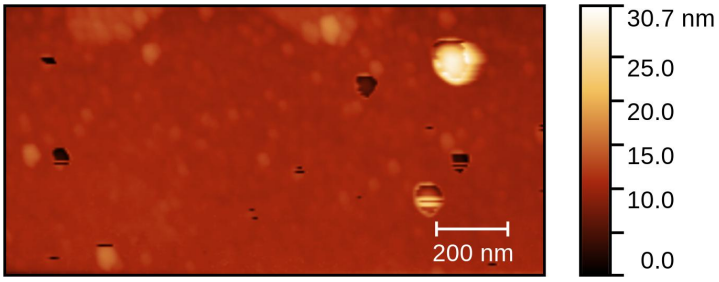


(c) Evaluation of the residues on the substrate

Figure 5.14: AFM images of butterfly patterns after removing the remaining resist with acetone for 15 hours followed by 1 minute in IPA and blow dry with air. The tip used for this set of scan is 8-10 nm golden tip.

### 5.4.2 Raman analysis of the substrate

The Raman maps in the following section are created by scanning each pattern individually and the results are merged into one graph without following the actual `X` and `Y` coordinates. Therefore the coordinates in the Raman maps are not written. The actual distance between each pattern for the squares is 5 $\mu$m while for the pentagons and hexagon is 3 $\mu$m.

Optical images of the scanned squares, pentagons and hexagons were taken using 100x magnification after cleaning the sample. The images are showed in figure 5.15. The rotation set by design of the squares, pentagons and hexagons is present in the middle of the pattern. For the pentagons and hexagons only a partial scan is performed, because the interest is to derive the edge termination and not to evaluate the quality of the basal

plane for each pattern.

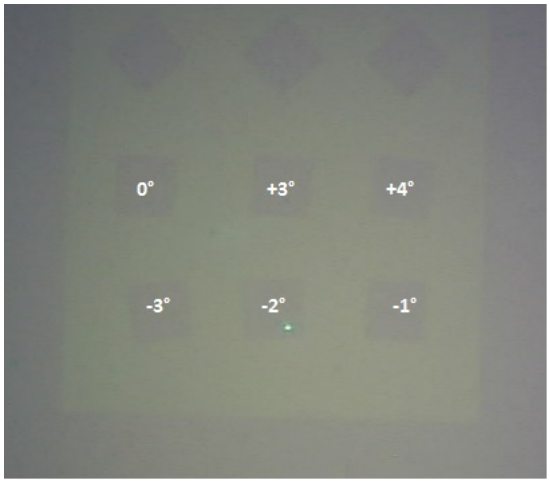


(a) Rotation of the squares on which Raman maps are preformed

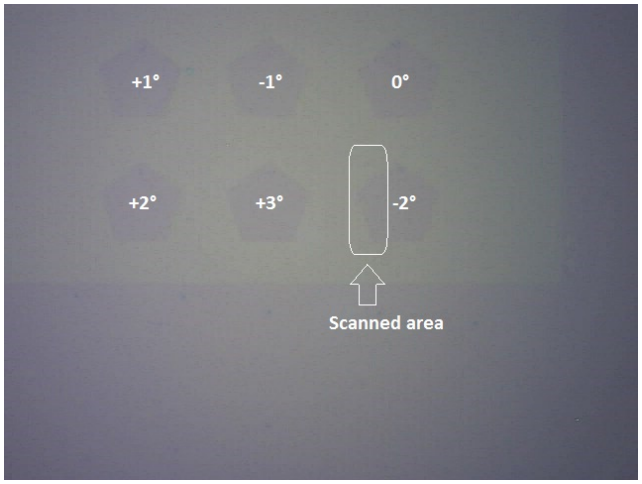


(b) Rotation of the pentagons on which partial Raman maps are preformed

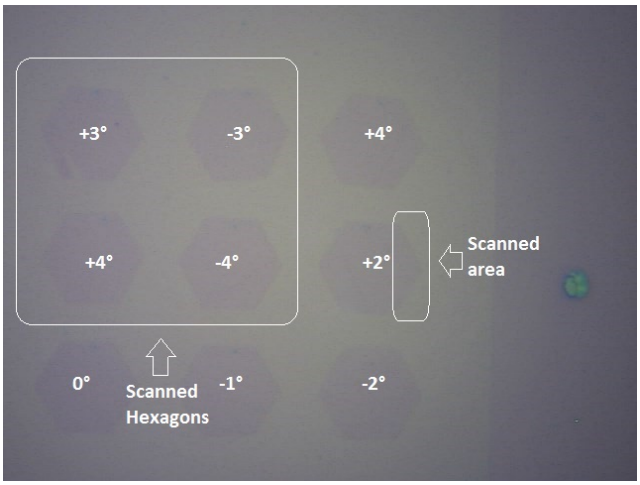


(c) Rotation of the hegaxons on which partial Raman maps are preformed

Figure 5.15: Optical image of the squares, pentagons and hexagons. The "-" sign denotes anti clock wise rotation, while "+" denotes clock wise rotation.

The obtained Raman maps for the hexagons are visualised in figure 5.16. For each hexagon the scan is performed with step size between each measurement of 250 nm. It can be seen that the $I_{D/G}$ ratio for the hexagon with rotation of +3° is the highest near the edges (up to 0.35), followed by the hexagon rotated on -3° which shows a raise around the edges to 0.2. The other two hexagons with rotation of ± 4° have a very few spots with introduced defects and the rest of the data suggest similar ratio compared to the ones taken from the initial Raman mapping of the substrate that was performed after the transfer process (section 5.1.1).

The $I_{2D/G}$ and FWHM for all hexagons is observed to be around of 24 $cm^{-1}$, with exception of two visible lines in the middle of the hexagons that are rotated on ± 4°. The raise of the FWHM(2D) is most likely caused from grain boundary or folded graphene.

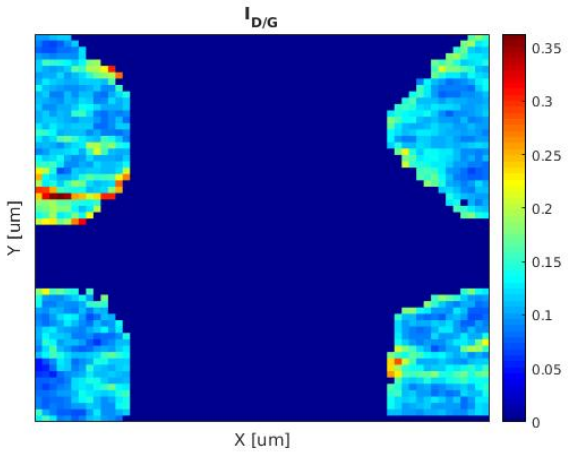


(a) Ratio intensity map for the "D" and "G" peak ratio

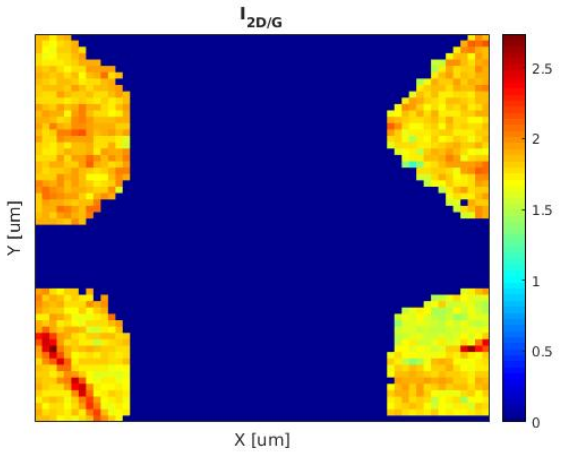


(b) Ratio intensity map for the "2D" and "G" peak ratio

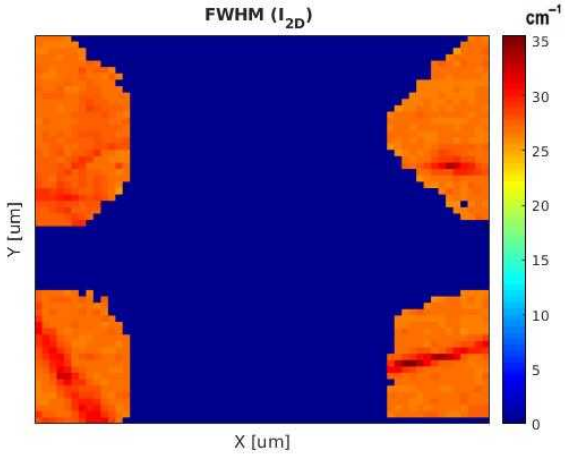


(c) Raman map for FWHM of the "2D" peak

Figure 5.16: Raman intensity maps of mono layer graphene bands and their ratios respectively. The wavelength of the Raman green laser is 514 nm, with spatial resolution of 1 $\mu$m. The scanned area of each individual hexagon is 12x4 $\mu m^2$ with a step size between each measurement of 0.25 $\mu$m.

In addition, Raman maps are performed on the patterned squares and pentagons. Figure 5.17 and figure 5.18 presents the $I_{D/G}$ and $I_{2D/G}$ ratios, FWHM of the D and 2D bands. For the squares, it can be seen that the least defects at the edges of the patterns is observed for the +3° rotation. The $I_{D/G}$ of this square is between 0.9 and 0.1, with small defects at the bottom left side of the pattern where the ratio increases to 0.17-0.19. For the rest of the squares the majority of the edges shows high defects with $I_{D/G}$ ratio of approximately 0.23 and small parts where the ratio increases up to 0.4. The $I_{2D/G}$ of all squares is between 1.6 to 1.8, with exception for the square rotated on -1° where the ratio raises to 2.1 - 2.3. From the FWHM of the 2D band for the same square, a grain boundary can be seen in the middle of the square, which shows a higher $I_{2D/G}$. Grain boundaries or folded graphene is observed on 4 out of 6 measured squares.

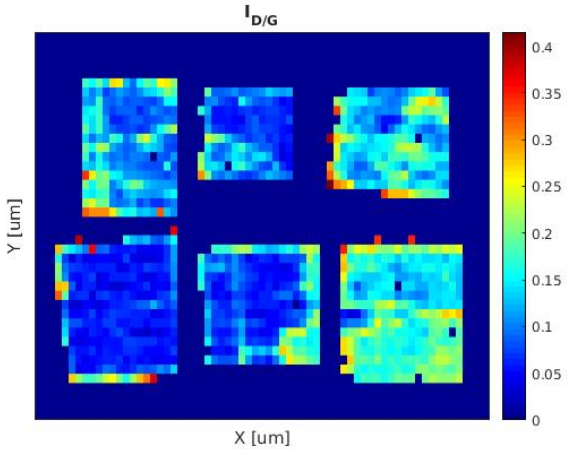


(a) Ratio intensity map for the "D" and "G" peak ratio

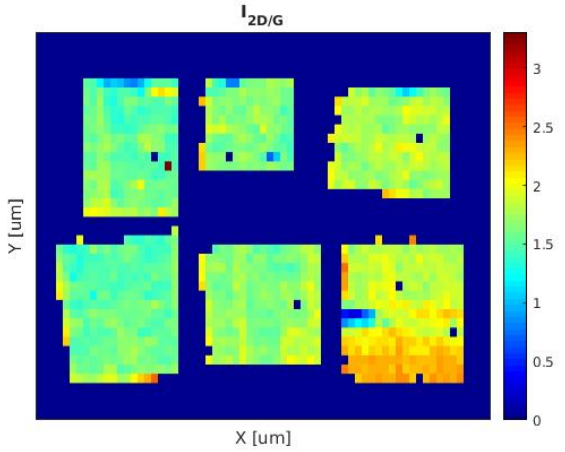


(b) Ratio intensity map for the "2D" and "G" peak ratio

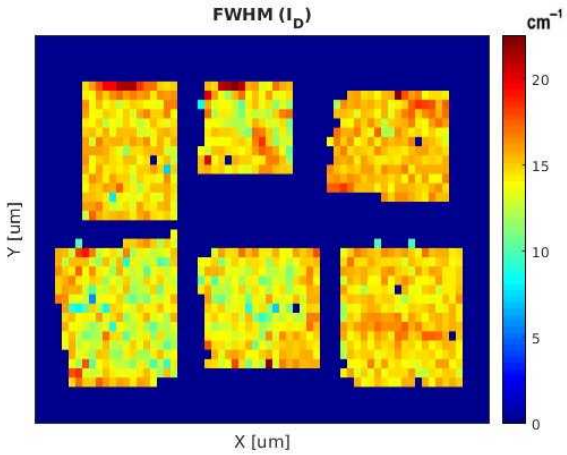


(c) Raman map for FWHM of the "D" peak

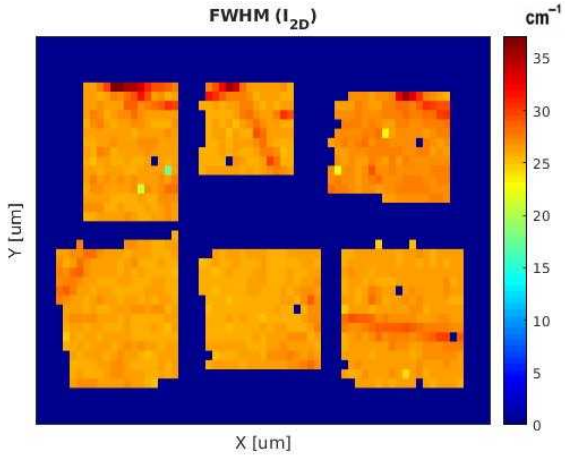


(d) Raman map for FWHM of the "2D" peak

Figure 5.17: Raman intensity maps using green laser with 514 nm wavelength and spatial resolution of 1 $\mu$m. The scanned area for each individual square is 5x4 $\mu m^2$. The step size between each measurement is 0.25 $\mu$m in horizontal direction and in vertical 0.35 $\mu$m.

Contrarily, the Raman maps (figure 5.18) that are performed partially on the pentagons, suggest that the $I_{D/G}$ ratio is the least for the pentagon with rotation of $+1^{\circ}$ with ratios between 0.12 to 0.15, while for the rest of the pentagons, at the edges $I_{D/G}$ increases to approximately 0.23 - 0.27. For all pentagons $I_{2D/G}$ ratios above 2 are observed and higher FWHM(D) between 15-18 $cm^{-1}$. Grain boundaries are observed in three of the pentagons from the FWHM of the 2D band.

The increased D peak can be caused not only by mismatch with the preferred edge orientation, but also from the oxygen plasma etching, left contaminants from the resist or initial defects introduced from the CVD growth graphene and transfer.

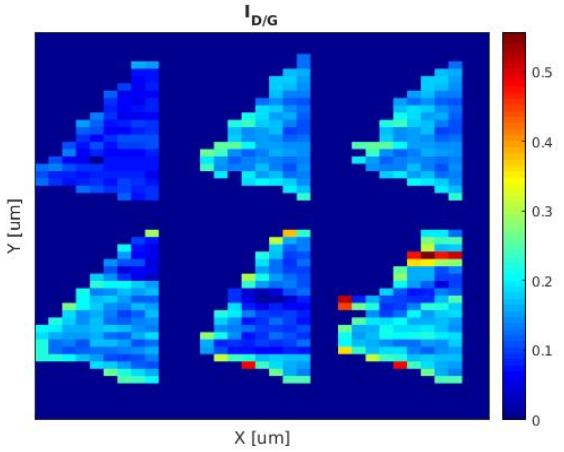


(a) Ratio intensity map for the "D" and "G" peak ratio

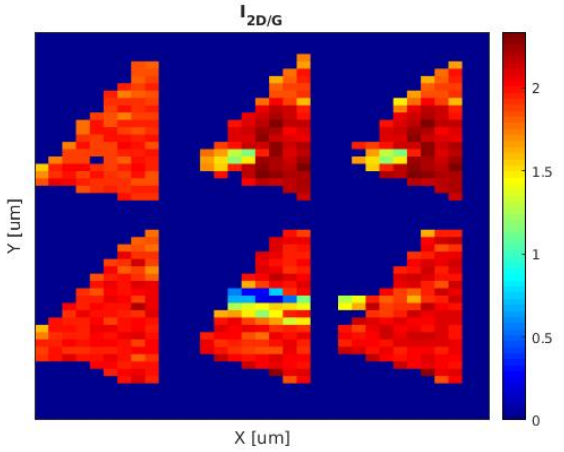


(b) Ratio intensity map for the "2D" and "G" peak ratio

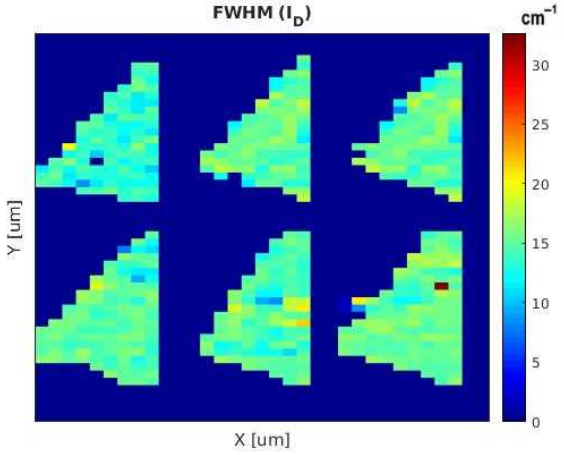


(c) Raman map for FWHM of the "D" peak

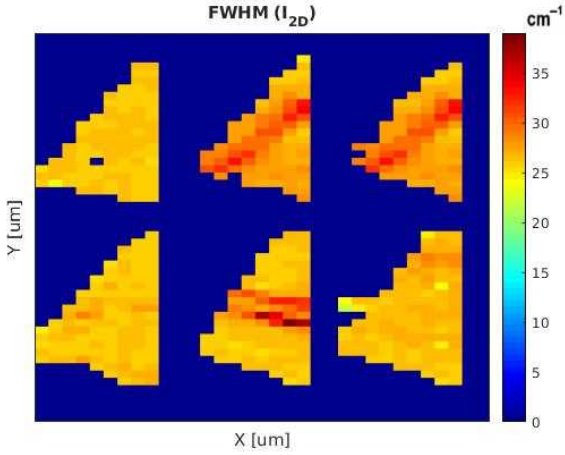


(d) Raman map for FWHM of the "2D" peak

Figure 5.18: Raman intensity maps of mono layer graphene bands and their ratios respectively. The wavelength of the Raman green laser is 514 nm, with spatial resolution of 1 $\mu$m. The scanned area for each individual pentagon is 2x8 $\mu m^2$. The step size between each measurement is 0.25 $\mu$m in horizontal direction and in vertical 0.35 $\mu$m.

Overall, from the comparison of different structures and rotations it was observed that the edge termination is not related to only one rotation. For hexagons the least amount of defects is observed at rotation of $\pm 4^\circ$ while for the squares at $+3^\circ$ and pentagons with rotation of $+1^\circ$.

Finally, Raman maps are taken on the butterfly with channel dimensions of 1 $\mu$m. The design of the butterfly is shown in figure 4.8 and the corresponding Raman maps in figure 5.19. It was observed that the $I_{D/G}$ ratio around the edges of the butterfly is increased to 0.19 at the upper part of the structure, while the bottom of the butterfly shows high defective regions with ratios of 0.25 - 0.3. Possible strains of the graphene pattern is observed on the same areas, but also small parts of the basal plane, for which $I_{D/G}$ is around 0.15 and FWHM(D) is 17 $cm^{-1}$.

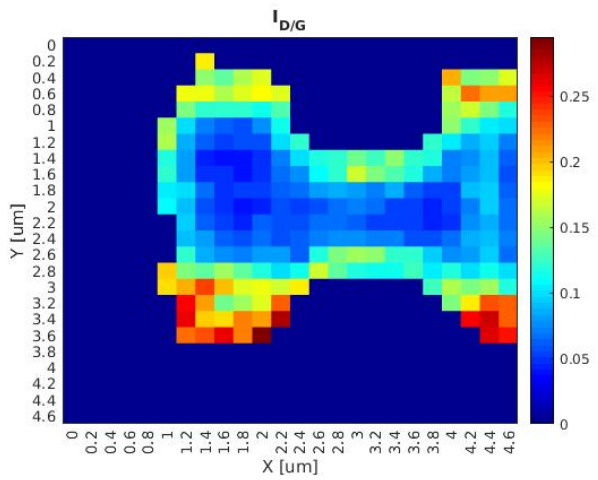


(a) Ratio intensity map for the "D" and "G" peak ratio

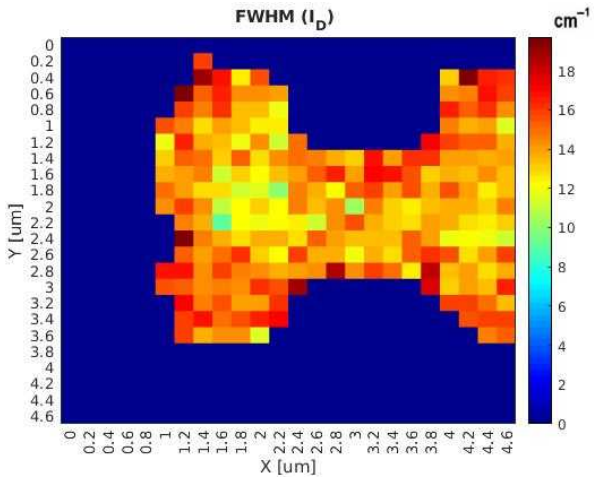


(b) Raman map for FWHM of the "D" peak

Figure 5.19: Raman intensity maps of mono layer graphene bands and their ratios respectively. The wavelength of the Raman green laser is 514 nm, with spatial resolution of 1 $\mu$m. The step size between each measurement is 0.2 $\mu$m.

## 5.5 Hydrogen plasma etching of graphene

Before etching the patterned substrate from the second batch with hydrogen plasma, a test is made on samples that have exfoliated graphene on them. The exfoliated samples can contain from mono layer graphene to graphite (multi layer graphene). The first test made on exfoliated sample was made with 20W power for 3 minutes and it was visually observed that damages are introduced to the silicon dioxide and most likely all graphene was etched away. Therefore, for the next runs the power and time was reduced. Figure 5.20 visualises the grain formation of the exfoliated sample before etching it with hydrogen plasma. After microscopic images were taken on the grains, the sample was etched with 10 W power for 1 minute and another set of images was performed. The microscopic image on the same area of the substrate is visualised in figure 5.21. It can be seen that the layers of the grains are reduced or removed completely. This experiment was run as a proof of concept that the tool can be used to remove graphene from the substrate.

After the proof of concept of the etching method was validated, another test was performed to study the edge termination, introduced defects after etching and the number of layers removed. The same power and etching time is used as in the previous experiment in order to etch a different sample. The $I_{D/G}$ ratio before etching the sample on one of the grains is visualised in figure 5.22a. After hydrogen plasma etching the same grain was scanned. It can be seen from figure 5.22b that $I_{D/G}$ ratio raised for the entire scanned area of the grain. Nevertheless, a further study of the etching effects on mono layer graphene covered with resist is required in order to conclude the efficiency of the hydrogen plasma deposition tool as an etcher. From the FWHM of the 2D peak it can be derived that the hydrogen plasma etching reduced the grains from four layers to bi-layer with some spots that shows three layer graphene. In addition, a test was performed on spin coated sample with PMMA and it was found that the hydrogen plasma etches the 0.45 nm PMMA per second, which is a good result as the thickness of the remaining resist on the patterns of the mono layer graphene samples is approximately 120 nm.

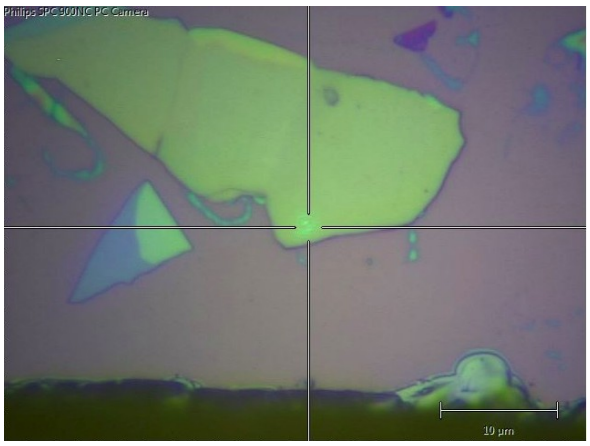


Figure 5.20: Exfoliated sample grains before etching with hydrogen plasma

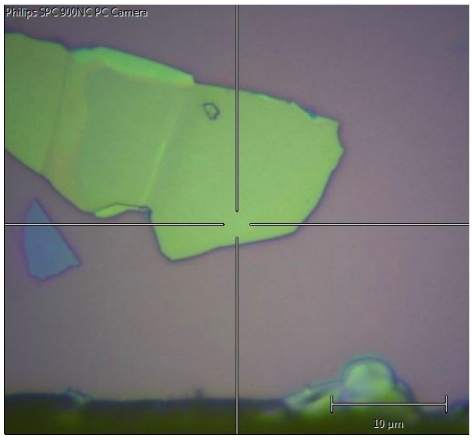


Figure 5.21: Exfoliated sample grains after etching with hydrogen plasma

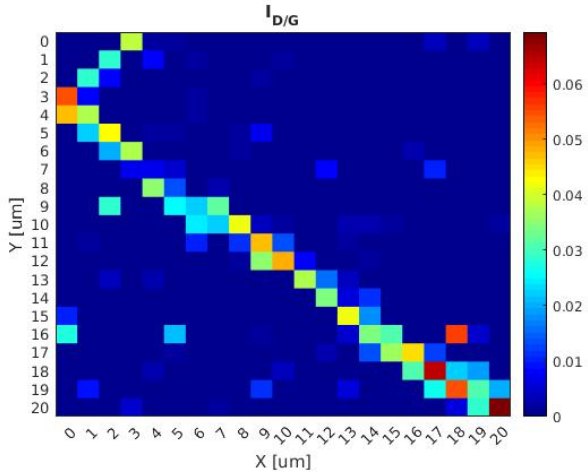


(a) Ratio intensity map for the "D" and "G" peak before etching

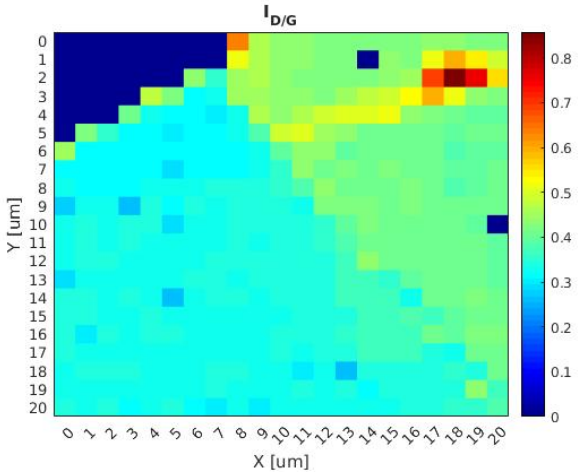


(b) Ratio intensity map for the "D" and "G" peak ratio after etching

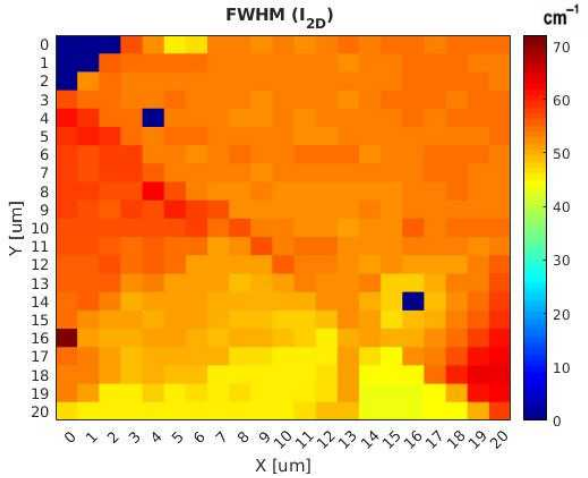


(c) Raman map for FWHM of the "2D" peak before etching

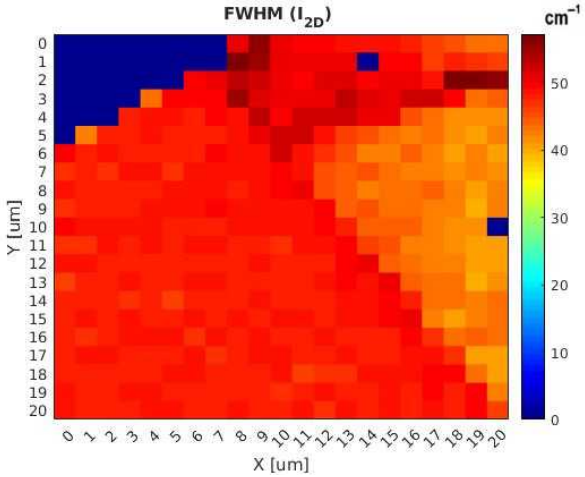


(d) Raman map for FWHM of the "2D" peak after etching

Figure 5.22: Raman intensity maps of exfoliated graphene grains. The wavelength of the Raman green laser is 514 nm, with spatial resolution of 1 um. The scanned area is 21x21 $\mu m^2$ with a step size between each measurement of 1 $\mu$m.

For the patterned substrate from the second batch, 5W power and etching for 30 seconds was used, followed by cleaning in acetone for 3h. The analysis of the sample after that showed that still a large part of the PMMA was not cleaned. Therefore, the sample was cleaned for another 15h. After cleaning the sample, Raman maps on two of the hexagons (#1 with rotation of +3°, and #2 with rotation +4°) are taken from the same area of the substrate for which the scan was performed on the oxygen plasma etched sample discussed in section 5.4.2. The result of the analysis is visualised in figure 5.23. It can be seen that, for both parts of the hexagons the ratio of $I_{D/G}$ is much higher compared to the one taken for the oxygen plasma etched sample, which suggest that the patterns are still contaminated. The high contamination of the sample is most likely caused from arcing that occur during the etching, which either introduces permanent damages to the sample, or the exposure to the plasma reacts in such a way with the PMMA resist that it cannot be removed effectively with acetone. From the FWHM(2D) of the hexagon rotated with +4° it was observed that it does not have the grain boundary or fold in the basal plane, as it was observed for the hexagon measurement from the previous experiment with the same rotation.

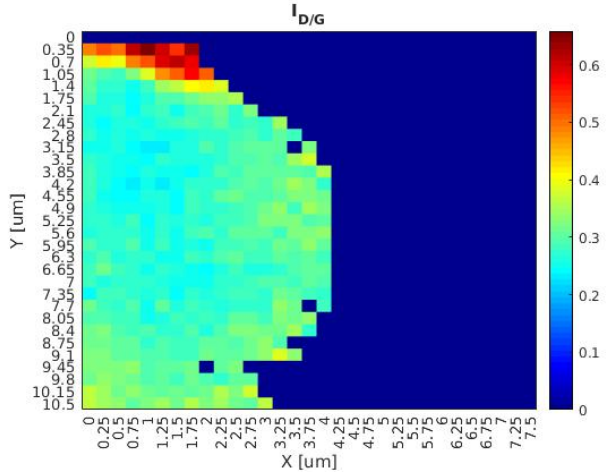


(a) Ratio intensity map for the "D" and "G" peak ratio for hexagon #1

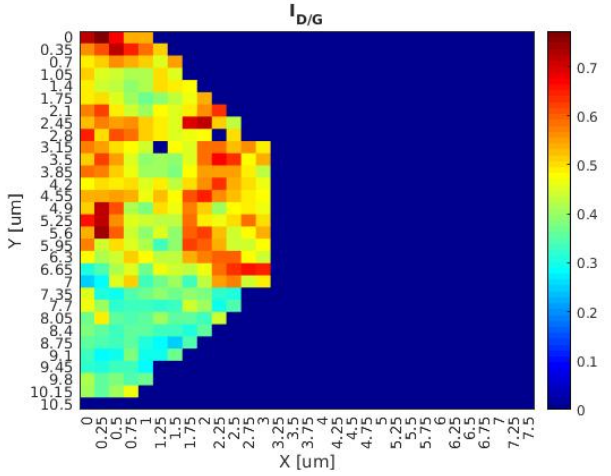


(b) Ratio intensity map for the "D" and "G" peak ratio for hexagon #2

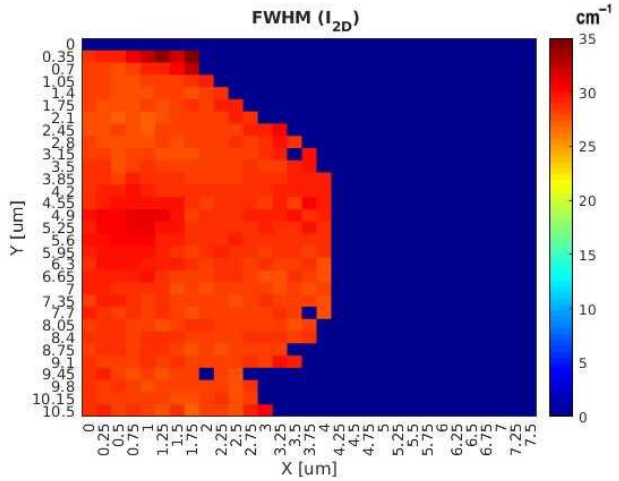


(c) Raman map for FWHM of the "2D" peak for hexagon #1

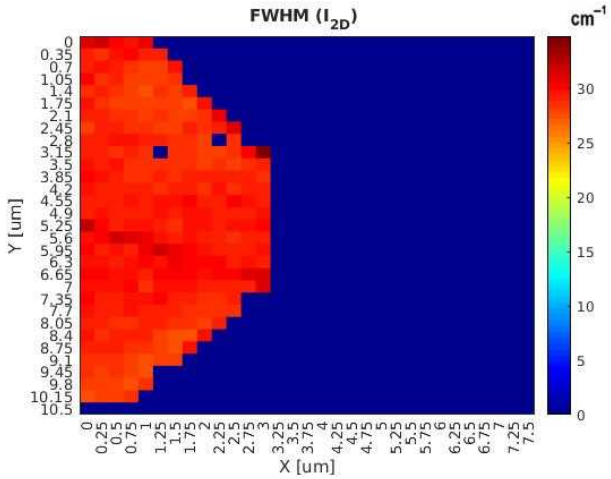


(d) Raman map for FWHM of the "2D" peak for hexagon #2

Figure 5.23: Raman intensity maps of etched hexagons with hydrogen plasma. The wavelength of the Raman green laser is 514 nm, with spatial resolution of 1 um. The scanned area is 12x4 $\mu$m$^2$ with a step size between each measurement of 0.25 $\mu$m.

In addition to the Raman maps, AFM images (figure 5.24 also confirms that the sample is quite contaminated after the extensive cleaning of 15h. Scan was performed on one of the butterflies with intended design channel of 200 nm (figure 5.25. This image suggest, that most likely the remaining resist on the patterns is with thickness of approximately 50 nm. Unfortunately, the left over part of the resist is not cleanable and left as a permanent damages.

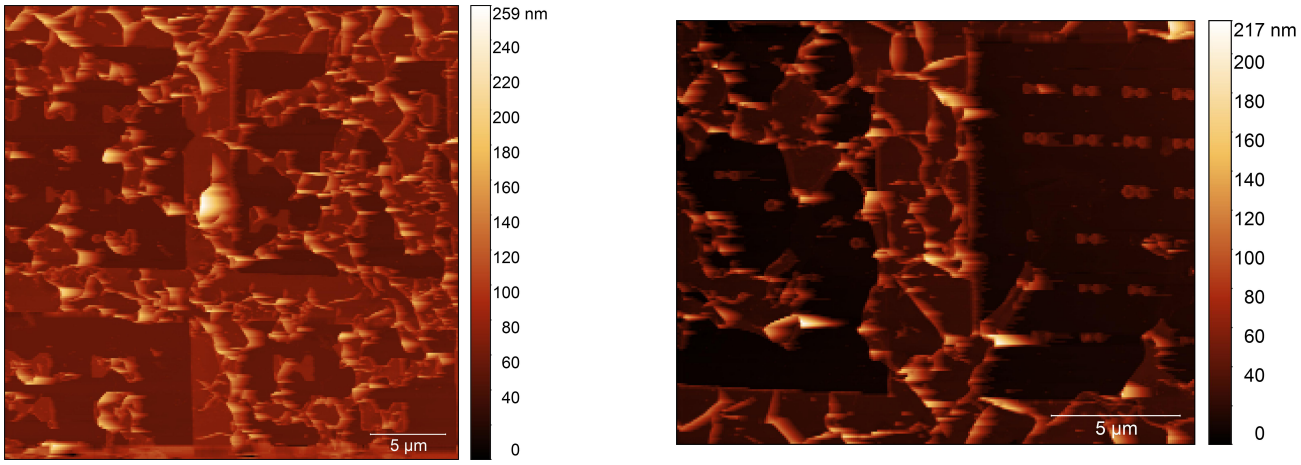


Figure 5.24: AFM images of the squares with butterfly patterns after removing the remaining resist with acetone for 15 hours followed by 1 minute in IPA and blow dry with air. The tip used for this set of scan is 8-10 nm golden tip.

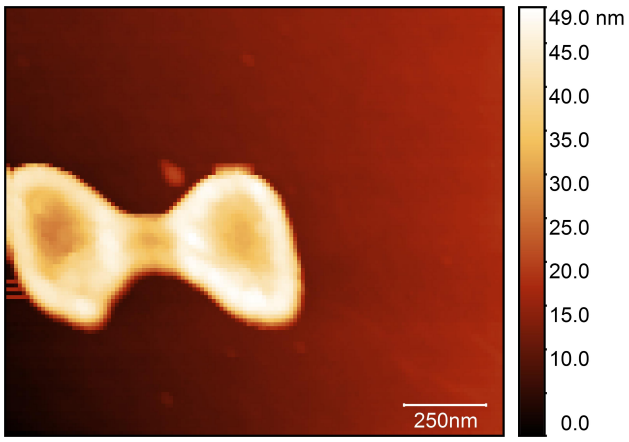


Figure 5.25: AFM images of the butterfly patterns with intended channel width and length of 200 nm. The tip used for this scan is 8-10 nm golden tip.

## 5.6 Carrier mobility extraction

The calculation of the electron/hole mobilities is adapted from [4] and [5].

A four contact probe measurement was not possible, due to the very small golden contact pads of 20 $\mu$m, that are used to connect the square pattern described in section 4.2.1. An attempt was made to connect, but only two out of four probes showed a resistance, which after trying to adjust the other two probes they lost contact. Therefore, electrical measurements in room temperature was performed using two probes on the butterfly patterns created between the 200 $\mu$m Au pads from the second batch of samples. The dimensions of the butterflies and their position on the chip are described in section 4.2. The measurement is performed by

supplying a constant voltage of 1V to one of the contacts, while the other was set to 0V. The back gate voltage was changed from -100 to 100V in order to find the Dirac point and extract the electron and hole mobility rates. The obtained transfer characteristics for the different butterfly patterns with channel dimensions of 1, 3, 7, 10 and 20 $\mu$m are visualised in figure 5.26. The the minimum current points ($V_{dirac}$) have been shifted to zero in order to normalise the extracted carrier mobilities to one point. The measured $V_{dirac}$ point is described later on in table 5.5.

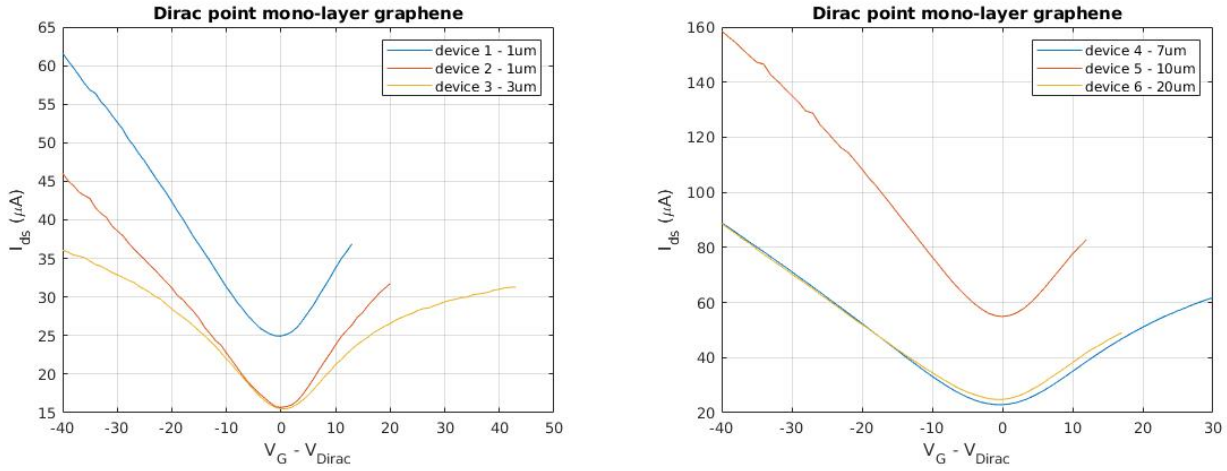


Figure 5.26: Transfer characteristics of butterfly patterns that have different channel lengths of 1,3,7,10,20 $\mu$m with 1V supplied as $V_{ds}$ and back gate voltage changes from -100 to 100 V.

The mobility is estimated from the slope $\frac{dI_{ds}}{dV_{gs}}$ of the linear part of the transfer characteristics using equation 5.1. This method of extraction is called direct transconductance method (DTM). In DTM the field-effect mobility is extracted according to the gate voltage dependent transconductance which does not take into account the contact resistance.

$$\mu = \frac{d}{W * C_{ox} * Vds} * \frac{dI_{ds}}{dV_{gs}} \tag{5.1}$$

where `d` is the length of the channel, `W` is the width of the channel, $C_{ox}$ is the $SiO_2$ capacitance and $\mu$ is the field-effect mobility. The $SiO_2$ capacitance is calculated using the formula 5.2.

$$C_{ox} = \frac{\epsilon * \epsilon_0}{t_{ox}} \tag{5.2}$$

where $\epsilon$ and $\epsilon_0$ are relative and absolute dielectric constant and $t_{ox}$ is the thickness of the $SiO_2$ layer, which for this substrate is 285 nm. Because of the complexity and accurately describing the butterfly shape is reduced as a three squares connected to each other that forms an approximate channel between the Au contacts. Thus, the expression $\frac{d}{W}$ is calculated using formula 5.3

$$\frac{d}{W} = \frac{d}{W_1 + W_2 + W_3} \tag{5.3}$$

where `d` is the contact to contact length taken as 100 $\mu$m and $W_{1-3}$ is the width of each square. $W_1$ and $W_3$ are the left and the right side of the butterfly for which the width is considered as constant of 40 $\mu$m, while the actual channel width created by design ($W_2$) is changed for each calculation from 1 to 20 $\mu$m. The carrier concentration can be calculated directly from the measured $V_{dirac}$ using equation 5.4.

$$n = \frac{C_{ox}}{e} * V_{dirac} \tag{5.4}$$

where e is the electron charge (e $\cong 1.602 * 10^{-19}$). Due to the neglecting of contact resistance, the calculated field-effect mobility would be lower than the real electron/hole mobilities. In addition to that the approximation of the channel, could also contribute to an increase or decrease of the mobility. The obtained results using equation 5.1 are plotted in figure 5.27.

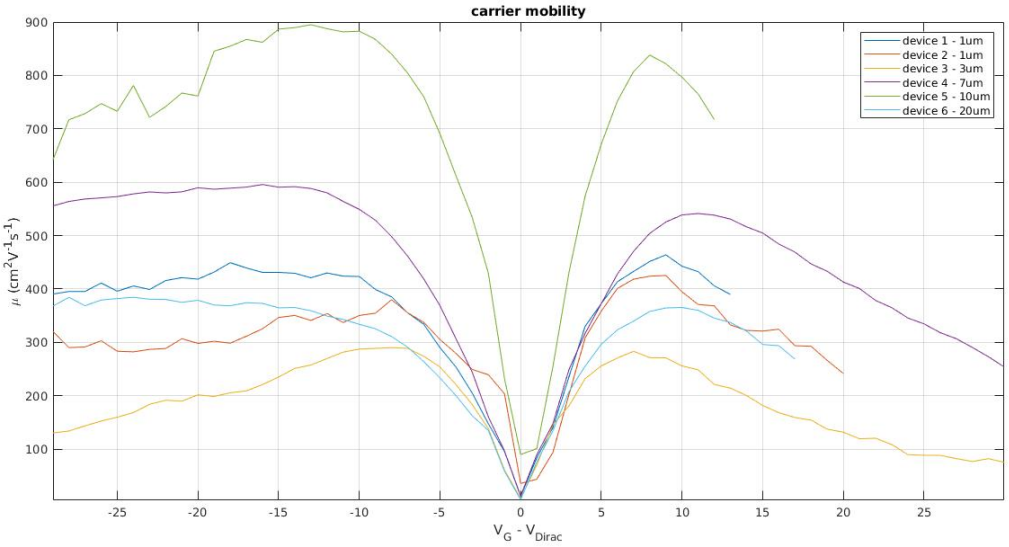


Figure 5.27: Carrier mobility extraction using DTM of butterfly patterns with different channel lengths of 1,3,7,10,20 $\mu$m.

Table 5.5: Measured Dirac voltages of devices with different channel length, extracted field effect mobilities and charge density.

| Device № | Channel length ($\mu$m) | Dirac Voltage $V_{dirac}$ (V) | Charge density n ($10^6 cm^{-2}$) | hole mobility $\mu$ (cm$^2$ V$^{-1}$s$^{-1}$) | electron mobility $\mu$ (cm$^2$ V$^{-1}$s$^{-1}$) |
|---|---|---|---|---|---|
| #1 | 1 | 87 | 1.90 | 399 | 414 |
| #2 | 1 | 80 | 1.19 | 379 | 401 |
| #3 | 3 | 57 | 1.17 | 290 | 283 |
| #4 | 7 | 70 | 4.15 | 528 | 525 |
| #5 | 10 | 83 | 1.80 | 882 | 838 |
| #6 | 20 | 77 | 1.73 | 325 | 339 |

From the summarised Dirac voltages in table 5.5 it can be seen that for all devices $V_{dirac}$ are positive, which means that from the adsorbed oxygen and water molecules on graphene the devices become p-doped. Furthermore, doping will introduce extra scattering for holes and electrons in graphene and thus lower their mobility. A correlation between the $V_{dirac}$ and carrier concentration shows that the charge density decreases when the Dirac point is shifted towards the positive direction. However, device #4 shows the highest charge density, that is approximately 2 times bigger than the ones calculated for device #1, #5 and #6. From the transfer characteristics, device #4 shows much steeper slope of the current for the negative voltage sweep. In addition the current measured at Dirac point is approximately 60 $\mu$A, which two times bigger than the one for the other devices and might be the reason for the calculated higher carrier concentration. From the obtained carrier mobilities, the device with 10 $\mu$m shows the highest electron and hole mobilities of 882 cm$^2$ V$^{-1}$s$^{-1}$ and

838 $cm^2$ $V^{-1}s^{-1}$ respectively. On the other hand, the lowest electron (290 $cm^2$ $V^{-1}s^{-1}$) and hole (283 $cm^2$ $V^{-1}s^{-1}$) mobilities are calculated for the structure with 3 $\mu$m channel.

# References


[1] S. Maghsoudy-Louyeh, M. Kropf, and Bernhard Tittmann. "Review of Progress in Atomic Force Microscopy". In: *The Open Neuroimaging Journal* 12 (Dec. 2018), pp. 86–104. DOI: 10.2174/1874440001812010086.

[2] Krishna Kanth Neelisetty et al. "Electron Beam Effects on Oxide Thin Films—Structure and Electrical Property Correlations". In: *Microscopy and Microanalysis* 25.3 (2019), pp. 592–600. DOI: 10.1017/S1431927619000175.

[3] Jian Shen et al. "AFM tip-sample convolution effects for cylinder protrusions". In: *Applied Surface Science* 422 (Nov. 2017), pp. 482–491. DOI: 10.1016/j.apsusc.2017.06.053.

[4] Francesca Urban et al. "Contact resistance and mobility in back-gate graphene transistors". In: *Nano Express* 1 (Mar. 2020), p. 010001. DOI: 10.1088/2632-959X/ab7055.

[5] Hua Zhong et al. "Comparison of mobility extraction methods based on field-effect measurements for graphene". In: *AIP Advances* 5 (May 2015), p. 057136. DOI: 10.1063/1.4921400.

# Chapter 6

# Conclusions and Recommendations

As CMOS scaling approaches the atomic feature size limit which results in a high power density and current leakage, low reliability and increased time and production cost, the need for new materials and devices is increasing. One of the promising materials to replace the CMOS technology is graphene. The goal of the thesis project is to analyse the limitations of achieving sub-50 nm GNR patterns, the effects on the edges from the fabrication steps and the influence of contaminants on the electrical properties.

A literature review was done in which the available methods for fabricating graphene patterns was investigated that covers the growth methods, transferring, patterning, etching and characterisation.

The simulation model described in Chapter 3 uses semi-empirical tight binding model in combination with NEGF in order to calculate the current flow through graphene butterfly patterns. The calculated current is used to derive the conductance changes based on the supplied top and back gate voltages. Different butterfly patterns were simulated with a smallest feature size of 10 nm or 30nm. The results showed that by modifying the dimensions of the butterfly different conductance can be obtained from which, by connecting the butterflies as complementary Boolean logic, it is possible to mimic the behaviour of an inverter, buffer, OR and NOR gates.

Based on the results from the simulation model the patterns with a channel of 30 nm and other test structures with dimensions above 50 nm such as butterflies, squares, pentagons, and hexagons are used to create different designs. The fabrication process used CVD graphene transferred to $SiO_2/Si$ samples. EBL was used to expose the designs on the samples follow by developing with 1:3 ratio of MIBK and IPA for 60 seconds. The exposed parts of graphene were etched with pure oxygen plasma for 30 seconds.

From the performed AFM/SEM characterisation, it was found that the created patterns below 50 nm were not present on the substrate. The patterns created with 50 nm channel by design were patterned successfully and the characterisation with AFM/SEM revealed that the channel width is smaller than the intended design by 5 to 50 %. Patterns that were designed with a channel below 150 nm are observed to have cut offs with no clear formation of slopes or rounded edges at the top part of the butterflies. On the other hand, for the bottom part the exposure was more uniform and the butterflies have distinguishable slopes and channel lengths. The characterisation of all butterflies with 200 nm channel showed that the dimensions of the device are very close to the ones intended by design and have a close to perfect edge formation. The most important steps towards obtaining correct ribbon dimensions is the exposure of the resist with EBL and developing of the sample which can be limited from multiple factors such as height of the sample with respect to the e-beam lens, tilt of the sample, variations in the resist profile, development time, vacuum level during exposure, humidity, vibrations and others. The non uniform exposure of the patterns at the top and the bottom part is most likely caused from the writing method of the EBL which exposes the design line by line.

From the Raman maps of the squares, pentagons and hexagons it was found that the least amount of defective

edges are observed at different rotations of the patterns, due to rotated grains by ± several degrees. Based on all of the performed Raman measurements the most likely edge orientation is random (combination of zigzag and armchair edges) with introduced additional defects from the etching, left contaminants from the resist or initial damages to the grains from the growth and the subsequent transfer process.

From the literature survey of the etching processes in section 2.3.3, remote hydrogen plasma is the only method that shows termination of the edges in zigzag direction. Based on this a test was perform to etch mono layer graphene using a DC hydrogen plasma. Arcing was observed during direct exposure to a DC hydrogen plasma which either made permanent damage to the resist or reacts with it in a way that was not possible to remove it with acetone efficiently. Highly defective pattern was observed from the taken Raman maps that showed $I_{D/G}$ ratios reaching 0.5. AFM images of the butterfly patterns also showed that the remaining resist on top of the patterns is with thickness of approximately 50 nm.

From the performed two contact probe measurements on all patterns a positive shift of the charge-neutral Dirac point voltage was observed, indicating p-doped graphene which is caused by the adsorption of oxygen, water molecules, and contamination left from the fabrication process.

Overall, there are multiple challenges to be resolved before graphene nano-ribbons can be used as building blocks for Boolean logic gates. The challenges starts with the growth process, which currently creates a poly-crystalline graphene from grains with different sizes in the range of nm to $\mu$m. Furthermore, grains can differ with several degrees in rotation that makes patterning the channels with the same edge termination as the desired one even more challenging. Transferring the graphene film to a substrate suitable for further processing can leave contaminants or introduce lattice defects. An attempt was made to determine the edge orientation before patterning using Raman (appendix B), but because of the formed poly-crystalline graphene film and the defects introduced to the basal plane from the CVD growth, the experiment was not successful. As it was already mentioned, exposure and developing of the sample can be influenced by many factors and have a significant impact on the dimensions of the ribbons. Oxygen plasma etching of graphene introduces edge defects, which affects the electrical properties of the patterns. Cleaning of the sample with chemicals such as acetone was observed that does not fully clean the graphene even after 15h of soaking. These contaminants are expected to reduce the electrical performance of the graphene and could be one of the explanations for the observed mobility in the range of 280 to 900 $cm^2$ $V^{-1}s^{-1}$.

## 6.1 Recommendation for future work

There are multiple actions to be taken in order to use mono layer graphene as a material for Boolean logic gates. Most of the actions are related to further optimisation of the fabrication process in order to obtain controllable and uniform patterns at specific feature size. Based on the work performed in this thesis the steps which can be taken as a follow up project are summarised below:

- STM is one of the methods which could achieve atomic resolution on the patterns created between the gold pads and etch with oxygen plasma, which can be used to evaluate the damages introduced to the edges.
- Cleaning the sample was observed to be challenging task. Left contamination of the ribbons results in doping, which would degrade the electrical properties of the ribbons. Thus, further investigation of how to clean effectively the sample without introducing damages to the edges or the lattice of the ribbons is necessary. One possible solution could be to perform initial cleaning of the sample using cold acetone for several hours followed by rinse in IPA and blow dry with nitrogen gun. To further clean the surface of the remaining contamination Raman laser with low power (10 - 30 mW) can be used as a heating source for several minutes which could result in decomposition of the PMMA.

- It was observed from the results in appendix E that when the sample is electrically isolated, hydrogen reacts very mild with graphene. This could mean that initial etching can be performed with hydrogen plasma followed by oxygen plasma in order to remove the rest of the graphene and potentially reduce the amount of defects at the edges of the patterns.
- Several samples are remaining with transferred mono layer graphene, which can be used to pattern structures with channel width of 50 nm or above and lengths in $\mu$m sizes. This will allow contact placement and perform temperature dependant measurements and study the changes in the Dirac point and mobility.

# Appendices

# A Raman spectroscopy measurements of 11 x 11 micron area using first polynomial fitting curve

From the created Raman maps using first polynomial fitting, it was observed, a area at which the graphene behave as it is folded or it is locally being lifted from the $SiO_2$. This can be seen from the FWHM of the 2D band and $I_{2D/G}$ ratio in figure 1c and figure 1b.

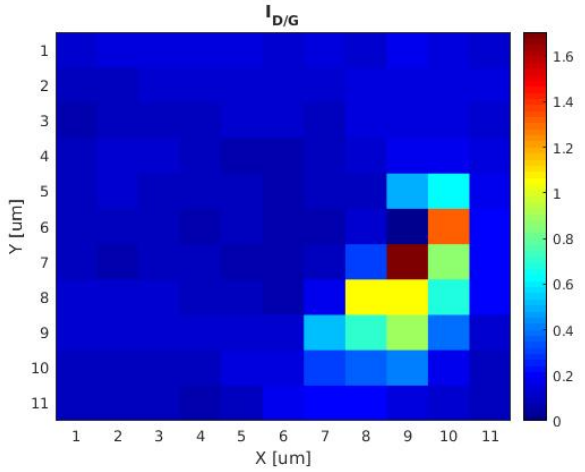


(a) Ratio intensity map for the "D" and "G" peak ratio

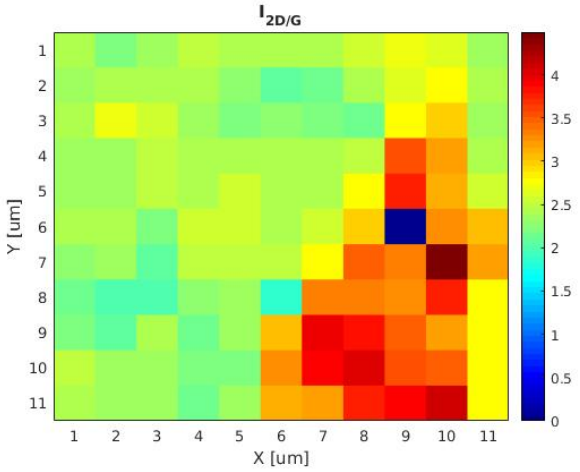


(b) Ratio intensity map for the "2D" and "G" peak ratio

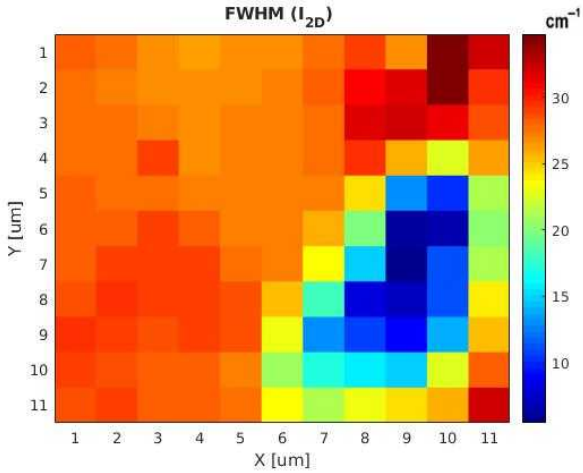


(c) Raman map for FWHM of the "2D" peak

Figure 1: Raman intensity maps of mono layer graphene bands and their ratios respectively. The wavelength of the Raman green laser is 514 nm, with spatial resolution of 1 $\mu$m. The scanned area is 11x11 $\mu m^2$ with a step size between each measurement of 1 $\mu$m.

To further analyse the reason behind the low FWHM expression and high $I_{2D/G}$, three random points are selected and the raw measurement is compared with the raw measurement from a point at which this effect was not observed. It can be seen from figure 2 that the signal is tilted for the selected three points in comparison to the measurement outside of this area. The tilt of the signal, most likely hides the real intensity rates of the peaks. In addition, the fitting algorithm might not be able to distinguish correctly the peak position and rate correctly which could lead to wrong ratio calculation. Another possible reason is that at this position of the substrate the graphene is folded or locally being lifted from the $SiO_2$.

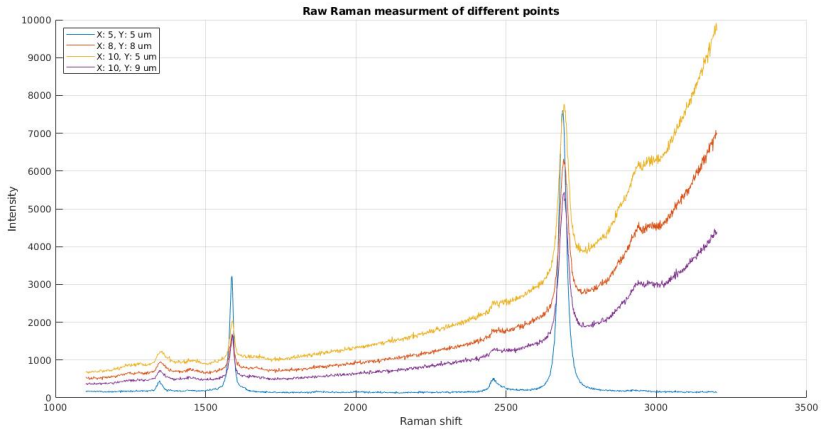


Figure 2: Raman raw measurement comparison of areas that shows a low FWHM expression, with a point for which the FWHM is within the set threshold.

In order to validate the origin of the error the fitting curve of the algorithm for the tilted signals is analysed. Figure 3a shows that using first order polynomial curve fitting is not able to correctly detect the D peak, and 2D peak becomes narrower as the starting points are moved towards the middle, which confirms that the origin from the error comes from the fitting algorithm. Therefore, a higher polynomial curve fitting is used to accurately detect the peaks and their true starting points. It was found that fourth order of polynomial curve fitting is able to accurately detect the peaks as shown in figure 3b.

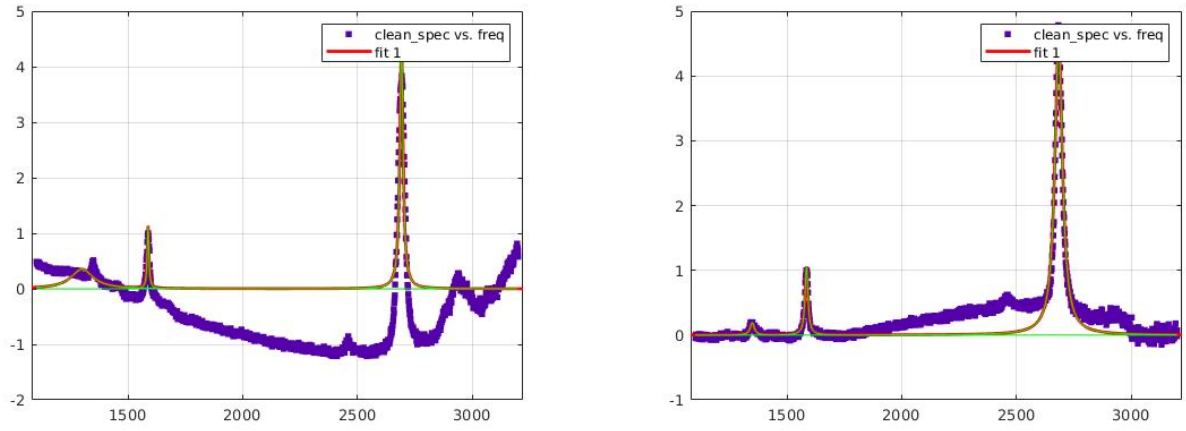


(a) Raman raw measurement fitted using first order of polynomial curve fitting.

(b) Raman raw measurement fitted using fourth order of polynomial curve fitting.

Figure 3: Lorentzian fitting of the Raman measurements using different orders.

# B Determining the orientation of the transferred graphene

One of the substrates after transfer process is used to perform experiment in order to study the edge termination of the graphene grains. In total, two experiments are performed on the same area of the chip, but between each experiment the substrate is rotated 90 degrees.

The expected theoretical outcome is that for one of the experiments the D peak is present, while for the other the D peak should be much smaller or not visible at all. In this case the absence of the D peak would suggest

a pristine graphene with zig-zag edges. However, the transferred graphene is poly crystalline which contains unavoidable topological defects at the grain boundaries consisting of non-hexagonal carbon rings. Thus, the scan is performed inside the grain and not at the grain boundary, because at the grain boundary the edge termination is not likely to be determined as the measurement will capture the introduced defects, instead of the edges. In addition mechanical deformations and contamination left from the transferring are very likely to be present. Thus, the expected outcome of the experiment is that for all measurements the D peak to be visible, but at one of the chip rotations to have lower value.

The spot chosen to perform both of the experiments is near one of the gold markers located at the middle of the chip. This position of the substrate allows for easier location after rotating or moving the substrate. For experiment #1 the armchair edges are suppose to be located in the `x` direction of the substrate (horizontally) based on the requested edge orientation made to the external company. The preferred edge orientation is discussed in section 4.1. The scanned area is visualised in figure 4. For experiment #2 the chip was rotated on 90 degrees (figure 5) and the starting point for the experiment was as much as possible chosen to be the same as performed in experiment #1.

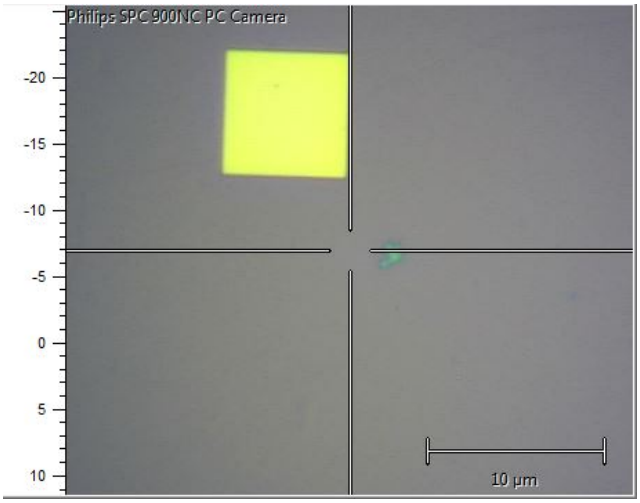


Figure 4: Experiment #1 scanned surface of 15x15 micron

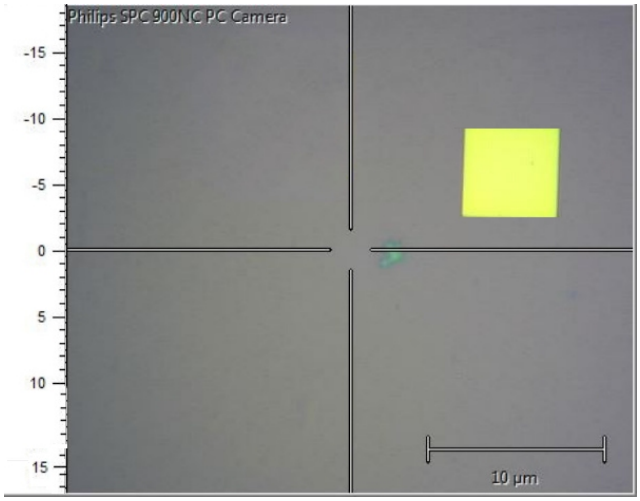


Figure 5: Experiment #2 scanned surface after 90 degree rotation.

It is worth noting, that manual rotation of the chip is very likely to cause a difference between both experiments (i.e the angle on which the chip is placed, the laser spot size on the chip, the starting point of the experiment, external light interference, the heating of the laser and etc.). All of this can contribute for less accurate result. In order to avoid the laser influence to the final result, the $I_{D/G}$ ratio is used as comparison, instead of taking the D peak intensity from each measurement. As alternative method to perform this analysis is to change the polarisation of the laser between each experiment, which will eliminate the potential errors coming from manual rotation [1]. The authors of the paper showed experimentally that for an-isotropic D band which is the case for edges, it is possible to distinguish the type of the edge. Armchair edges can be detected by changing the laser polarisation to 45°. They have also observed that introduced edge defects from grain boundaries give rise to double resonance processes, which makes the intensity of the D band isotropic and does not depend anymore on the light polarisation direction. However, the Renishaw system that was used to perform the Raman experiments, does not support changing the polarisation of the laser, hence this type of experiment was not performed.

In order to analyse the data, the $I_{D/G}$ ratio of each measurement is compared individually for all scans and a percentage difference between experiment #1 and experiment #2 is plotted as a heat map in figure 6. The

formula used to derive the percentage difference between both peaks is described below.

$$B_{(i)} = \frac{I_{D/G}Experiment\#1_{(i)} - I_{D/G}Experiment\#2_{(i)}}{I_{D/G}Experiment\#2_{(i)}} * 100 \quad (1)$$

where **i** is the index of each block and B is the final percentage difference.

It can be seen, that for each block the D peak value of experiment #1 is higher by at least 5 % compared to the peak value taken from experiment #2. Despite the fact, that the results shows a difference in the $I_{D/G}$ ratio, to accurately detect the edge termination, the measurement should be performed at the edges of the grains and not in the basal plane. But, at this stage the graphene is poly-crystalline with grains touching to each other or overlapping, which makes it not possible to perform scan at edge of the grains. Furthermore, CVD growth graphene is not pristine graphene, which consist of defects in the basal plane as mentioned in section 2.1.3. This means that by scanning the basal plane it is very likely to probe the defects and rotations of the sample to cause increase of the D peak. Thus, the experiment is considered as not successful.

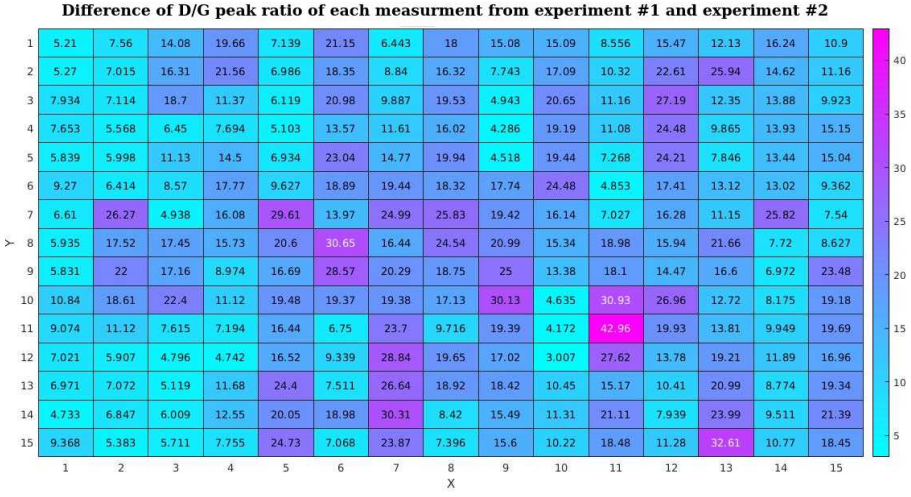


Figure 6: Percentage difference of the $I_{D/G}$ peak ratios for experiment #1 and experiment #2

# C Raman maps of the butterflies with 50-200 nm channel before cleaning the sample

To verify that the mono layer graphene patterns are still below the resist and not etched away from the oxygen plasma a Raman mapping of the square that contains the bigger butterfly structures is performed. Figure 7 shows the intensity maps for 10x10 $\mu m^2$ using green laser with 514 nm wavelength and step size between each measurement of 350 nm. The intensity map of the $I_{2D/G}$ (figure 7b) and FWHM (figure 7c) shows ratios that are in the range of the set threshold values for mono layer graphene in section 5.1. However, the analysis of the "D" peak suggest that the etching process introduce defects in the mono layer graphene lattice, or that the remaining resist influences the measurement that leads to higher values of the "D" peak. This can also be seen from the $I_{D/G}$ in figure 7b, where the spots on which graphene is detected have ratios in the range between 0,6 and 1,6. This ratios are higher than the set threshold of 0,1 or below.

One limiting factor of performing Raman maps on small features is the spatial resolution, i.e the spot size that interacts with the substrate, that can be set to approximately 1 $\mu$m at the highest magnification. This does

not allow to see the patterns it self, but also some of the measurements covers the whole pattern itself and the defects from all sites of the structures are registered.

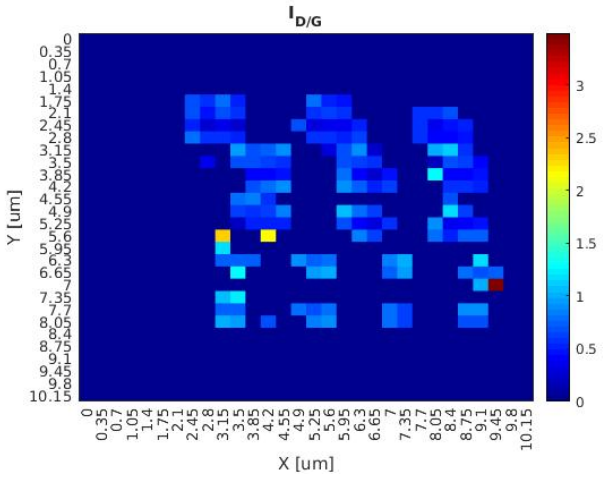


(a) Ratio intensity map for the "D" and "G" peak ratio

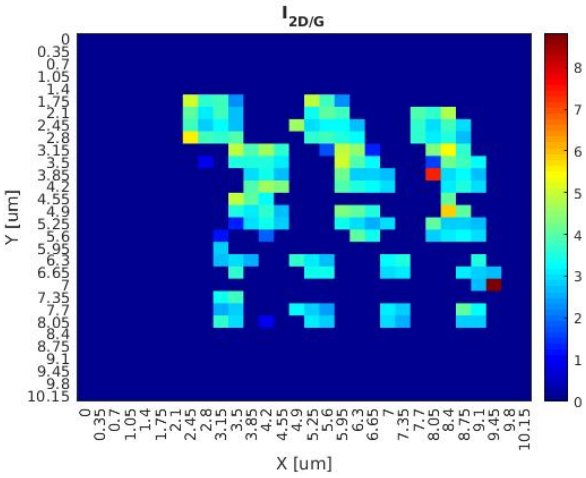


(b) Ratio intensity map for the "2D" and "G" peak ratio

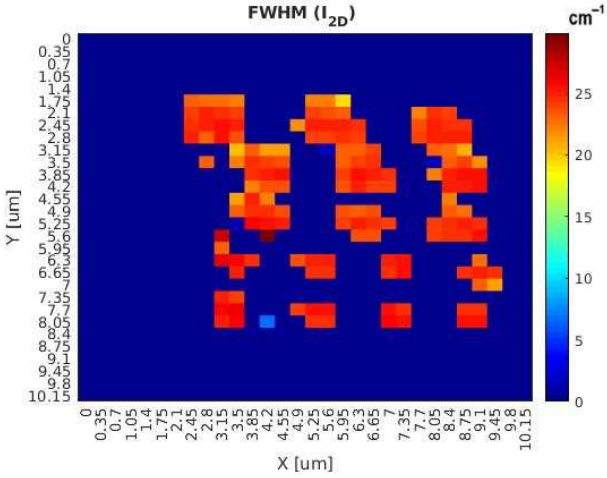


(c) Raman map for FWHM of the "2D" peak

Figure 7: Raman intensity maps of mono layer graphene bands and their ratios respectively. The wavelength of the Raman green laser is 514 nm, with spatial resolution of 1 $\mu$m. The scanned area is 10x10 $\mu$m$^2$ with a step size between each measurement of 350 nm.

# D Raman maps of the butterflies with 50-200 nm channel after cleaning for 15h with acetone

Figure 8 shows the intensity maps for 10x10 $\mu$m$^2$ area using the same laser settings and step size of the measurement as the previously performed experiment. Due to shifting of the starting point for the measurement, external variations and large spot size of the laser interacting with the sample, the scanned patterns does not show the same formation as in appendix C. However it can be derived, that the large "D" peak value (figure $I_{D/G}$) ratio is not influenced by the resist, but that the mono layer graphene patterns have indeed introduced lattice defects and part of which can be edge defects. Nevertheless, the $I_{2D/G}$ (figure 8b) and FWHM (figure 8c) remained in the set threshold for mono layer graphene.

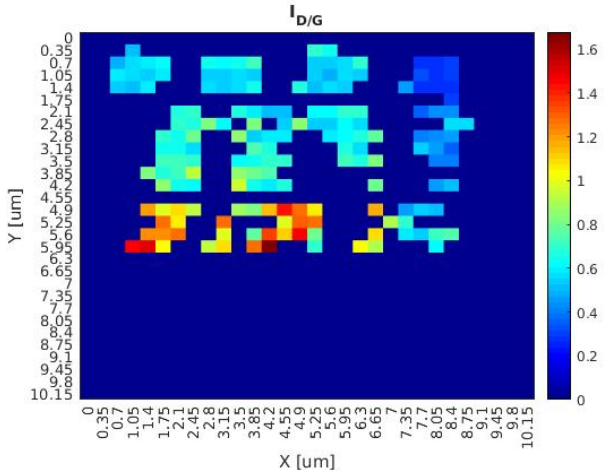


(a) Ratio intensity map for the "D" and "G" peak ratio

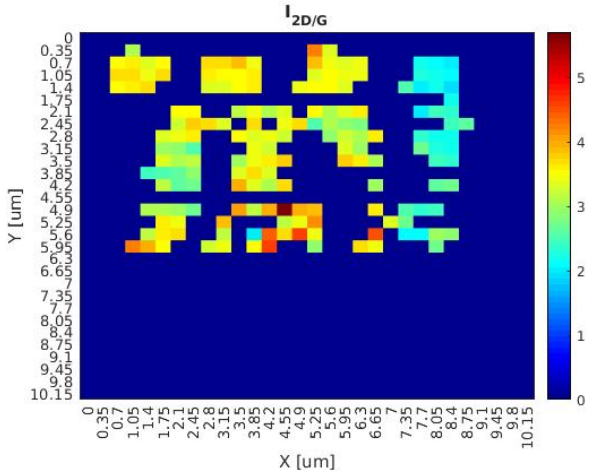


(b) Ratio intensity map for the "2D" and "G" peak ratio

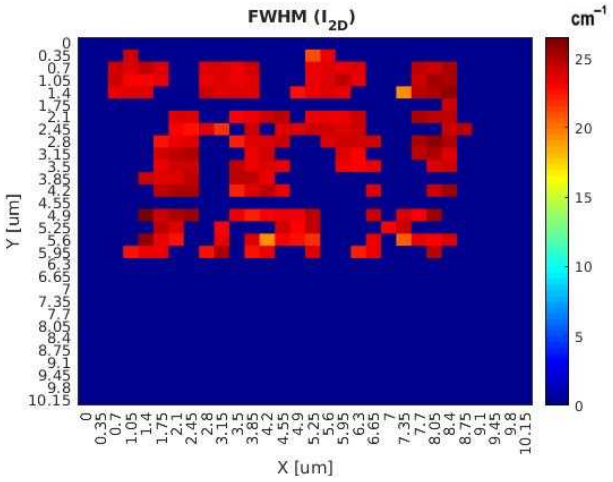


(c) Raman map for FWHM of the "2D" peak

Figure 8: Raman intensity maps of mono layer graphene bands and their ratios respectively. The wavelength of the Raman green laser is 514 nm, with spatial resolution of 1 um. The scanned area is 10x10 $\mu m^2$ with a step size between each measurement of 350 nm.

# E Remote hydrogen plasma etching

The sample was placed on a plate which serves to electrically isolate the sample with the plasma and remove the arcing effect, that was observed when sample was exposed directly to the hydrogen plasma. Four experiments were performed, with different etching times and different power. The results are visualised in figure 9 and compared with the measurement before etching. It can be seen that, after 30 seconds etching with 5W, the high D-peak shows that the hydrogen reacts with the graphene and start introducing defects. The 2D band is observed to become wider and less intense, which is another indication that the hydrogen plasma introduces damages and destroys the graphitic chemical structure. After 5W and 5 min of etching, the 2D band almost disappear, but still G and high D peaks are observed. The followed up etchings for 10 and 30 minutes showed appearance of the G and D peaks which remains almost the same that makes it not possible to etch the remaining part of the graphene. In addition, after each etching iteration the thickness of the resist on top of the structures decreased, where after the last test was visible that a large part of it was etched away. The changes in the thickness of the resist can be seen in figure 10.

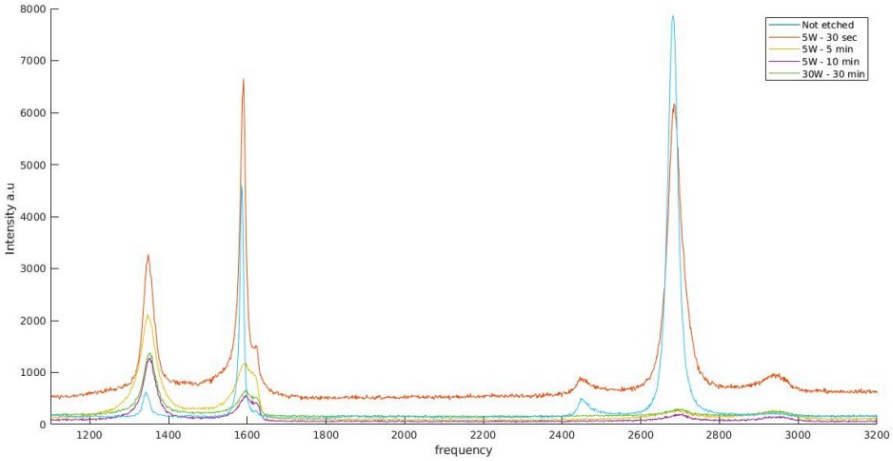


Figure 9: Raman measurement after remote hydrogen etching for different times

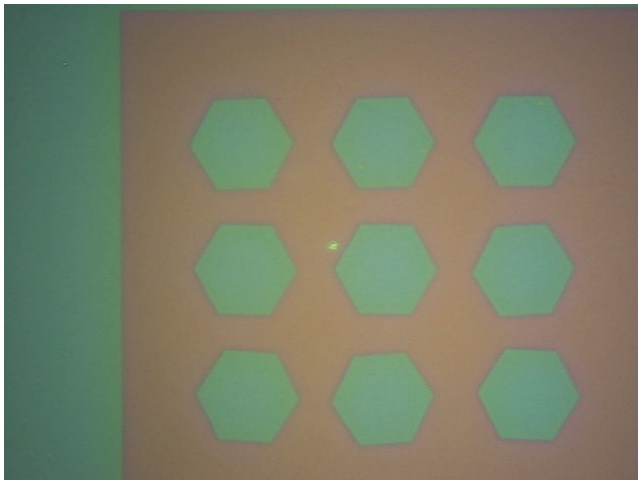

(a) Resist thickness after 5W for 30 seconds hydrogen plasma etching

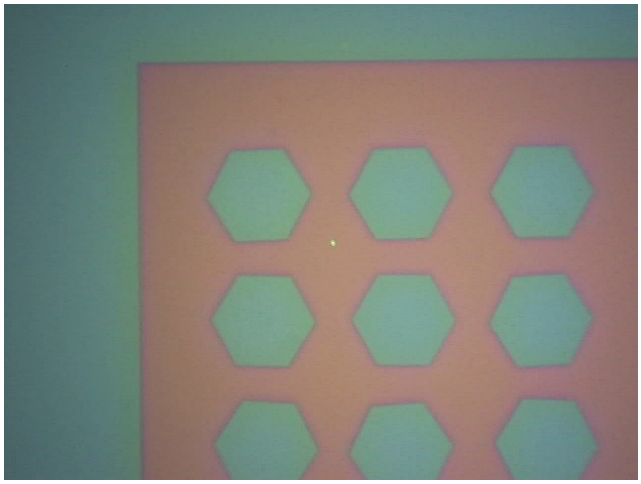

(b) Resist thickness after 5W for 5 minutes hydrogen plasma etching

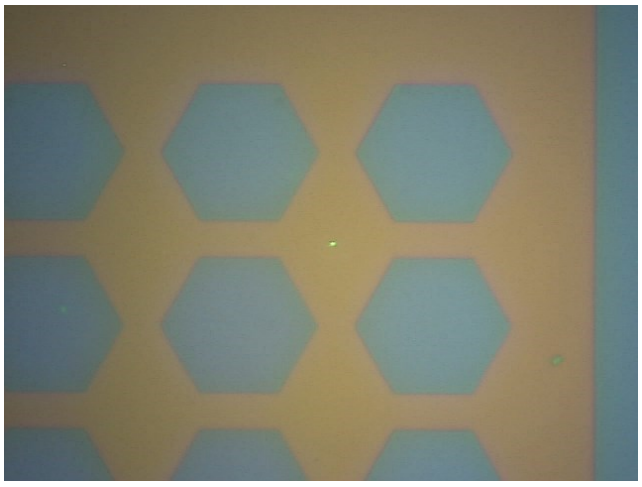

(c) Resist thickness after 5W for 10 minutes hydrogen plasma etching

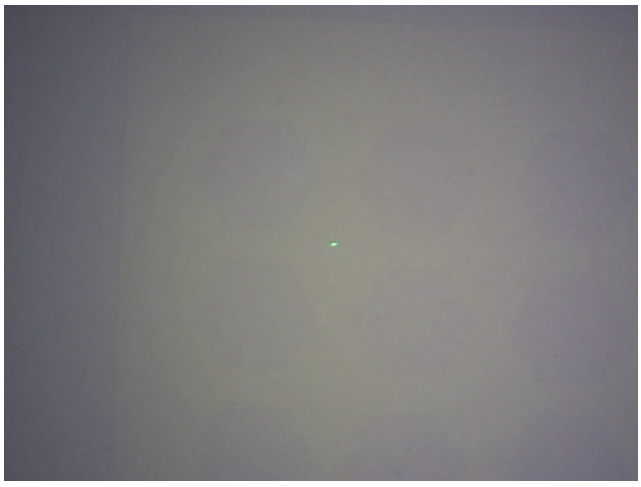

(d) Resist thickness after 30W for 30 minutes hydrogen plasma etching

Figure 10: Changes of the PMMA thickness after each etching step.